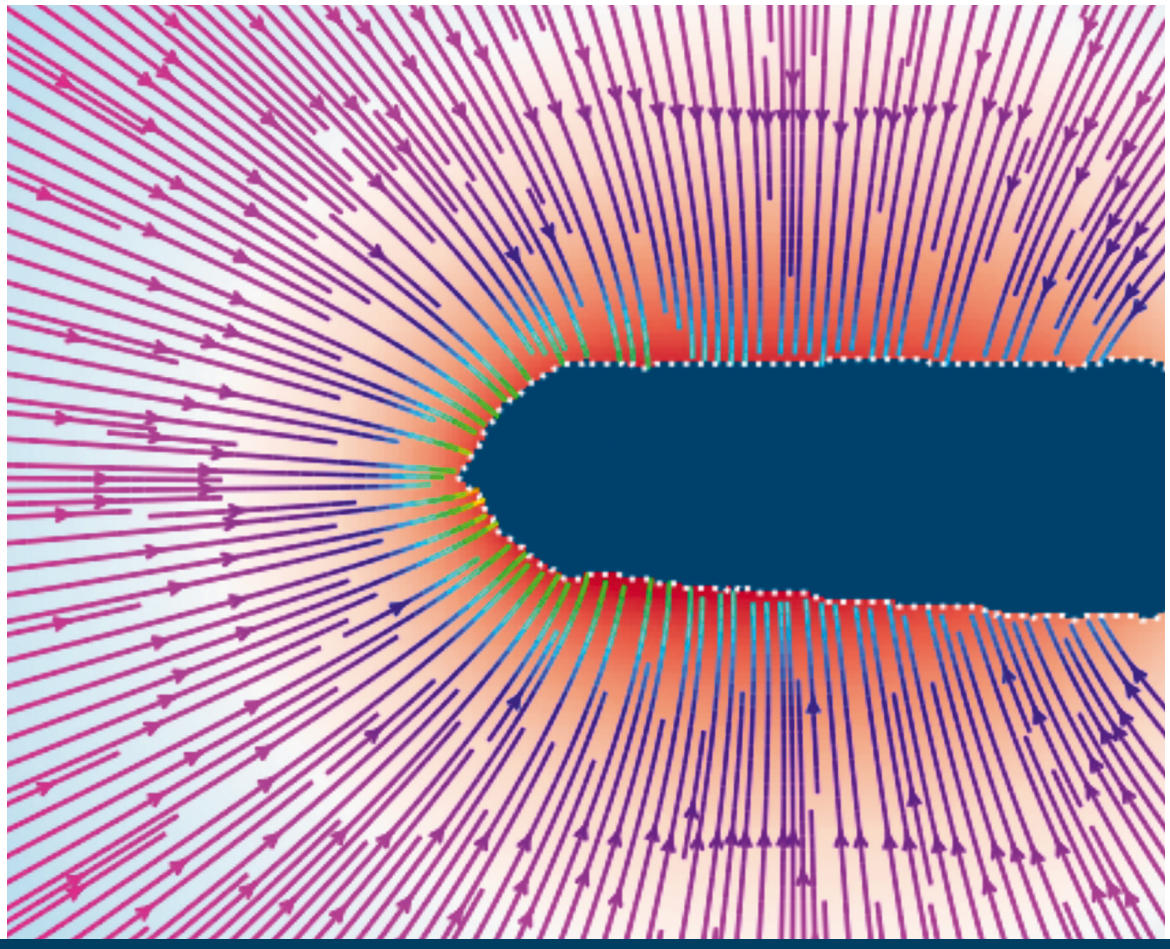

High spatial resolution and three-dimensional measurement of charge density and electric field in nanoscale materials using off-axis electron holography

Fengshan Zheng

Schlüsseltechnologien / Key Technologies
Band / Volume 221
ISBN 978-3-95806-476-8

Mitglied der Helmholtz-Gemeinschaft

JÜLICH
Forschungszentrum

Schriften des Forschungszentrums Jülich
Reihe Schlüsseltechnologien / Key Technologies Band / Volume 221

Forschungszentrum Jülich GmbH
Ernst Ruska-Centre for Microscopy and Spectroscopy with Electrons (ER-C)
Physics of Nanoscale Systems (ER-C-1) / Microstructure Research (PGI-5)

High spatial resolution and three-dimensional measurement of charge density and electric field in nanoscale materials using off-axis electron holography

Fengshan Zheng

Schriften des Forschungszentrums Jülich
Reihe Schlüsseltechnologien / Key Technologies Band / Volume 221

ISSN 1866-1807 ISBN 978-3-95806-476-8

Bibliografische Information der Deutschen Nationalbibliothek.
Die Deutsche Nationalbibliothek verzeichnet diese Publikation in der
Deutschen Nationalbibliografie; detaillierte Bibliografische Daten
sind im Internet über http://dnb.d-nb.de abrufbar.

Herausgeber und Vertrieb:	Forschungszentrum Jülich GmbH Zentralbibliothek, Verlag 52425 Jülich Tel.: +49 2461 61-5368 Fax: +49 2461 61-6103 zb-publikation@fz-juelich.de www.fz-juelich.de/zb
Umschlaggestaltung:	Grafische Medien, Forschungszentrum Jülich GmbH
Druck:	Grafische Medien, Forschungszentrum Jülich GmbH
Copyright:	Forschungszentrum Jülich 2020

Schriften des Forschungszentrums Jülich
Reihe Schlüsseltechnologien / Key Technologies, Band / Volume 221

D 82 (Diss. RWTH Aachen University, 2020)

ISSN 1866-1807
ISBN 978-3-95806-476-8

Vollständig frei verfügbar über das Publikationsportal des Forschungszentrums Jülich (JuSER)
unter www.fz-juelich.de/zb/openaccess.

Abstract

The ability to make local measurements of charge density in nanoscale materials and devices is essential for understanding many material properties. The charge density can then be used to infer the electric field or electrostatic potential within and around the specimen. This information is important for scientists working on subjects such as field electron emission and atom probe tomography.

Off-axis electron holography is a powerful technique that can be used to record the phase shift of a high-energy electron wave travelling through an electron-transparent specimen in a transmission electron microscope. Information about the charge density within the specimen can be retrieved from the measured phase with high spatial resolution. In this thesis, charge density and electric field measurements are performed, both in projection and in three dimensions, with a primary focus on samples that have a needle-shaped geometry. Three approaches are used: an analytical model-dependent approach, a model-independent approach and an approach based on numerical model-based iterative reconstruction. The model-based iterative approach allows *a priori* information, such as the shape of the object and the influence of charges that are located outside the field of view, to be taken into account. More importantly, it also allows for the reconstruction of three-dimensional charge density distributions from incomplete tomographic tilt of phase images without the artefacts that would be present if conventional tomographic reconstruction algorithms were used.

In this thesis, a W_5O_{14} nanowire is investigated experimentally in the presence of an applied electrical bias and the charge distribution along it is evaluated. A carbon fibre needle-shaped specimen is then studied, in order to demonstrate the capability of the model-based iterative approach to measure the three-dimensional charge density, electric field and electrostatic potential both inside and around it. Finally, a systematic investigation of electron-beam-induced charging in a needle-shaped specimen with an insulating Al_2O_3 apex is presented, including the dependence of the results on electron dose rate, total dose, temperature, primary electron energy and the surface state of the sample. Great care is required with the acquisition and interpretation of the results, in particular because charging phenomena are sensitive to the electrical conductivity of the sample, the presence of contact potentials and the presence of (unknown) surface states.

Kurzfassung

Die Fähigkeit, lokale Messungen der Ladungsdichte in nanoskaligen Materialien und Geräten durchzuführen, ist für das Verständnis vieler Materialeigenschaften unerlässlich. Aus der Ladungsdichte kann dann auf das elektrische Feld oder das elektrostatische Potential innerhalb und um die Probe herum geschlossen werden. Diese Informationen sind wichtig für Wissenschaftler, die an Themen wie Feldelektronenemission und Atomsonden-Tomographie arbeiten.

Die Off-Axis-Elektronenholographie ist eine leistungsstarke Technik, mit der die Phasenverschiebung einer hochenergetischen Elektronenwelle, die durch eine elektronenstrahlendurchlässige Probe läuft, in einem Transmissionselektronenmikroskop aufgezeichnet werden kann. Aus der gemessenen Phase können mit hoher Ortsauflösung Informationen über die Ladungsdichte in der Probe gewonnen werden.

In dieser Arbeit werden Ladungsdichte- und elektrische Feldmessungen sowohl in Projektion als auch in drei Dimensionen durchgeführt, wobei der Schwerpunkt auf Proben mit nadelförmiger Geometrie liegt. Es werden drei Ansätze verwendet: ein analytischer modellabhängiger Ansatz, ein modellunabhängiger Ansatz und ein Ansatz, der auf numerischer modellbasierter iterativer Rekonstruktion basiert.
Der modellbasierte iterative Ansatz erlaubt es, *a priori* Informationen, wie z.B. die Form des Objekts und den Einfluss von Ladungen, die sich außerhalb des Sichtfeldes befinden, zu berücksichtigen. Noch wichtiger ist, dass er auch die Rekonstruktion dreidimensionaler Ladungsdichteverteilungen aus unvollständigen tomographischen Verkippungen von Phasenbildern ohne die Artefakte ermöglicht, die bei Verwendung herkömmlicher tomographischer Rekonstruktionsalgorithmen vorhanden wären.

In dieser Arbeit wird ein W_5O_{14} Nanodraht experimentell in Gegenwart einer angelegten elektrischen Vorspannung untersucht und die Ladungsverteilung entlang dieses Nanodrahtes ausgewertet. Anschließend wird eine Kohlenstofffaser untersucht, um die Fähigkeit des modellbasierten iterativen Ansatzes zur Messung der dreidimensionalen Ladungsdichte, des elektrischen Feldes und des elektrostatischen Potentials in und um den Draht herum zu demonstrieren.
Schließlich wird eine systematische Untersuchung der elektronenstrahlinduzierten Aufladung in einer Atomsondennadel mit einer isolierenden Al_2O_3 Spitze vorgestellt, einschließlich der Abhängigkeit der Ergebnisse von Elektronendosisleistung, Gesamtdosis, Temperatur, der Energie des einfallenden Elektronenstrahls und dem Oberflächenzustand der Proben. Große Sorgfalt ist bei der Erfassung und Interpretation der Ergebnisse erforderlich, insbesondere weil Aufladungsphänomene empfindlich auf die elektrische Leitfähigkeit der Probe, das Vorhandensein von Kontaktpotentialen und das Vorhandensein von (unbekannten) Oberflächenzuständen reagieren.

Table of contents

List of figures

List of tables

Nomenclature

Roman Symbols

a	Amplitude of complex-valued wavefunction
$\mathbf{C}$	Cost function
C_E	Interaction constant
$\mathbf{E}$	Electric field vector
$\mathbf{F}$	Forward model
$\mathbf{M}$	Phase mapping matrix
$\mathbf{P}$	Projection matrix
$\mathbf{R}$	Regularisation term
$\mathbf{r}$	Three-dimensional position (x, y, z)
V	Electrostatic potential
$\mathbf{x}$	Vectorised charge density
x, y, z	Cartesian coordinates
$\mathbf{y}$	Concatenation of pixels in phase image(s)

Greek Symbols

ε_0	Vacuum dielectric constant or permittivity
λ	Regularisation parameter
∇	Two-dimensional gradient operator

∇^2	Two-dimensional Laplacian operator
ψ	Wavefunction
ρ	Charge density
φ	Phase of complex-valued wavefunction

Acronyms / Abbreviations

2*D*	Two-dimensional, two dimensions
3*D*	Three-dimensional, three dimensions
APT	Atom probe tomography
CCD	Charge-coupled device
CVD	Chemical vapour deposition
DPC	Differential phase contrast
EDS	Energy-dispersive spectroscopy
FFT	Fast Fourier transform
FIB	Focused ion beam
FOV	Field of view
HAADF	High-angle annular dark-field
MBIR	Model-based iterative reconstruction
MIP	Mean inner potential
NFESEM	Near field emission scanning electron microscopy
PRW	Perturbed reference wave
SD	Standard deviation
SEM	Scanning electron microscopy
SIMDALEE	Sources, Interaction with Matter, Detection and Analysis with Low Energy Electrons

SNR	Signal-to-noise ratio
STEM	Scanning transmission electron microscopy
STM	Scanning tunnelling microscopy
TEM	Transmission electron microscopy
UHV	Ultra-high vacuum

Chapter 1

Introduction

1.1 Importance of local charge density and electric field measurement in materials science

Information about charge density in nanoscale materials and devices is important for understanding properties such as conductivity, permittivity, ferroelectricity, piezoelectricity and spontaneous polarisation [1], as well as charge accumulation at interfaces and surfaces [2, 3] and charging and discharging processes, for example in solid state batteries [4, 5]. It is also beneficial to understand the phenomenon of electron-beam-induced charging in combinations of insulating, semiconducting and conducting materials in the electron microscope. Furthermore, it is of both fundamental and practical interest to be able to detect elementary charges experimentally with high spatial resolution.

In this thesis, the research fields that are of particular interest are charge accumulation at interfaces and surfaces in materials, electron-beam-induced charging of specimens in the electron microscope and the measurement of electric fields outside electrically-biased needle-shaped specimens, such as field emitters and atom probe needles.

1.1.1 Charge accumulation at interfaces and surfaces of materials

Charge accumulation at interfaces and surfaces plays a critical role in the performance of materials and nanoscale devices, *e.g.*, *p-n* junctions [6], metal-semiconductor junctions, ferroelectric tunnel junctions [3], two-dimensional (2D) electron gases [7] and grain boundaries in electroceramics [2]. The accumulation of charges at interfaces plays an important role in the electrical conductivity of such systems. For instance, space charge layers at grain boundaries in doped ceria (CeO_2), which is regarded as a possible electrolyte for use in

intermediate temperature solid oxide fuel cells [8], are generally believed to be responsible for the deterioration of its ionic conductivity [9, 10].

Attempts have been made to measure either the charge density or the electrostatic potential in such systems using phase contrast techniques in the transmission electron microscope (TEM). Examples include studies of *p-n* junctions [11, 12, 6, 13], 2D electron gases in $LaAlO_3/SrTiO_3$ [14, 7], $SrTiO_3$ bicrystals [2, 15–17], grain boundaries in Sm-containing doped ceria [18] and grain boundaries between Ca-doped and undoped $YBa_2Cu_3O_{7-x}$ [19]. Theoretical models have been set up to interpret experimental measurements of space charge layers at grain boundaries [20, 21]. Available phase contrast TEM techniques include Fresnel contrast analysis [17], off-axis electron holography [2, 15, 16, 19, 11, 12, 6, 18], in-line electron holography [14, 7] and differential phase contrast (DPC) imaging in the scanning TEM (STEM) [13].

When applying phase contrast techniques, one has to be careful about dynamical diffraction effects, the electrostatic mean inner potential (MIP) of the specimen, surface damage introduced by the preparation of electron-transparent specimens and electron-beam-induced charging, as well as microscope parameters such as aberrations. For these reasons, most previous reports of space charge measurements in the TEM are inconclusive or affected by artefacts. The trustworthy, quantitative measurement of charge density with high spatial resolution requires consideration of all of these effects on experimental measurements.

1.1.2 Electron-beam-induced charging

The phenomenon of electron-beam-induced specimen charging has been discussed in the literature since the early 1960s (*e.g.*, [22, 23]). Specimen charging occurs when poorly-conducting or poorly-electrically-contacted specimens are observed in the electron microscope, as the inelastic scattering of electrons leads to the emission of secondary electrons. This process has been investigated intensively mainly in the scanning electron microscope (SEM) (*e.g.*, [24]), but rarely in the TEM for specimens that are thinner for higher energies of the primary electrons.

In recent years, specimen charging in biological specimens has attracted increasing attention in cryomicroscopy (*e.g.*, [25, 26]), as it causes a strong degradation in image quality and therefore a loss of spatial resolution. Some work has been carried out to investigate the charging of carbon films, either for application as a support for biological specimens (*e.g.*, [25, 26]) or for application as electrostatic phase plates (*e.g.*, [27]). Charging effects in carbon films are sometimes referred to as the "bee-swarm" effect [22], which is also known as the "Berriman effect" in biological electron microscopy [28–30].

Specimen charging can result in image distortion, image astigmatism that may vary with sample position, electron-beam-induced movement of irradiated areas of the specimen and strong contrast at sharp or broken edges of the sample. Theoretical explanations of the microscopic mechanisms of charging, in particular by Jacques Cazaux [31–35], do not yet provide a satisfactory description of the phenomenon. A phase contrast transfer function method has been used to measure the phase shift induced by the electric potential due to charging [36, 37]. There are also several off-axis electron holography studies of charging in the TEM [38–41], but the interpretation of such results is still simplistic and inconclusive.

The real-time quantitative measurement of electron-beam-induced charging is essential to understand the mechanisms of charging in thin specimens that have different electrical properties and geometries, as well as to understand how to reduce charging effects when imaging using both low and high energy electrons.

In addition to the above considerations, the charge density in a specimen can be regarded as a fundamental quantity that can in turn be used to infer the spatial distribution of the electric field, which can itself be difficult to measure directly, in part because of its slow decay, strong dependence on boundary conditions and the positions of image charges. Such measurements of electric field are particularly important for studies of needle-shaped specimens, such as field emitters and atom probe needles, in order to calculate the trajectories of electrons or ions that are emitted or extracted from them during field emission or field evaporation. In this way, information about the electric field measured in the TEM can provide a type of aberration correction for the reconstruction of three-dimensional (3D) atom positions in atom probe tomography (APT). It can also assist with the evaluation of the material's field emission performance.

1.1.3 Cold field emission

Cold field emission has been used widely in a variety of applications, especially for electron sources in electron microscopy (*e.g.*, [42]). It is based on the emission of electrons as a result of the presence of a strong electrostatic field. Field emission occurs only when the electric field strength at the surface of the specimen, which is usually needle-shaped or tip-like, is on the order of GV/m. It also strongly depends on the work function of the surface of the material. A theoretical explanation for field emission by quantum tunnelling was proposed in 1928 [43]. The so-called "Fowler-Nordheim" (*F-N*) equation is used to describe the local current density emitted from internal electron states in the conduction band of a bulk metal. It states that the current density emitted from a small uniform area of a surface is

determined by the local work function and the local electric field. However, the *F-N* equation is no longer valid if the electric field is very strong [44, 45], in particular for nanostructures such as nanowires and nanotubes. The details of the electric field around a field emitter play a vitally important role in determining its field emission properties, including the current density, emission area and temporal coherence.

Therefore, *in situ* observations of the charge density, electric field or electrostatic potential of a field emitter before and during field emission are paramount for understanding the field emission process and the underlying mechanisms. Several attempts have been made to measure the electric fields of field emitters fabricated from different materials, including carbon nanotubes [46], carbon cone nano-tips [47–49], $TaSi_2$ nanowires [50], as well as used and unused Schottky field emission gun emitters [51].

However, in most previous experiments performed using off-axis electron holography, the slow decay of the electric field prevented the use of conventional tomographic approaches to retrieve 3D information about the electric field, which extended outside the field of view (FOV). In addition, the presence of a fringing field in vacuum added technical difficulties to the interpretation of the off-axis electron holograms.

1.1.4 Atom probe tomography

The technique of atom probe tomography, which aims at obtaining the atom-by-atom internal structure of a material, usually involves two processes: field evaporation by an electric field at the surface of a needle-shaped specimen and projection of the ions determined by the electric field around the apex [52, 53]. A knowledge of the electric field is therefore essential to understand both the field evaporation process and the projection of the ions. The latter process, in particular, is significant for establishing the fidelity of the reconstruction of 3D atomic positions.

A standard APT reconstruction algorithm assumes a homogeneous evaporation field from an approximately hemi-spherical surface that has a certain radius and is positioned on a truncated cone with a certain shank angle [54]. This assumption is expected to hold most closely when the specimen is homogeneous and the analysis is performed for a small FOV. However, in the majority of cases, the specimen will contain different materials and phases, which have different evaporation fields. The assumption of a homogeneous evaporation field is then no longer valid. Even if a specimen has only a single phase, the surface of the tip cannot be assumed to be perfectly smooth for a wide FOV, especially if there is any anisotropy of the evaporation fields, as well as in the presence of surface atom diffusion or motion. The difference between the electric field modelled on the above assumptions and the true electric field will induce so-called "trajectory aberrations" [55]. For instance,

in multiphase specimens, which may contain precipitates in a matrix, the so-called local magnification effect [56, 57], or chromatic aberration [55], can result in spatial distortions of the reconstruction due to the different evaporation fields of the individual phases. During "dynamic reconstruction" [58], reconstruction parameters such as the radius of the tip, the field factor and the image compression factor are allowed to change dynamically during evaporation. However, a standard reconstruction algorithm is still typically used.

Although numerical simulations have been implemented to calculate the exact trajectory of each ion, the computational cost and assumptions required to set up such simulations still preclude their routine use [59].

Correlative TEM and APT experiments have been utilised to provide combined information for the reconstruction of atomic positions, in particular by providing measurements of the morphology and radius of the specimen [60, 61]. However, direct measurements of electric field are still lacking. Currently, real-time measurements of electric field during APT using TEM are not possible, as there is no instrument that combines TEM and APT simultaneously. Until such an instrument becomes available, sequential snapshots of the electric field would already be of great value to assess and improve the fidelity of APT reconstructions.

1.2 Charge density and electric field measurement in the transmission electron microscope

Off-axis electron holography is sensitive to the electrostatic potential within and around a specimen projected along the incident electron beam direction and has been widely used to study long-range electrostatic fields [62–65], such as those originating from triboelectric charges [66], trapped charges in specimens [67], charges at dislocations [68], electron-beam-induced charges in TEM specimens [38, 40, 30, 69], *p*-*n* junctions [6, 70], dynamic charging in Li-ion battery materials [4], electrically biased tips [71–73], nanotips [74] and field emitters [46, 50, 51, 48, 49].

Other related phase contrast techniques in the TEM that are also sensitive to electrostatic potentials include in-line electron holography, DPC imaging, as well as ptychography applied to pixelated STEM data. Iterative reconstruction algorithms have been developed for in-line electron holography [75] and comparisons between in-line and off-axis electron holography have been carried out [76, 77]. DPC imaging is sensitive to the phase gradient rather than to the phase itself, *i.e.*, to the projected in-plane electric field, rather than to the projected electrostatic potential [78]. DPC imaging has been used to measure polarisation fields [79, 80], piezoelectric fields [81], built-in electric fields at *p*-*n* junctions [13] and atomic-

resolution signals [78, 82, 83]. The accuracy and precision of the technique are determined by the detector geometry and performance, experimental stability during scanning, calibration of the instrument and careful interpretation [84].

This thesis is dedicated to fundamental and practical aspects of quantitative charge density measurement at the nanoscale using off-axis electron holography and its application to needle-shaped specimens. However, most of the approaches and conclusions are also relevant to the interpretation of experimental results obtained using other phase contrast techniques, including in-line electron holography, DPC imaging and ptychography in the STEM.

1.3 Relationship to research on low energy electrons in the SIMDALEE2 Marie Curie Initial Training Network

The SIMDALEE2 (Sources, Interaction with Matter, Detection and Analysis with Low Energy Electrons) project [1] is a research and training network that is dedicated to the investigation of low energy electrons near solid surfaces. It aims to establish a comprehensive and effective research platform for the study of low energy electrons. Within this framework, information about the charge density distributions and electric fields of needle-shaped specimens is crucial to understand how electrons behave during and after field emission and how they subsequently interact with the surfaces and internal structures of materials. In particular, the project is strongly related to near field emission scanning electron microscopy and specimen charging.

The near field emission scanning electron microscopy (NFESEM) technique [85], in which electrons are extracted by field emission from a sharp tip that is positioned a few tens of nm from a surface, involves the collection and analysis of secondary electrons generated at the surface. The electric field around the tip is crucial because field emission at such a close tip-electrode (specimen surface) distance results in the self-focusing of electrons that are emitted from a nm-sized tip [86]. It therefore determines the lateral resolution of such an instrument and influences the mechanism of image contrast formation.

In an SEM that typically operates at electron energies of between from several Volts and several thousand Volts for the study of both biological and inorganic specimens, information about the electric field that is present within and around the sample would help to understand the mechanism of image contrast formation [87]. Quantitative charge density measurements

[1] Marie Curie Initial Training Network (ITN) financed by the European Commission (grant number 606988 under the FP7-PEOPLE-2013-ITN action of the European Commission).

resulting from electron-beam-induced specimen charging would also be beneficial for understanding charging in both SEM [24] and TEM, as well as providing pathways for the mitigation and control of charging during experimental image acquisition.

Chapter 2

Fundamentals of off-axis electron holography and strategy for charge density measurement

2.1 Off-axis electron holography

The concept of holography was first proposed by Denis Gabor in 1948 [88]. When it is applied in the TEM, the technique is capable of retrieving both phase and amplitude information about the electron wave. It therefore allows for the correction of coherent aberrations and the improved interpretation of recorded images. In particular, the TEM mode of off-axis electron holography, which is illustrated schematically in Fig. 2.1a, allows both the phase φ and the amplitude a of the wavefunction $\psi = a\exp(i\varphi)$ that is transmitted through an electron-transparent specimen to be retrieved directly [89]. When applying the technique, the specimen is illuminated by either a spherical wave or a plane wave (*I*). The object wave that has travelled through the specimen is overlapped with a reference wave that has travelled through vacuum with the aid of an electrostatic biprism (*EB*), which is normally a thin wire that has a positive voltage applied to it and is positioned in a conventional selected area aperture plane, resulting in the formation of an interference pattern or hologram (*Hol*). The hologram is magnified by the projection lenses of the microscope (not shown) and recorded on a digital detector. It can then be processed to retrieve real-space phase and amplitude information about the object. The experimental setup for the examination of an electrically-biased needle-shaped specimen (*Sp*, red) is shown in Fig. 2.1b. A photograph of the microscope that is used for off-axis electron holography experiments in Forschungszentrum Jülich is shown in Fig. 2.1c.

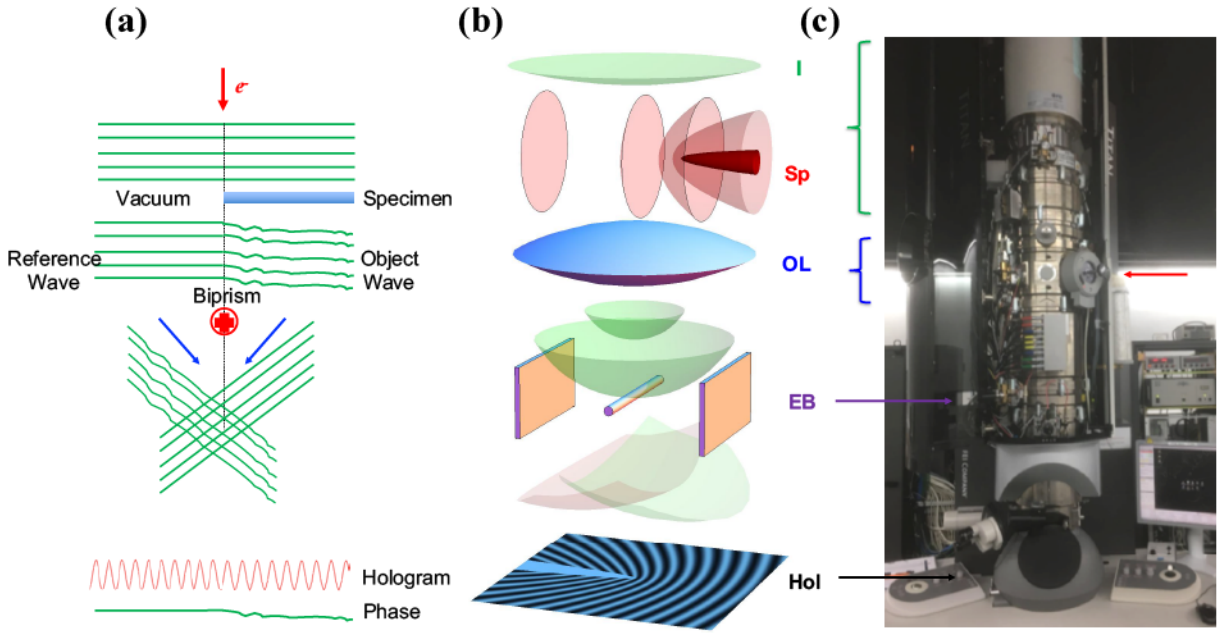

Fig. 2.1 (a) Schematic diagram illustrating the principle of off-axis electron holography. (b) Experimental setup for off-axis electron holography. (c) Photograph of an FEI Titan transmission electron microscope in Forschungszentrum Jülich. Corresponding components are labelled using the same colours. From top to bottom in (b) are: an illuminating spherical or plane electron wave *I*, an electrically-biased needle-shaped specimen *Sp*, the electron microscope objective lens *OL*, an electron biprism *EB* and a recorded off-axis electron hologram *Hol*. Semi-transparent red surfaces in (b) show equipotential surfaces around the electrically-biased needle. For clarity, the counter-electrode is not shown here, but its location could be inferred by the flatness of the left equipotential surface.

In the absence of dynamical scattering and magnetic fields, the electron optical phase shift φ can be written as follows [90]:

$$\varphi(x,y) = C_E \int_{-\infty}^{+\infty} V_t(x,y,z)\, dz, \tag{2.1}$$

where z is the incident electron beam direction, (x, y) are 2D Cartesian coordinates in the specimen plane, C_E is a constant that depends on the microscope accelerating voltage ($C_E = 6.53 \times 10^6$ rad/(V m) at 300 kV) and V_t is the total electrostatic potential, which includes contributions from the mean inner potential (MIP), fixed charges (*e.g.*, ions), mobile charges and polarisation-induced charges.

If the electrostatic biprism is oriented along the y axis, then the intensity in the hologram in an ideal imaging system can be expressed in the form [62, 63, 91]

$$I(x,y) = \left| \psi\left(x - \frac{d}{2}, y\right) \exp\left(\frac{i\pi x}{s}\right) + \psi\left(x + \frac{d}{2}, y\right) \exp\left(-\frac{i\pi x}{s}\right) \right|^2, \tag{2.2}$$

where d is the interference distance [1](depending on the potential and the width of the biprism), and s is the spacing of the interference fringes. Eq. 2.2 describes the intensity distribution in the hologram.

If the object is located at $x + d/2$, then the corresponding object wave $\psi\left(x + \frac{d}{2}, y\right)$ is overlapped with the reference wave $\psi\left(x - \frac{d}{2}, y\right)$. In order to retrieve the amplitude and the phase of the object wave, the reference wave should ideally be equal to unity, *i.e.*, a plane wave, or it should be known.

When a long-range electric field originates from the specimen, as shown in Fig. 2.1b, the reference wave may be perturbed, such that its phase is not flat and it already contains information about the specimen. Analysis of the hologram then results in the reconstruction of a fictitious specimen that can be described by the wavefunction [62, 63]

$$\psi(x,y) = a(x,y)\, \exp\left[i\varphi\left(x + \frac{d}{2}, y\right) - i\varphi\left(x - \frac{d}{2}, y\right)\right], \tag{2.3}$$

where $a(x,y)$ is the amplitude of the object wave and $\varphi(x + \frac{d}{2}, y)$ and $\varphi(x - \frac{d}{2}, y)$ are the phases of the object and reference waves, respectively. The difference between these two phases, rather than the true object phase, is then reconstructed. The influence of such a perturbed reference wave (PRW) on measurements of charge density and electric field is discussed below.

[1]The interference distance is, in fact, a vector, which depends on the rotation angle of the biprism. Here, for simplicity, it is assumed that the biprism is oriented parallel to the y axis.

Once the object phase, which is proportional to the projected potential, has been reconstructed (see Chapter 4 for reconstruction details), it can be analysed further to obtain the charge density across the FOV.

2.2 Charge density measurement using off-axis electron holography

2.2.1 Model-independent approach

In classical electrodynamics, the potential V_Q (where the subscript Q is used to indicate that the potential is entirely due to physical charges and does not include the contribution from the MIP of the specimen) is generated by the source charge density, $\rho(x, y, z)$, according to Poisson's equation

$$\nabla^2 V_Q = -\frac{\rho(x,y,z)}{\varepsilon_0}, \tag{2.4}$$

where ε_0 is the vacuum permittivity. According to Gauss' law, the flux of the electric field through a closed surface is proportional to the charge inside the volume of space bounded by that surface:

$$\oiint_{\partial\Omega} \mathbf{E} \cdot d\mathbf{S} = \frac{1}{\varepsilon_0} \iiint_{\Omega} \rho(x,y,z)\, dV, \tag{2.5}$$

where $\mathbf{E}$ is the electric field and $\partial\Omega$ is a surface that encloses the volume Ω.

In off-axis electron holography, in the presence of a PRW and in the absence of the MIP (*i.e.*, when $V_t = V_Q$), the substitution of $\varphi(x,y)$ in Eq. 2.3 by Eq. 2.1 results in an expression for the reconstructed phase $\varphi_{rec}(x,y)$ (*i.e.*, the phase term of ψ in Eq. 2.3) that has the form [71]

$$\varphi_{rec}(x,y) = C_E \int_{-\infty}^{+\infty} \left[V_Q\left(x+\frac{d}{2},y,z\right) - V_Q\left(x-\frac{d}{2},y,z\right)\right] dz. \tag{2.6}$$

By combining Eqs. 2.4, 2.5 and 2.6, the relationship between the measured phase and the charge density in the specimen can be written [74, 40]

$$\iint_C \nabla^2 \varphi(x,y)_{rec}\, dxdy = -\frac{C_E}{\varepsilon_0} \iint_C \rho_{proj}(x,y)\, dxdy = -\frac{C_E}{\varepsilon_0} Q_C, \tag{2.7}$$

where C is the region of integration (Fig. 2.2), ∇^2 is a two-dimensional Laplacian operator, $\rho_{proj}(x,y) = \int \rho(x+\frac{d}{2},y,z)dz$ is the projected charge density and Q_C is the total charge in

region C. The volume over which Gauss' law is evaluated is an infinite cylinder (along the z axis), of which C is a cross-section.

Evaluation of the Laplacian of the phase is facilitated by the fact that it can be calculated directly from the reconstructed complex wavefunction using the expression [74]

$$\nabla^2\varphi = \mathrm{Im}\left[\frac{\nabla^2\psi}{\psi} - \left(\frac{\nabla\psi}{\psi}\right)^2\right]. \tag{2.8}$$

By making use of the divergence theorem, Eq. 2.7 can equivalently be written in the form [40]

$$Q_C = -\frac{\varepsilon_0}{C_E}\oint_{\partial C} \nabla\varphi_{rec}(x(l),y(l))\cdot\mathbf{n}(x(l),y(l))\,dl, \tag{2.9}$$

where ∇ is a two-dimensional gradient operator, ∂C denotes an integration loop (coinciding with the boundary of the integration region C in Eq. 2.7), l is a curvilinear coordinate along the loop and $\mathbf{n}$ is the outward normal to the loop, as shown schematically in Fig. 2.2.

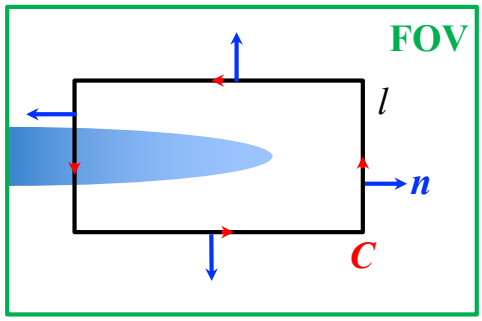

Fig. 2.2 Schematic diagram illustrating the application of the model-independent approach to the analysis of a phase image of a needle-shaped specimen. The green rectangle indicates the FOV. The black rectangle is a chosen integration loop C, with curvilinear coordinate l and corresponding outward normal vector $\mathbf{n}$.

2.2.2 Analytical model-dependent approach

Model-dependent approaches that are helpful for the determination of charge density distributions from phase images can be based on the use of finite-element simulations (*e.g.*, [49, 66]) or on analytical solutions for simple sample geometries, such as nanoparticles [92] and needle-shaped specimens [71, 72, 93].

The development of an analytical model-dependent approach depends on the availability of a model that can be used to solve the Laplacian equation to calculate the charge density from a holographic phase image. *Prior* knowledge of the shape and morphology of the specimen and a counter-electrode, if one is present, as well as of the boundary conditions, is required. Moreover, the model should ideally be as simple as possible.

Needle-shaped specimens have previously been modelled using a line charge distributions in front of grounded conducting planes [71, 93]. The justification for the utilisation of such a model is that equipotential surfaces around a line of constant charge density take the form of ellipsoids, which are in turn similar to the outer boundary of a needle-shaped specimen, which is often conducting and itself expected to be an equipotential surface. The line charge density can then be adjusted until a best match is obtained between experimental and simulated images of the phase outside the specimen. The influence of the presence of a grounded conducting plane on the electrostatic potential distribution and electron optical phase can be included by using image charge methods [71] (*cf.* Appendix 2). In the presence of an external field, a linear line charge model, in which the charge density increases along the length of the needle, can be used [72, 93] (*cf.* Appendix 2).

The above two approaches are routinely used in the literature (*e.g.*, [71, 74, 40, 72]). Their corresponding advantages and disadvantages for the evaluation of charge density using off-axis electron holography are compared and discussed in detail for a needle-shaped specimen in Chapter 4.

Chapter 3

Experimental setup and choice of specimens

3.1 Off-axis electron holography in the TEM

An FEI Titan G^2 60−300 TEM equipped with an ultra-bright field emission electron gun (X-FEG) and two electrostatic biprisms was used for off-axis electron holography experiments in this thesis. A photograph of this microscope is shown in Fig. 2.1c. The operating voltage was set to 300 kV, unless stated otherwise. In order to obtain a large FOV, experiments were usually performed in Lorentz mode, with the conventional microscope objective lens switched off. Off-axis electron holograms were recorded either using a $\sim 2k \times 2k$ charge-coupled device (CCD) Ultrascan camera (Gatan Inc.) or a $\sim 4k \times 4k$ direct electron counting K2-IS camera (Gatan Inc.). Reference holograms were acquired from vacuum with the specimen removed from the FOV. Real-space phase and amplitude images were reconstructed from recorded electron holograms using a standard fast Fourier transform (FFT) algorithm in Holoworks software (Holowerk LLC.).

High-angle annular dark-field (HAADF) imaging and chemical mapping in STEM mode were performed on an FEI Titan 80−200 ChemiSTEM microscope equipped with a Super-X energy-dispersive spectrometer (EDS) and operated at 200 kV.

For cooling experiments, the specimen temperature was controlled using a Gatan liquid N_2 model 636 cooling holder (Gatan Inc.).

3.2 Electrical biasing setup

A scanning tunnelling microscopy (STM)-TEM holder [94] (Nanofactory Instruments) was used for electrical biasing experiments on needle-shaped specimens, as shown in Fig. 3.1. The needle-shaped specimen was usually glued to the top of a W wire of diameter 0.25 mm and then inserted into the housing of the holder. The STM tip, which was used as a counter-electrode, was usually made from Au or W. The typical size of the tip of the counter-electrode was several μm or hundreds of nm. The STM tip was fixed to the movable hat, which was controlled by a piezo tube. In this way, the distance between the STM tip and the specimen could be adjusted. An electrical voltage of between -200 and +200 V could then be applied between the needle-shaped specimen and the counter-electrode. This setup allows spatially-resolved measurements of electric fields around atom probe specimens or field emitters to be obtained. These results are presented in Chapters 4 and 6-8 below.

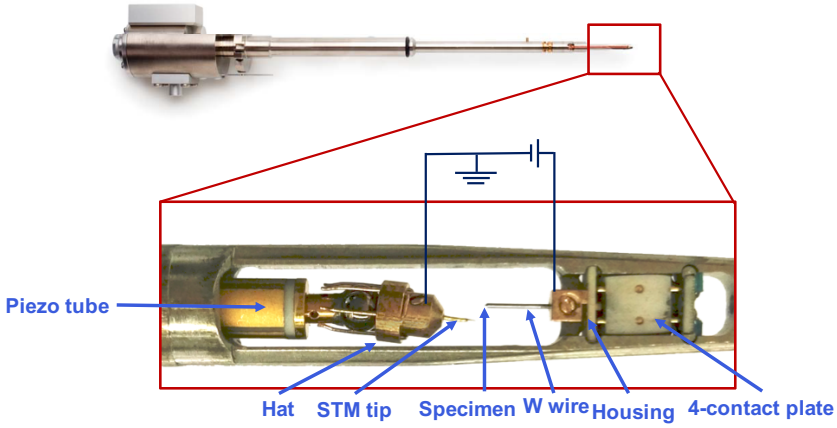

Fig. 3.1 Photographs of the Nanofactory STM-TEM specimen holder. Top: overview of the holder. Below: magnified image of the end of the holder. The specimen usually takes the form of a W wire of diameter 0.25 mm with a needle-shaped specimen mounted on top of it. The Au or W counter-electrode has a size of between several μm and several hundreds of nm and is fixed to a movable hat. In this way, the distance between the specimen and the counter-electrode can be adjusted.

3.3 Electron-beam-induced charging setup

Electron-beam-induced charging was studied systematically to evaluate its dependence on several parameters, including electron dose rate, total electron dose, temperature and applied electrical bias voltage. The electron dose rate was controlled either by the spot size while keeping the illuminated area unchanged, or by spreading the beam. Its value was read out from the K2-IS camera in units of electrons per pixel per second (*e.p.s*). The electron dose rate was typically varied between $\sim$ 40 *e.p.s* and $\sim$ 1 *e.p.s*. The total electron dose was then adjusted by varying the exposure time between 1 and 20 s. The sample temperature was controlled by using the cooling holder described above over a temperature range of between $\sim$ -180 and 80 °C. The electrical bias was controlled using the STM-TEM specimen holder described above, with a bias voltage applied to the specimen of between -200 and +200 V, while the counter-electrode was grounded.

3.4 Overview of specimens

Multiple needle-shaped specimens, including both field emitters and atom probe needles, were studied in this thesis.

3.4.1 W nanotip

A W nanotip was provided by partners from ETH Zürich. It was prepared using an electrochemical etching technique from a W wire of diameter 0.25 mm and later cleaned in an ultra-high-vacuum (UHV) chamber to remove contamination, including hydrocarbons and oxidisation. Further details can be found elsewhere [85]. Due to a lack of UHV transfer capabilities to the TEM, the W nanotip was transferred through air and was therefore covered by an oxidised layer. (See Chapter 4 for further details.)

3.4.2 LaB_6 field emitter

A LaB_6 field emitter was prepared by Maximilian Kruth from Forschungszentrum Jülich, Germany from a single crystal of LaB_6 that had a diameter of 0.6 mm using a two-step process, which involved first electrochemical etching of a tip to a diameter of several tens of μm, followed by size reduction and sharpening of the apex using focused ion beam (FIB) milling. The final diameter of the apex was approximately 30 nm. A detailed description of the preparation procedure can be found elsewhere [95].

3.4.3 W_5O_{14} nanowire

A W_5O_{14} nanowire was synthesised using an iodine transport method [96] by Saqib Muhammed from the Josef Stefan Institute, Slovenia. The starting material consisted of 352.7 mg of WO_3 powder (Sigma Aldrich, 99.99%), 37.5 mg of Ni foil and 567 mg of iodine (1-3 mm beads, Sigma Aldrich, 99.7%). WO_3 was used as the source of W and O, while Ni was added as a growth promoter. Evacuated (4×10^{-6} mbar) and sealed quartz ampoules were inserted into a two-zone furnace for 500 h. The material was transported from 860 to 736 °C. For electrical biasing experiments, the nanowire was first glued using FIB onto a sub-μm-sized W wire, which was then mounted on the fixed side of the specimen holder. (See Chapter 6 for further details.)

3.4.4 CdS nanocomb

CdS nanocombs were provided by a partner from the Beijing Institute of Technology, China. They were grown using an *in situ* seeding chemical vapour deposition (CVD) process [97]. For electrical biasing experiments, the nanocombs were first glued onto a W wire using FIB deposition, just as for the W_5O_{14} nanowire, with assistance from Maximilian Kruth from Forschungszentrum Jülich, Germany.

3.4.5 Carbon fibre needle

A high-strength carbon fibre (T1000) was obtained from Toray company [1]. The fibre comprised primarily C (>99%), with a small amount of N, in the form of a highly-textured structure along the fibre axis, with turbostratic graphene as the basic structural unit [98]. This choice of material reduces the influence of changing diffraction conditions during a tilt series of tomographic experiments. A needle-shaped specimen was prepared from the fibre using standard FIB milling by Shasha Wang, from the High Magnetic Field Laboratory, Hefei, China, similar to the application for the LaB_6 field emitter.

3.4.6 Cr_2AlC-Al_2O_3 atom probe needle

Cr_2AlC belongs to the subset of ternary metal carbides that have the general formula $M_{n+1}AX_n$ (M: early transition metal, A: A group element, X: C or N) and are referred to as MAX phases. The potential for utilising MAX phase ceramics (*e.g.*, Cr_2AlC) as self-healing materials has been investigated in recent years [99]. In these materials, the products of

[1] www.toray.jp

oxidisation, such as α-Al_2O_3 and other oxides, have been shown to fill crack sites, thereby effectively healing them. Here, this material, together with its insulating oxide, is used to investigate electron-beam-induced charging in the TEM. In this sample, α-Al_2O_3 acts as an insulator, while the MAX phase is a conductor [100]. The details of sample synthesis and atom probe needle preparation by Maximilian Kruth from Forschungszentrum Jülich, Germany and Konda Gokuldoss Pradeep from RWTH Aachen University, Germany, can be found elsewhere [101].

Chapter 4

Applications of model-independent and analytical model-dependent approaches for charge density measurement to needle-shaped specimens

This chapter is adapted from one of my own publications [102]. The model-independent and analytical model-dependent approaches for charge density measurement, which were introduced in Chapter 2, are applied to the interpretation of electron optical phase images to obtain charge density in needle-shaped specimens in this Chapter. Practical considerations associated with using the model-independent approach are discussed and illustrated through the analysis of experimental data recorded from a W nanotip. The advantages and disadvantages of the above two approaches are then compared through the study of an electrically-biased LaB_6 field emitter. The accuracy and precision of the model-independent approach are found to depend on the signal-to-noise ratio in the experimental data. For the analytical model-dependent approach, the choice of model, *i.e.*, the extent to which it resembles the true experimental geometry, is found to be important.

4.1 Model-independent approach: practical considerations

A variety of practical considerations can affect charge density measurement using the model-independent approach applied to phase images recorded using off-axis electron holography, including the mean inner potential, the diffracting condition and the thickness profile of the specimen, the spatial resolution and the signal-to-noise ratio (SNR) of the recorded

phase images, electron-beam-induced specimen charging and the influence of sample imperfections (*e.g.*, preparation damage, Ga implantation, oxidation and contamination). Several of these considerations are discussed in the following sections.

4.1.1 Mean inner potential

The MIP of a specimen affects charge density measurements from electron optical phase images because it is associated with the presence of effective local dipole layers at the specimen surface [103]. Fig. 4.1a shows part of a phase image of the apex of an unbiased W nanotip. The nanotip is surrounded at its end by a layer of amorphous oxide and/or contamination. Fig. 4.1b shows the projected charge density calculated directly from the Laplacian of the phase image using Eq. 2.7. This approach invariably results in a noisy image. Local variations in specimen thickness and MIP are visible in the form of dipole layers, both at the specimen edge and at the boundary between the W core and the surrounding amorphous layer. Fig. 4.1c shows line profiles of the cumulative charge obtained by integrating the signal in Fig. 4.1b across the marked rectangles. The red profile from the amorphous layer alone in region B shows either a peak or a dip at the specimen edge, whereas the green profile from region A shows additional similar features at the boundaries between the W core and the amorphous layer. The line profiles confirm that the MIP contributes additional effective negative or positive local charge wherever the specimen thickness or the MIP changes [41]. Reassuringly, the total charge (given by the difference between the left and right sides of the line profiles in Fig. 4.1c) is zero, indicating that in the present example there is no significant electron-beam-induced charging of the W nanotip or the surrounding amorphous layer.

Several approaches can be used to remove the MIP contribution from the measured charge density. For a needle-shaped specimen such as that examined here, the difference could be evaluated between two aligned phase images recorded without and with an electrical bias voltage applied between the specimen and the counter-electrode, in order to measure the charge density distribution in the specimen due to the application of an electrical bias alone. Care is then required to minimise any misalignment between the two phase images, which can result in artefacts in the phase difference image and in the final charge density, in particular at the specimen edge. Fig. 4.2 illustrates the influence of misalignment between two phase images on the measurement of the charge density in the W nanotip, in the form of cumulative charge profiles evaluated from phase difference images (Figs. 4.2a-b) that were calculated from deliberately misaligned phase images. The cumulative charge profiles, which are shown in Fig. 4.2c, were calculated by applying loop integrals to median-filtered phase difference images that were deliberately shifted with respect to each other by ± 5 pixels along the x axis, as shown in Figs 4.2a and 4.2b. Each line profile shows four distinct peaks or

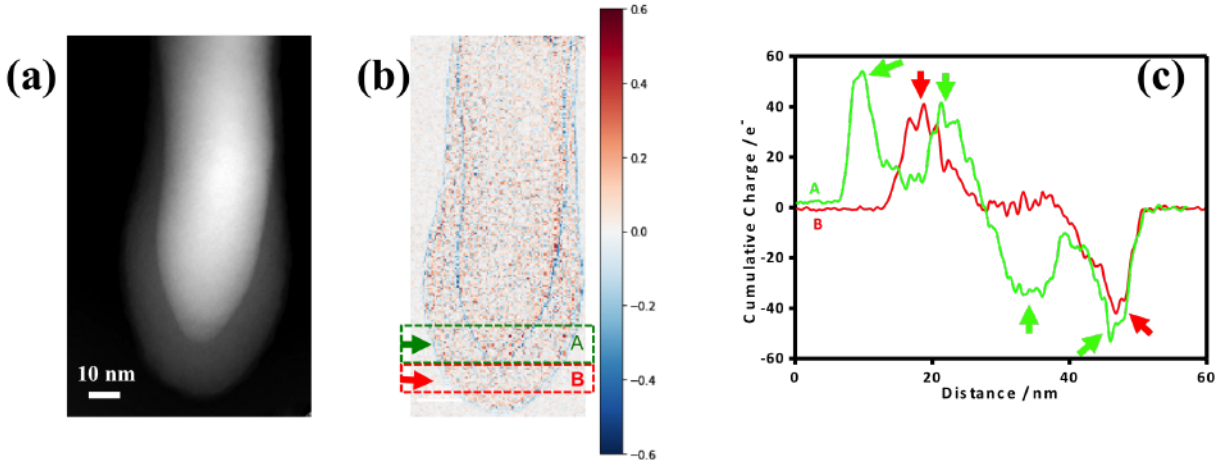

Fig. 4.1 Apparent charge density derived from the MIP contribution to the phase for an unbiased W nanotip covered by an amorphous layer. (a) Part of a phase image recorded from the apex of the nanotip using off-axis electron holography. (b) Charge density calculated from the Laplacian of the phase (using Eq. 2.7) shown in units of $e/pixel$. An effective band of negative charge is located on the vacuum side of the specimen edge, while an effective band of positive charge is located on its inner side, thereby forming a dipole layer. Similar effective bands of charge are present at the interface between the needle and the surrounding oxide. (c) Cumulative charge profiles corresponding to integrals of the signal in the Laplacian of the phase across regions A (green) and B (red) marked in (b). The line profiles are in practice calculated from loop integrals (using Eq. 2.9) applied to a median-filtered version of the phase (to reduce noise). Arrows indicate the positions of edges or interfaces.

dips at the specimen edge and at the interfaces between the W core and the surrounding amorphous layer. Similar to the influence of the MIP on charge density measurement (Fig. 4.1), the total contribution to the cumulative charge that originates from misalignment of the phase images is zero. However, local artefacts are present within the boundary of the specimen. Accurate alignment between such phase images, often to sub-pixel precision, is therefore essential before evaluating the charge density from their phase difference.

4.1.2 Spatial resolution

The approach used to reconstruct the phase of the electron wave from off-axis electron holograms using an FFT-based algorithm [90] is illustrated in Fig. 4.3 for a W nanotip that was electrically biased at 50 V. Figs. 4.3a-b show the object hologram and vacuum reference hologram, respectively. First, the hologram is Fourier transformed (Figs. 4.3c-d). The Fourier transform contains two side-bands and a centre-band. The two side-bands contain complete information about the electron wave and its conjugate, while the centre-band is, to first order, the Fourier transform of a conventional bright-field TEM image of the specimen. The electron wave can be retrieved by selecting one of the side-bands using a digital (usually circular) mask, centring it and taking its inverse Fourier transform (Figs. 4.3d-e). The position of the centre of the side-band can be determined by using the vacuum reference hologram, as the electromagnetic field from the specimen may alter its position. Figs. 4.3f-h show reconstructed wrapped phase, unwrapped phase and amplitude images, respectively. The spatial resolution of the final reconstructed images is determined by the size of the mask, which is usually chosen to be $\frac{1}{3}$ or $\frac{1}{2}$ of the separation between the centre-band and the side-band for strong and weak phase objects, respectively, which can result in under-sampling of the phase/amplitude image, as well as in the damping of higher-frequency information. This effect is especially pronounced if coarser interference fringes are used to record electron holograms, as they lead to a smaller separation between the side-band and the centre-band and therefore to the need to use a smaller mask size. For example, the peak charge density at a *p-n* junction was shown to be damped when a small mask was used [6]. For this reason, complementary techniques such as in-line electron holography, DPC imaging and ptychography are sometimes better suited to retrieving high frequency phase information about a specimen [104, 77].

4.1.3 Signal-to-noise ratio

Uncertainty in charge density measurement is determined by several factors, including the noise in the original hologram, the sampling density of the phase image and the size of

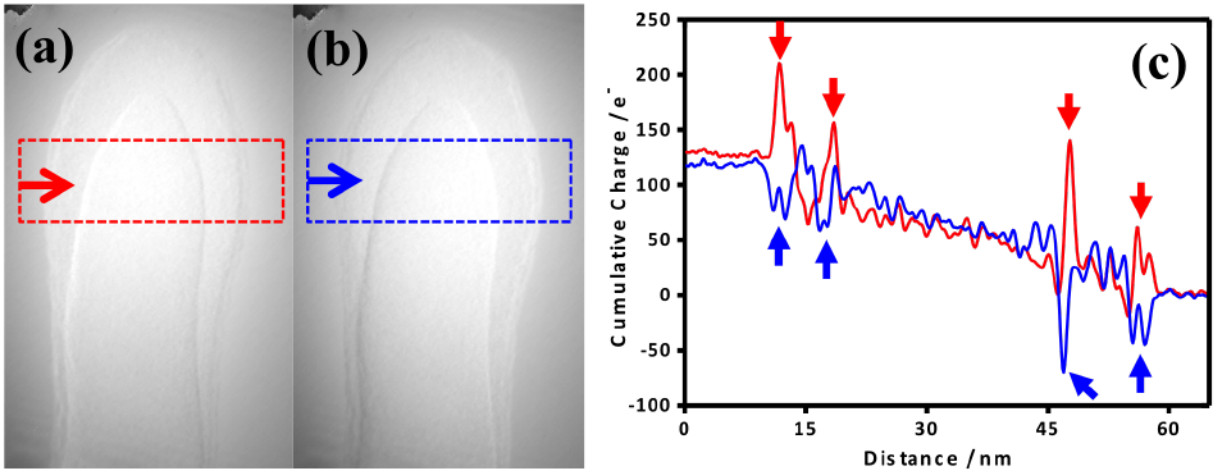

Fig. 4.2 Charge density calculated by applying a loop integral (using Eq. 2.9) to differences between phase images recorded without and with an electrical bias voltage applied to the W nanotip shown in Fig. 4.1. (a, b) The phase image recorded with an applied electrical bias voltage to the nanotip was deliberately misaligned by ±5 pixels along the *x* axis with respect to the phase image recorded without an applied bias before evaluating their difference. (c) Cumulative charge profiles calculated by integrating the signal across the regions marked in (a) and (b). Arrows indicate the positions of edges or interfaces.

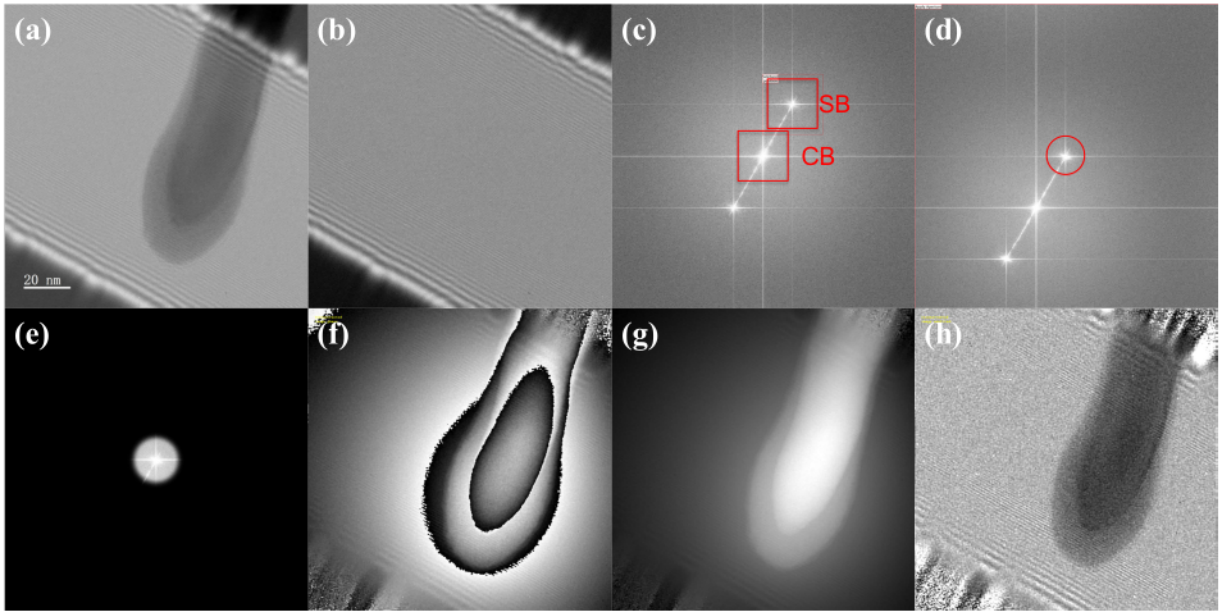

Fig. 4.3 Example of standard FFT-based reconstruction of electron holograms. (a) Object hologram and (b) vacuum reference hologram. (c) Fourier transform of the vacuum reference hologram used to determine the position of the centre of the side-band (SB). (d) Fourier transform of the object hologram, with the centre of the upper side-band shifted to the centre of Fourier space. (e) Circular aperture with a size of $\frac{1}{3}$ of the separation between the centre-band (CB) and the side-band applied to select the area to be used for the inverse Fourier transform. (f-h) Reconstructed images: wrapped phase, unwrapped phase and amplitude, respectively. The specimen is the W nanotip presented in Fig. 4.2 above. The object hologram was recorded with the specimen electrically biased at 50 V.

the integration region used in the loop integral approach. If an experimental phase image is assumed to be a superposition of a noise-free phase image and random normally-distributed noise with zero mean and standard deviation (SD) $\delta\varphi$ (*i.e.*, neglecting scattering absorption in the specimen), then the Laplacian of the phase image can also be treated as a superposition of a noise-free charge density and noise. Here, the relationship between the SD of the measured charge density $\delta\sigma$ and the SD of the phase is derived.

A discrete Laplacian is a one-step matrix algebraic operator that maps each pixel in a phase image $\varphi(i,j)$ onto the value $\varphi(i+1,j)+\varphi(i-1,j)+\varphi(i,j+1)+\varphi(i,j-1)-4\varphi(i,j)$. If this operation is applied to a noisy phase image that has zero mean, then the result is another noisy image, which is also normally distributed and has zero mean (as $1+1+1+1-4=0$), while it has a standard deviation that is $\sqrt{20}$ times larger than the SD of the original image. This description is valid when each pixel is uncorrelated with its neighbours and when the SDs can be added in quadrature, such that $1^2+1^2+1^2+1^2+4^2=20$. The relationship between the SDs of the phase and the charge density can then be expressed in the form

$$\delta\sigma = \sqrt{20}\frac{\varepsilon_0}{C_E}\frac{\delta\varphi}{p^2} = \sqrt{20}\frac{\delta q}{p^2}, \tag{4.1}$$

where p is the pixel size (sampling density) and $\delta q = \frac{\varepsilon_0}{C_E}\delta\varphi$ is defined as the charge noise that is related to the phase noise. For reference, $\delta\varphi$ = 118 mrad corresponds to δq = 1 e at 300 kV. Since experimental values of phase noise are typically well below 100 mrad (in particular when using a direct electron counting camera and averaging multiple phase images), the achievement of single electron sensitivity in charge density measurement is in principle relatively straightforward.

Eq. 4.1 is derived on the assumption of uncorrelated/white noise in the phase image. However, this assumption does not hold for Fourier-transform-based hologram reconstruction, as noise correlations are introduced whenever a chosen sideband is masked using an aperture. Such a mask can take the form of a "soft" window function (*e.g.*, Hann, Gaussian or Butterworth) or a "hard" function (*e.g.*, top hat). Soft apertures are commonly used, as they are more efficient than hard apertures for suppressing phase noise without introducing artefacts in reconstructed phase images. Fig. 4.4 shows a comparison between simulated white noise (*a*, top half), correlated noise resulting from the use of a Gaussian aperture (*a*, bottom half) and experimental noise (*c*) extracted from the vacuum region of a phase image. Correlations are visible directly in the granularity of the noise, which does not match the pixel size. White noise (*b*, upper half) results in a one-pixel-wide diagonal line in the corresponding correlation matrix, while correlated noise (*b*, lower half and *d*) results in a thicker diagonal line, with a profile that decays in proportion to the smoothing parameter that was used to define the reconstruction mask.

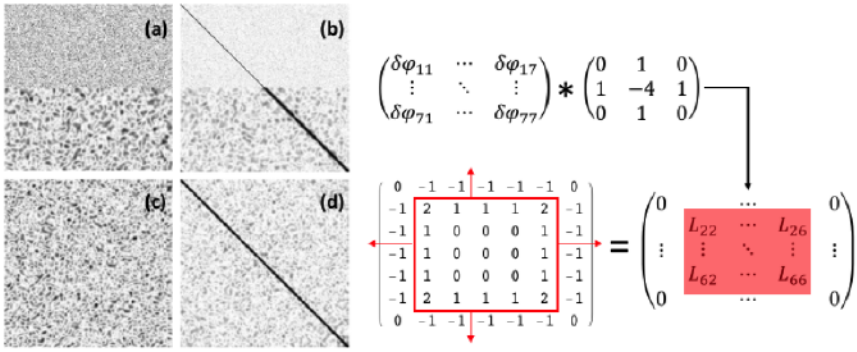

Fig. 4.4 Left: (a) Simulated white (top) and correlated (bottom) noise images. (b) Corresponding simulated correlation matrices. (c) Experimental noise image, extracted from a vacuum region, obtained from the reconstruction of a series of 20 electron holograms. (d) Corresponding experimental correlation matrix. Right: Block diagram illustrating the noise transfer process from phase to charge.

Unfortunately, the calculation of a full correlation matrix for an experimental phase image would require multiple independent measurements, which are not available here. However, on the assumption of isotropic correlations, each column of a single image can be treated as a single vacuum measurement, thereby reducing the problem from two dimensions to one dimension. The resulting reduced correlation matrix is shown in Fig. 4.4d. As a result of the reduced dimensionality, only coefficients c_0, c_1 and c_2 can be derived from this reduced matrix, where c_0 is the auto-correlation coefficient, c_1 is the correlation coefficient between adjacent pixels (*e.g.*, (i,j) and $(i+1,j)$) and c_2 is the correlation coefficient between non-adjacent pixels (*e.g.*, $(i-1,j)$ and $(i+1,j)$). On the assumption of isotropic correlations, a Gaussian fit to these points could be extended to two dimensions, in turn allowing the determination of the c_{11} coefficient, where c_{11} is the correlation coefficient between diagonally-neighbouring pixels (*e.g.*, (i,j) and $(i+1,j+1)$).

Surprisingly, noise correlations are not detrimental to the transfer of noise from the phase image to the charge density. On the contrary, since discrete differential operators involve taking differences between pixel values, covariances contribute to decreasing the transferred noise variance, as parts of the correlated noise cancel out. When a discrete Laplacian operator is applied to correlated noise, the noise transfer factor of 20 in Eq. 4.1 becomes $(20-32c_1+8c_{11}+4c_2)$.

A representative value of the phase noise in vacuum in a phase image reconstructed from a single electron hologram was measured to be approximately 81 mrad (SD). By averaging 20 successive phase images [105], the phase noise was reduced to 17 mrad, in agreement

with the expected $\sqrt{20}$ reduction for uncorrelated noise, as the noise in each hologram was uncorrelated with others in the stack and the averaging procedure does not introduce correlations. When a discrete Laplacian is applied to a selected region of vacuum in the phase image, *e.g.*, to the region shown in Fig. 4.4c, the noise transfer factor is in general lower than $\sqrt{20}$, in agreement with the strong correlations that are visible in the experimental correlation matrix shown in Fig. 4.4d. The relevant correlation coefficients can be extracted from the experimental correlation matrix shown in Fig. 4.4d, leading to values of $c_1 = 0.859$, $c_{11} = 0.746$ and $c_2 = 0.532$. (c_{11} was estimated by applying a second-order polynomial interpolation to $c_0 = 1$, c_1 and c_2). The noise transfer factor thus drops from $\sqrt{20} = 4.47$ to $\sqrt{0.613} = 0.783$. As a consequence, the noise in the charge density calculated using Eq. 4.1 drops from 0.64 e/p^2 to 0.11 e/p^2, in agreement with the experimental value of the SD in the charge density being 0.10 e/p^2.

Integration of the measured charge density reduces noise, although it does not bring it back to the value that it has in the original phase image, both because the integration region is usually smaller than the FOV and as a result of noise correlations. Even if the phase noise is uncorrelated, the charge noise becomes correlated as a result of the use of a discrete Laplacian operator. The right half of Fig. 4.4 illustrates how the SD of the measured charge δQ is related to $\delta\sigma$ and $\delta\varphi$. A simple square 7×7 matrix with noisy pixels $\delta\varphi$ is chosen to represent a selected region of a phase image used for charge density measurement. The discrete Laplacian of this matrix, which is represented by a standard 3×3 kernel, is an edge-padded 5×5 matrix (the evaluation of boundary pixels is neglected for simplicity), in which each pixel value L_{ij} is a linear combination of the original pixel values, as written above (*e.g.*, $L_{44} = \delta\varphi_{34} + \delta\varphi_{35} + \delta\varphi_{43} + \delta\varphi_{45} - 4\delta\varphi_{44}$, *etc.*). Summing these 25 pixels gives another linear combination of pixel values. Isolating the coefficients of each pixel that contribute to the sum and assembling them into a matrix yields what is shown in Fig. 4.4 at the end of the process diagram, which coincides with the discrete representation of the loop integral of the gradient (represented by the $(-1,\ 1)$ kernel) of the original image over the boundary of the chosen region. In addition to providing visual verification of the equivalence of the two methods to measure Q, it confirms that δQ is also identical. Counting the number of pixels that contribute to the measurement of Q and summing them in quadrature (for uncorrelated phase noise) provides the following relationship between the charge density measurement uncertainty and the phase noise:

$$\delta Q = \sqrt{8n}\frac{\varepsilon_0}{C_E}\delta\varphi = \sqrt{\frac{2L}{p}}\delta q, \tag{4.2}$$

where $n \gg 1$ is the number of pixels on one side of the square integration loop and L is the total length of the loop. The noise transfer factor in the case of correlated phase noise becomes $\sqrt{8(1-c_1)n}$, where the only relevant correlations are those between adjacent pixels in the Laplacian. Since these correlations are also the strongest ones, c_1 can be close to unity (it takes a value of 0.714 in the example discussed above), supporting the effectiveness of the charge density measurement scheme with respect to noise despite the use of discrete differential operators.

4.2 Application of model-independent and analytical model-dependent approaches

Several approaches have been proposed for the reconstruction of charge density from electron optical phase images and for removing the effect of the PRW, including the use of finite element simulations (*e.g*, [49]), analytical model-dependent approaches (*e.g.*, [71, 72, 93]) and the model-independent approaches (*e.g.*, [40, 41, 74]). Here, a model-independent approach (as described by Eqs. 2.7 and 2.9) and an analytical model-dependent approach are illustrated and compared through the study of a LaB_6 needle-shaped specimen, which was prepared for use as a field emitter. (See Chapter 3 for preparation details.) An electrical bias voltage was applied *in situ* to the field emitter in the TEM by using an STM-TEM holder (see Chapter 3). A voltage of -50 V was applied between the field emitter and a counter-electrode, which was positioned approximately 6 μm from it. Off-axis electron holograms were recorded at 300 kV in an FEI Titan 60-300 TEM (Fig. 2.1c) on a Gatan K2-IS camera using an exposure time of 8 s. The electron holographic interference width was approximately 1.8 μm and the interference fringe spacing was approximately 2.7 nm, resulting in a spatial resolution of approximately 8 nm.

The upper frame in Fig. 4.5a shows a phase image recorded from the LaB_6 field emitter without an applied electrical bias, corresponding only to the MIP contribution to the phase, *i.e.*, to its projected thickness and shape. The lower right part of the specimen is covered by a region of amorphous contamination. The outline of the entire specimen, including the LaB_6 field emitter and the amorphous region, is marked by a dashed black line. Figs. 4.5b-c show an equivalent phase image recorded in the presence of an electrical bias voltage of -50 V and the difference between the two phase images, respectively. In this way, the MIP contribution to the phase has been removed, according to the approach described in Section 4.1.1. Corresponding phase contour maps, with a spacing of 2π radians, are shown below each phase image. It is apparent that the phase contour map shown in Fig. 4.5a

is not perfectly flat in the vacuum region around the specimen, indicating the needle is slightly charged due to secondary electron emission in the TEM. This electron-beam-induced charging contribution to the total charge density in the specimen is assumed to be independent of the applied bias voltage and to be subtracted together with the MIP contribution to the phase in Fig. 4.5c.

4.2.1 Model-independent charge density reconstruction

Fig. 4.6a shows the projected charge density calculated directly from the phase difference image shown in Fig. 4.5c using Eq. 2.7. As expected, the resulting charge density has poor SNR as a result of the use of a second-order derivative in the form of a Laplacian operator. Fig. 4.6b shows that, after applying a Gaussian filter to the projected charge density, an accumulation of negative charge becomes visible at the edges and the apex of the needle-shaped specimen in the presence of an applied voltage of -50 V. Fig. 4.6c shows a line profile of the cumulative charge along the length of the specimen (in blue) generated by integrating the charge density in Fig. 4.6a parallel to the emitter axis using the approach described in Section 2.1. The integration region is marked by a red dashed rectangle in Fig. 4.6a. The charge in the specimen is negative. The approximately constant slope of the cumulative charge profile suggests that the charge density in each slice of the three-dimensional volume of the specimen of equal thickness is the same, *i.e.*, that it has an approximately linear equivalent charge density on its axis.

4.2.2 Analytical model-dependent reconstruction

A linear line charge model (see Appendix B) was used here to provide an analytical solution for the charge density along the needle-shaped specimen. The shape of the needle was fitted to an ellipsoid of major semi-axis $a = 45\ \mu$m and minor semi-axis $b = 0.6\ \mu$m. The value of K (a constant with the same unit of surface charge density in Eq. B.4 (see Appendix B) was found from a best fit to the phase difference image shown in Fig. 4.5c in the vacuum region around the needle. Fig. 4.7a shows a simulated phase contour map corresponding to the best fit for $K = 35\ e/\mu\text{m}^2$. The underlying electric field strength E induced by the counter-electrode and the base on which the field emitter sits can be calculated from Eq. B.5 [72, 93] to be approximately 0.4 MV/m, which is comparable to the electric field generated when 50 V is applied between two infinite plates with a separation of 50 μm. Fig. 4.7b shows a stream plot of inferred electric field lines in the $z = 0$ plane obtained from the best-fitting parameters. The maximum electric field strength at the apex E_{apex} is

Fig. 4.5 Upper row: Phase images recorded from a LaB_6 field emitter using off-axis electron holography, corresponding to (a) the MIP contribution alone; (b) the MIP contribution and the effect of an applied electrical bias voltage of -50 V; (c) Difference between (b) and (c), *i.e.*, the contribution from the applied electrical bias voltage alone. The outline of the specimen, including a region of amorphous contamination at its lower right, is marked using a dashed black line. Lower row: Corresponding phase contour maps, displayed in the form of the cosine of the phase. The phase contour spacing is 2π radians.

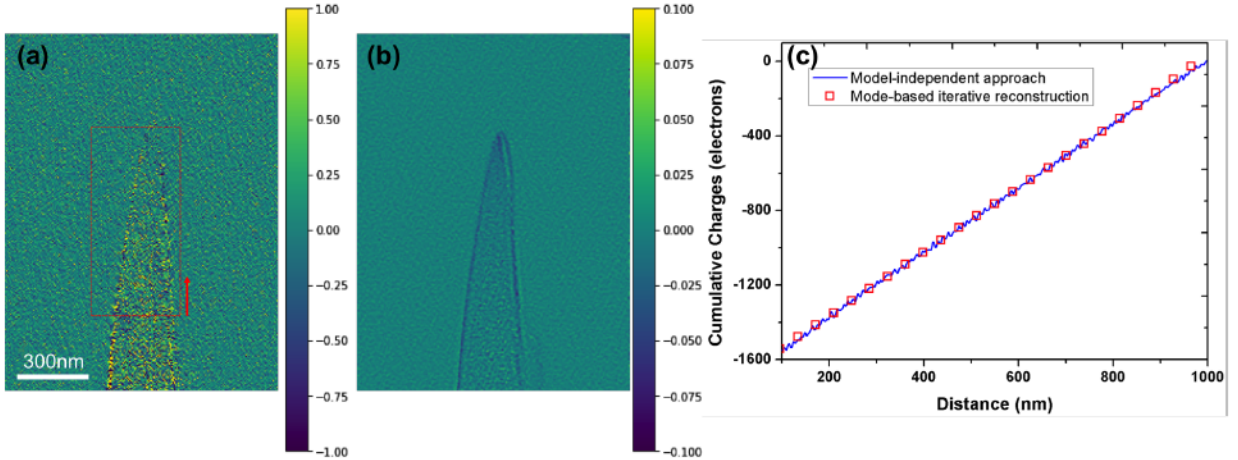

Fig. 4.6 Illustration of the model-independent approach for charge density measurement to a LaB_6 field emitter that is subjected to an applied electrical bias voltage of -50 V. (a) Projected charge density calculated directly from the Laplacian of the phase difference image shown in Fig. 4.5c (using Eq. 2.7). (b) Filtered charge density generated from (a) by using a Gaussian filter with a standard deviation of 5 pixels (4.2 nm). (c) Line profiles of cumulative charge calculated from the results obtained using the model-independent approach (blue line) and numerical model-based iterative reconstruction (red squares; see Section 5.4.6 below). The integration region is marked by a red square in (a).

approximately 3.6 GV/m. The ratio E_{apex}/E corresponds to a field enhancement factor of 9000.

The field emitter studied here was also transferred to a dedicated UHV chamber to measure its field emission properties after the TEM experiments [95]. The electric field at the apex determined from a measured *I*-*V* curve was 2.2 GV/m (see measurement details elsewhere [95]), which is slightly lower than that estimated here. The fact that no field emission current was measured in the TEM may be a consequence of the poorer vacuum level.

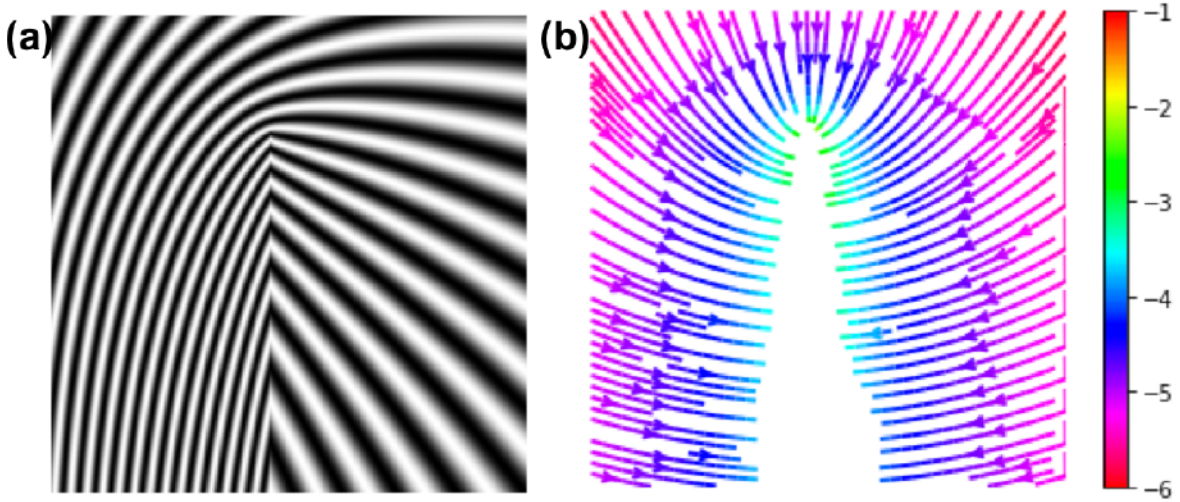

Fig. 4.7 Demonstration of the application of the analytical model-dependent approach for charge density measurement to a LaB_6 field emitter that is electrically biased at -50 V. (a) Phase contour map corresponding to a best fit of a linear line charge model in the vacuum region around the specimen to the experimental phase difference image shown in Fig. 4.5c. The phase contour spacing is 2π radians. (b) Streamlines showing a section through the electric field in the $z = 0$ plane (the central slice of the emitter) calculated from the best-fitting parameters. The colour scale indicates the natural logarithm of the electric field strength. The shadow of the needle is indicated by the white region.

4.3 Discussion

A linear line charge model was used in the analytical model-dependent approach (Section 4.2.2) due to the fact that the equipotential surfaces around such a charge density resemble ellipsoids, which are in turn similar to the physical shape of the needle studied here. The (3D) electric field in the vacuum region around the needle can be calculated directly using existing analytical solutions and there is no need for the measurement of phase information inside the needle. It should be noted that the line charge density used here does not represent the true line charge density along the needle, as in this model the line charge density has a maximum at its foci rather that at its apex. Multiple line charges were used to better approximate experimental phase images in the literature [72, 73]. It should also be noted that a specimen that has a shape of either a perfect ellipsoid (in 3D) or a well-defined simple geometry hardly exists. The true (always complex) geometry of any experimental setup complicates finding an analytical solution for the charge density and phase distribution. A knowledge of the interference distance is also needed to take the presence of the perturbed reference wave effect into account.

The model-independent approach (Section 4.2.1) is the most direct and unbiased approach for retrieving the projected charge density from a holographic phase image and is insensitive to the presence of both the perturbed reference wave and charges outside the field of view. The measured line profile of the cumulative charge along the length of the emitter confirms that it has a constant line charge density. However, the MIP contribution to the phase has to be removed before evaluation using the Laplacian operator. This requirement is sometimes difficult to achieve for specimens that are not electron-transparent or exhibit strong diffracting behaviour. In addition, the measured (projected) charge density can be noisy (since the approach relies on the evaluation of second-order derivatives), further inhibiting reconstruction of the 3D charge density from a tomographic tilt series of 2D (projected) charge density distributions.

Based on these shortcomings of the two existing approaches, in this thesis a numerical model-based iterative approach is developed for the reconstruction of charge density from electron optical phase images, as discussed in Chapter 5.

4.4 Summary and conclusions

In this chapter, examples of practical considerations that influence charge density measurements in the TEM have been described, including the MIP and the thickness profile of the specimen, the spatial resolution of recorded phase images and noise transfer to the recon-

structed charge density. Two existing (model-independent and analytical model-dependent) approaches have been applied to the reconstruction of the charge density in an electrically-biased LaB_6 field emitter. The analytical model-dependent approach can calculate the 3D electric field around the specimen directly if the model is sufficiently accurate to represent the true experimental specimen geometry. This approach also requires a knowledge of the interference distance, in order to include the perturbed reference wave effect into the model. The model-independent approach is the most direct and unbiased approach for retrieving the projected charge density from a holographic phase image and is insensitive to the presence of the perturbed reference wave and charges outside the field of view. However, the measured charge density can then be very noisy (since the approach relies on the evaluation of derivatives), complicating reconstruction of the three-dimensional charge density from a tomographic tilt series of two-dimensional charge density distributions. These shortcomings of existing approaches motivate the development of a numerical model-based iterative approach for the reconstruction of charge density from electron optical phase images.

Chapter 5

Development of model-based iterative reconstruction of charge density from electron optical phase images

This chapter is adapted from one of my own publications [102]. The applicability and accuracy of the analytical model-dependent approach depend on the availability of a suitable model for the charge density in the specimen, whereas the use of a Laplacian operator in the model-independent approach results in poor signal-to-noise ratio in the inferred charge density, as discussed in Chapter 4. In order to tackle these limitations, in this thesis a numerical model-based iterative reconstruction (MBIR) algorithm [106] is adapted and developed to retrieve the best-fitting projected or 3D charge density in a specimen from one or more electron optical phase images. This approach has the significant advantage that it allows additional *a priori* information about the specimen to be incorporated, including a knowledge of the locations of untrustworthy regions in the image, such as regions that contains strong diffraction contrast, as well as a knowledge of the location and shape of the specimen, which can significantly reduce the number of unknowns in the fitted charge density. A similar approach was originally developed for the retrieval of magnetisation distributions from electron holographic phase images [106] and is adapted here for the determination of charge density distributions. When it is applied to the reconstruction of either a 3D magnetisation distribution or a 3D charge density distribution, it can avoid many of the artefacts that are generated when using a conventional backprojection-based tomographic reconstruction algorithm, in particular when limited or incomplete data are available.

5.1 Overview

In general, a forward model can be defined by a function $\mathbf{F} : \mathbb{R}^n \longmapsto \mathbb{R}^m$, which maps a physical quantity onto a set of observable data. Reconstruction of the quantity from the data is then referred to as an inverse problem. The dependence of one or more phase images $\varphi(x,y)$ on the charge density $Q(r)$ can be described by the forward model $\mathbf{F}(Q(r)) = \varphi(x,y)$, in which the physical quantity Q is mapped onto a set of phase images φ, as illustrated schematically in Fig. 5.1. The physical quantity Q can also be linked to the electric field, which is recorded more directly using DPC imaging in the STEM. Although DPC imaging can be described by another forward model, the analysis of DPC STEM data is not addressed further in this thesis.

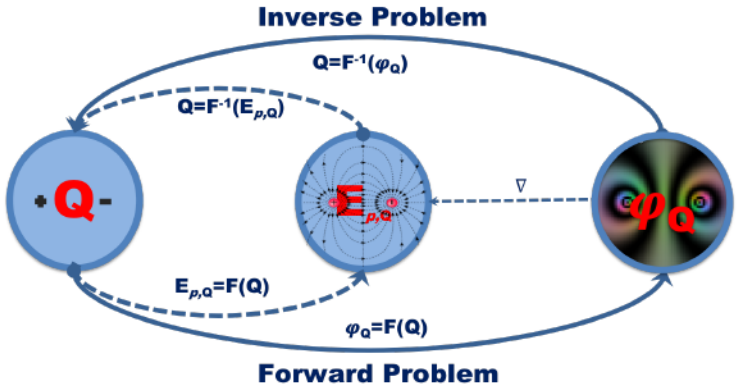

Fig. 5.1 Schematic illustration of the forward and inverse problems that link charge density Q, projected in-plane electric field $E_{p,Q}$ and phase φ_Q. The projected in-plane electric field can be retrieved from the phase with a two-dimensional gradient operator or can be recorded more directly using DPC imaging in the STEM.

A forward model $\mathbf{F}$ can operate, by definition, on vectorised quantities according to the expression

$$\mathbf{F}(\mathbf{x}) = \mathbf{y}, \tag{5.1}$$

where $\mathbf{x}$ and $\mathbf{y}$ represent a concatenation of the pixels in the vectorised charge density in one or more phase images [1], respectively. In the present case, the forward model is linear (*i.e.*, the matrix, $\mathbf{F}$ describing the forward model does not depend on the input charge density) and

[1] Vectorised quantities describing charge density $\mathbf{x}$ and phase $\mathbf{y}$ should not be confused with spatial coordinates (x,y).

can therefore be expressed in the form of a matrix-vector multiplication $\mathbf{F}(\mathbf{x}) = \mathbf{Fx}$. The inverse problem then involves retrieval of the charge density (Q or $\mathbf{x}$) from the phase images (φ or $\mathbf{y}$). However, the solution of Eq. 5.1 for $\mathbf{x}$ may not be generally achievable as a result of the (3D) size of the matrix $\mathbf{F}$ and the fact that it is always not of full-rank (implying an "ill-posed" problem with no (unique) solution [107]). A better-posed problem can be defined in the form of a least-square minimisation of a cost function $\mathbf{C}(\mathbf{x})$, in order to guarantee the existence of a solution, as described by the expression

$$C(\mathbf{x}) \equiv \| \mathbf{Fx} - \mathbf{y} \|^2 + R_\lambda , \tag{5.2}$$

where the regularisation term R_λ can be used to include *a priori* knowledge about the specimen, or other mathematical/physical constraints, into the cost function. In its simplest implementation, the regularisation term can be written in the form

$$R_\lambda \equiv \lambda \, \| \mathbf{x} \|^2 . \tag{5.3}$$

This implementation is a simple Euclidean norm, *i.e.*, a 0^{th} order Tikhonov regularisator [108]. The regularisation parameter, λ, determines its weight over the first term of the cost function, which favours compliance with experimental measurements.

The workflow of the model-based iterative reconstruction procedure is illustrated schematically in Fig. 5.2 (adapted from Ref [106]).

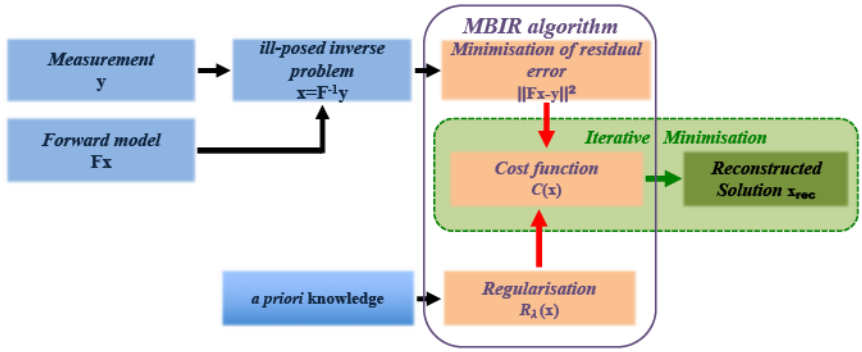

Fig. 5.2 Workflow of model-based iterative reconstruction. A forward model $\mathbf{F}$ maps a physical quantity $\mathbf{x}$ onto a set of observable data $\mathbf{y}$. The ill-posed inverse problem $\mathbf{x} = \mathbf{F}^{-1}\mathbf{y}$ can be solved by least-square minimisation of a cost function $\mathbf{C}(\mathbf{x})$. A regularisation term $R_\lambda(\mathbf{x})$ is used to include *a priori* knowledge about the system. A conjugate gradient algorithm is used to find the best-fitting solution $\mathbf{x}$.

5.2 Forward model

The forward model, which is used to map a chosen charge density onto a corresponding holographic phase image, serves as the basis for iterative reconstruction of the charge density. A simple and easy model that can be implemented in the forward model is an electric dipole, which comprises a point charge $q(x_0, y_0, 0)$ and its image charge $-q(x_0', y_0', 0)$. The electrostatic potential of this electric dipole can be written in the formula

$$V_{dipole} = \frac{q}{4\pi\varepsilon_0}\Big(\frac{1}{\sqrt{(x-x_0)^2+(y-y_0)^2+z^2}} - \frac{1}{\sqrt{(x-x_0')^2+(y-y_0')^2+z^2}}\Big), \tag{5.4}$$

where q is the point charge, (x_0, y_0) and (x_0', y_0') are the positions of the point charge and its image charge, respectively and (x, y, z) are Cartesian coordinates of an arbitrary position.

Integration of the electrostatic potential in the z direction (*i.e.*, the electron beam direction) from $+\infty$ to $-\infty$ provides the measured holographic phase shift

$$\varphi(x,y) = C_E \frac{q}{4\pi\varepsilon_0} \ln \frac{(x-x_0')^2+(y-y_0')^2}{(x-x_0)^2+(y-y_0)^2}. \tag{5.5}$$

Two singularities are present in the above equations. Here, we tackle this problem by treating a single voxel of charge using the analytical expression for a uniformly-charged sphere, which avoids infinities where the charges are located (*cf.* Appendix A). Fig. 5.3 shows a simulated phase image and a corresponding phase contour map of such a dipole, in which the charges are separated by a distance of 32 nm, for a pixel size of 1 nm.

By making use of Eq. 5.5, the forward model can be split into the projection of the charge density in the electron beam direction and a subsequent phase mapping operation, which can be described by a convolution. In discretised form, the projection and convolution can be implemented in two steps, which can be described in matrix form by the expression

$$\mathbf{y} = \mathbf{F}\mathbf{x} = \mathbf{M}\mathbf{P}\mathbf{x}, \tag{5.6}$$

where the matrix $\mathbf{F}$ is split into a projection matrix $\mathbf{P}$ and a convolution matrix $\mathbf{M}$, $\mathbf{x}$ is the charge state vector (*i.e.*, $Q(x,y,z)$ in vectorised form) and $\mathbf{y}$ describes the calculated phase images (*i.e.*, $\varphi(x,y)$ in vectorised form). The projection step can be implemented efficiently by employing sparse matrix calculations, in particular for projection in the electron beam direction. In order to optimise the second step, the convolution kernels (*cf.*, Eq. 5.5) can be pre-calculated in real space, thereby allowing fast convolutions to be used in Fourier space [106, 109].

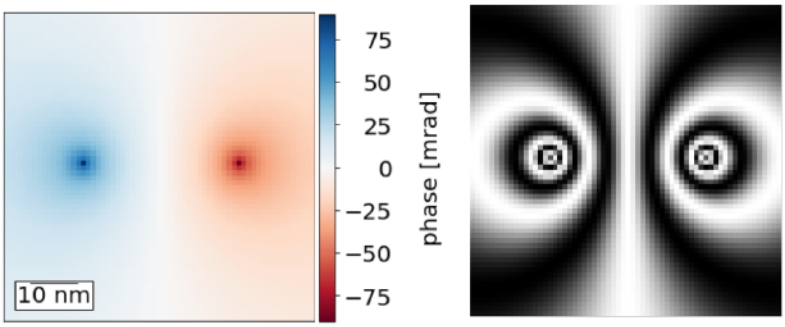

Fig. 5.3 Simulated phase image (left) and corresponding phase contour map (right) calculated for an elementary positive point charge and its image charge separated by a distance of 32 nm. The phase contour spacing is $2\pi/300$ radians. The pixel size is 1 nm. The field of view is 64 nm $\times$ 64 nm.

5.3 Regularisator

Regularisation allows *a priori* information to be included in the inverse algorithm. One of the regularisators that can be used here is based on the minimisation of the total electrostatic potential energy W of all of the charges, which can be expressed in the form [110]

$$W = \frac{1}{8\pi\varepsilon_0}\sum_i\sum_j \frac{q_i q_j}{|\mathbf{r_i}-\mathbf{r_j}|}(i \neq j), \tag{5.7}$$

where q_i, q_j and $\mathbf{r_i}$, $\mathbf{r_j}$ are the magnitudes and positions of the i,j-th charges, respectively. The charges interact with each other through the Coulomb force, which turns the linear term in Eq. 5.3 into a non-linear one. In an ideal metal, in which charges are located only on the specimen surface, Eq. 5.7 can be reduced further to

$$w = \frac{\varepsilon_0}{2}\sigma^2, \tag{5.8}$$

where w is the energy density and σ is the surface charge density. Minimisation of the total electrostatic potential energy is a physical constraint that could be used to restrict the reconstruction of the charge density. In order to enforce this physical constraint, a 0^{th} order Tikhonov regularisation, which corresponds to a scaled identity matrix in the regularisation term, is used in this thesis. The regularisation term is then exactly Eq. 5.3, *i.e.*, a Euclidean norm. Although charges do not necessarily need to be located only on the specimen surface, 0^{th} order Tikhonov (*i.e.*, Euclidean norm, Eq. 5.3) regularisation is used here as it aims to minimise the overall charge, which also has a physical meaning.

In this thesis, the following constraints are used: the application of a mask to define the region that can host charges (*i.e.*, the location of the specimen itself); the application of a confidence mask to define trustworthy regions in the experimental phase image(s); the enforcement of physical or mathematical constraints by implementing a 0^{th} order Tikhonov regularisator in the cost function.

5.4 Charge density reconstruction in projection

The reconstruction of charge density is first demonstrated in projection from a single phase image, as this is a less complicated problem than 3D reconstruction of charge density from a tomographic tilt series of phase images. It is also informative for the study of low-dimensional materials, *e.g.*, nanowires and nanotubes. The parameters that can affect the fidelity of the reconstruction of the charge density include:

- The mask that defines regions that can host charges.
- The measurement noise in the phase image and the chosen regularisation strength.
- Other artefacts in the phase image.
- The presence of charges outside the field of view.
- The perturbed reference wave.

In order to evaluate the influence of each of these parameters, a simulated projected charge density image was generated from the uniform charge density on the surface of a finite hollow sphere, as shown in Fig. 5.4. The sampling density is 1 nm/pixel, the inner and outer radius of the hollow sphere are 30 and 34 nm, respectively and the FOV is 128 nm $\times$ 128 nm. The image charges (whose positions are defined by the counter-electrode position) are situated (1, 1) mm away, such that the positions of image charges and real charges are symmetrical with respect to the counter-electrode. The charge density in the central slice ($z = 0$) of the original 3D charge density is shown in Fig. 5.4a, with a charge of 2×10^{-3} electrons in each pixel. The total charge in the entire shell is 100 electrons. The projected charge density (along the z axis) is shown in Fig. 5.4b. A line profile extracted across its centre ($x = 0$), which contains features resulting from discretisation, is shown in Fig. 5.4c. Fig. 5.5 shows a corresponding phase image calculated using the forward model.

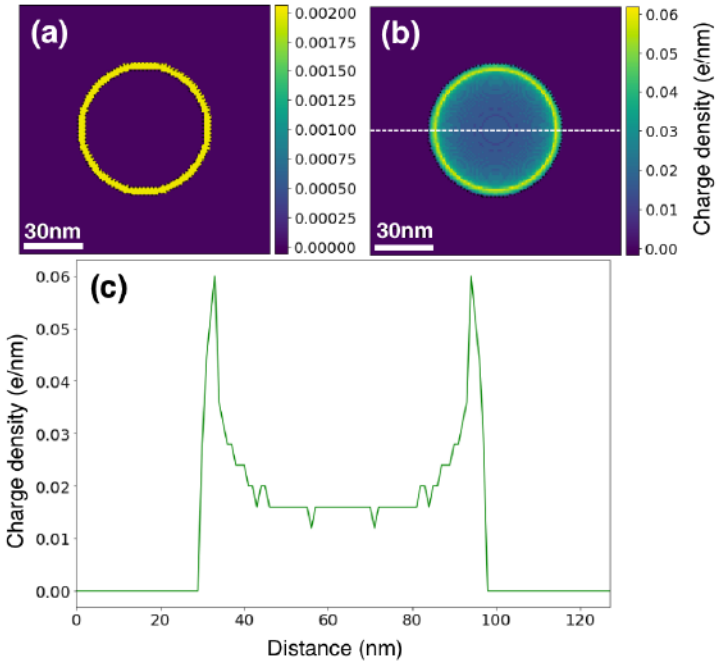

Fig. 5.4 Surface charge density on a hollow sphere: (a) Charge density in the central slice ($z = 0$); (b) Projected charge density along the z direction; (c) Line profile along the marked central line ($x = 0$) in the projected charge density in (b). The field of view is 128 nm × 128 nm.

5.4.1 Mask

A mask can be used to include *a priori* information about the specimen geometry, *i.e.*, about the possible positions of the charges. It can result in a significant reduction in the number of unknowns, as well as in an improvement in the quality of the reconstruction. Although a mask can be implemented as a term in the cost function, here we apply a mask by excluding selected regions from the charge state vector $\mathbf{x}$, *i.e.*, by assuming a charge of zero in these regions. The algorithm does not fit regions outside the mask. Differences between input and reconstructed projected charge density calculated from the phase image shown in Fig. 5.5 with and without using a mask are shown in Fig. 5.6. When a mask is not used, the error in the reconstructed charge density (defined by the deviation from the input charge density, same below) can be as large as 10%, while the error in the reconstructed phase can be as large as 150 μrad (not shown). In addition, ripple-like artefacts are present in the reconstructed charge density (top panel in Fig. 5.6). In contrast, when a mask (marked by the

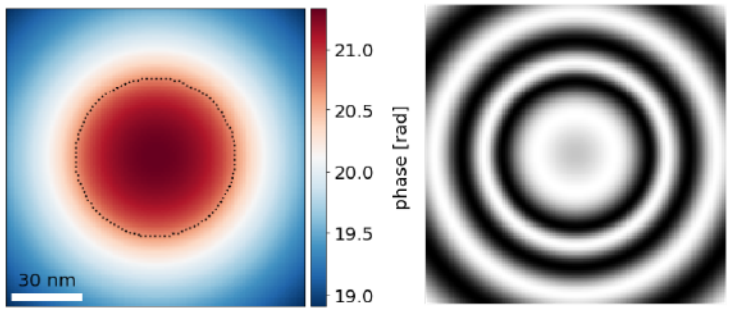

Fig. 5.5 Phase image (left) and corresponding phase contour map (right) calculated from the projected charge density shown in Fig. 5.4b. The dashed line in (a) marks the edge of the sphere. The phase contour spacing is $\frac{2\pi}{8}$ radians. The field of view is 128 nm $\times$ 128 nm.

dashed circle, also shown in Fig. 5.5) is used, the error in the reconstructed charge falls to below 1%, and the error in the phase falls to approximately 15 μrad (not shown). Moreover, the above ripple-like artefacts are now absent.

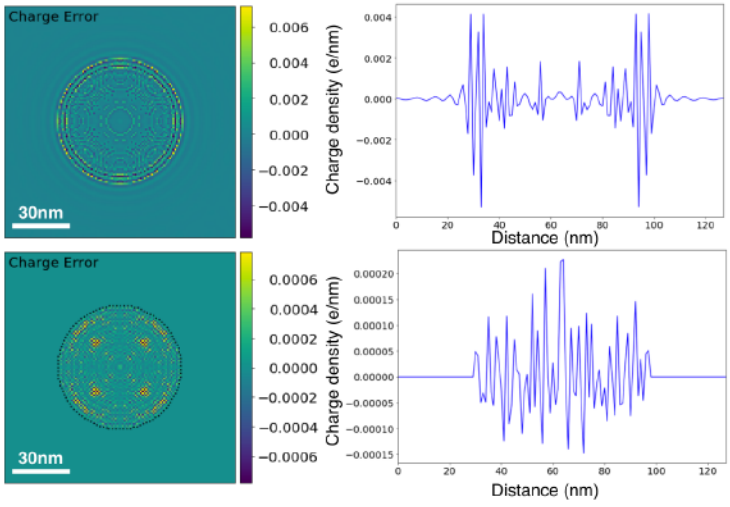

Fig. 5.6 Difference between the reconstructed charge density and the input charge density shown in Fig. 5.4b, first in the absence (top) and then in the presence (bottom) of a mask that defines the position of the specimen. Corresponding projected charge density profiles across the centre of the sphere are shown on the right. Note the different vertical scales. In each case, 1000 iterations were used for reconstruction. See text for details.

5.4.2 Gaussian noise and regularisation strength

The noise in an experimental phase image depends on several factors, including the choice of detector (*e.g.*, CCD camera or direct electron counting camera) and averaging scheme (*e.g.*, single hologram acquisition or multiple hologram averaging). In the presence of noise, the reconstruction of a phase image without using a regularisator can result in a charge density that deviates greatly from the original input. A 0^{th} order Tikhonov regularisator is therefore used here.

As discussed in Section 5.1, the regularisation strength, which is controlled by the regularisator parameter λ, determines the ratio between the residual norm vector (the first term on the right of Eq. 5.2) and the regularisation term (Eq. 5.3). If $\lambda \to 0$, then the regularisation term vanishes (or is not used in the extreme case) and the cost function depends solely on the residual norm vector, resulting in high frequency noise in the reconstructed charge density. If $\lambda \to \infty$, then the cost function only favours the regularisation term and the reconstructed charge density diverges greatly from the experimental measurement. An optimal choice of regularisation parameter λ, which should correspond to a balance between compliance with the measurements and enforcement of *a priori* constraints, can be found from an L-curve plot [111], as illustrated in Fig. 5.7. Such a plot shows the normalised regularisation term $\frac{1}{\lambda}||\mathbf{x}||^2$ plotted as a function of the residual norm vector $||\mathbf{Fx}-\mathbf{y}||^2_{S_\varepsilon^{-1}}$ on a double logarithmic scale. (See Section 5.4.3 below for details of the weighted matrix S_ε^{-1}.) Fig. 5.7 is calculated from the simulated phase image shown in Fig. 5.5, with an added Gaussian noise level of 0.05 rad. This noise level is representative of that in experimental phase images. The almost-vertical part of the L-curve plot, for smaller values of λ, corresponds to the reconstructed charge density being dominated by high frequency noise or perturbations. The formation of a quasi-plateau for larger values of λ corresponds to the smoothing of high frequency noise or perturbations. The optimal value of λ is located at the corner of the L-curve plot, at which the vertical line transitions into a plateau. This value corresponds to a balance between compliance with the experimental measurements and smoothness of the reconstructed charge density.

In the present example, the optimal value of λ is determined to be approximately 5, resulting in the reconstructed charge density shown in Fig. 5.8. At the edge of the mask, the reconstructed charge density deviates by 50% from the original input charge density, while elsewhere inside the mask the error is below 5%. The phase error is below 1%. The underlying reason for a greater deviation at the edge may possibly originate from the use of a 0^{th} order Tikhonov regularisator and needs further investigations in the future. Fig. 5.9 shows the influence on the reconstructed charge density of using different regularisation parameters λ of 0.5 and 50. For $\lambda = 50$, the charge density is smoothed heavily (upper left

image and blue profile at the bottom of Fig. 5.9), whereas for $\lambda = 0.5$, the charge density is noisy (upper right image and green profile at the bottom of Fig. 5.9).

The algorithm is insensitive to the presence of an arbitrary phase offset and an arbitrary linear phase ramp. Care in the application of the algorithm and in the interpretation of the result therefore is required if a real phase ramp is present across the FOV.

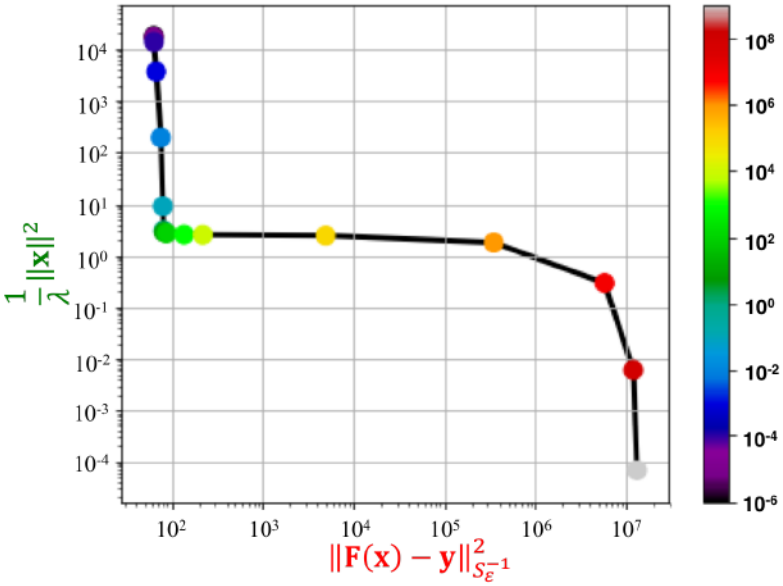

Fig. 5.7 L-curve analysis used for the reconstruction of the projected charge density shown in Fig. 5.4. A good estimate for the optimal regularisation parameter λ is 5. See text for details.

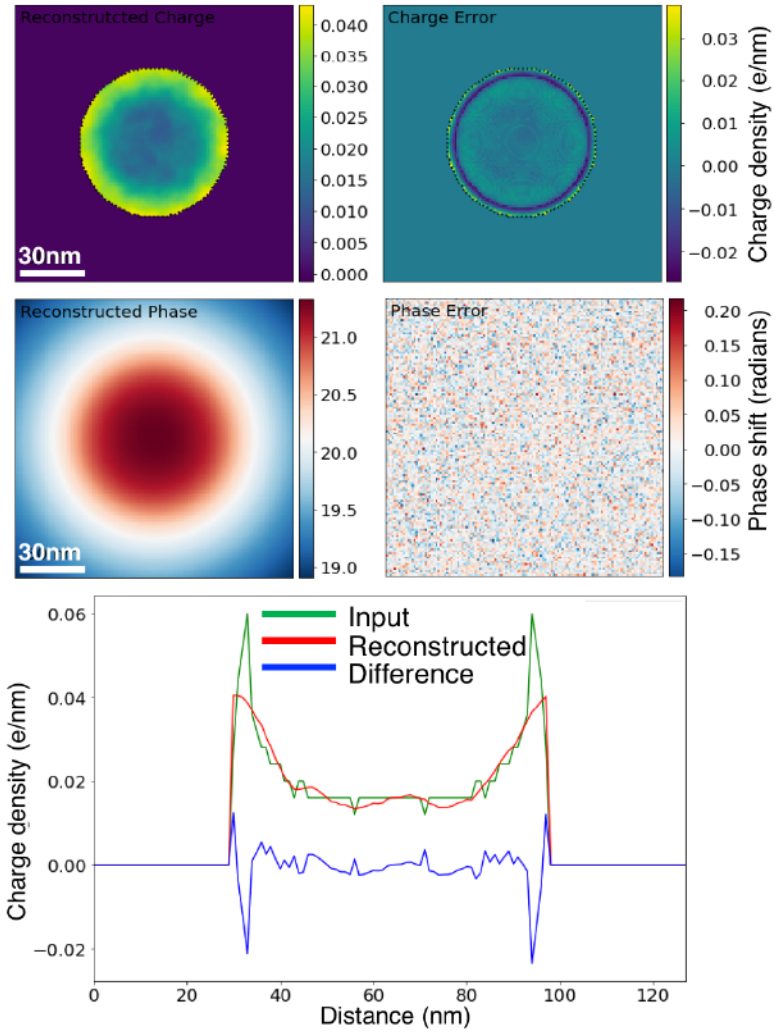

Fig. 5.8 Reconstruction of projected charge density from the phase image shown in Fig. 5.5 with Gaussian noise of 0.05 rad added. A regularisation parameter λ of 5 was used. The reconstructed projected charge density (left) and its deviation from the input projected charge density (right) are shown in the upper row. The reconstructed phase (left) and its deviation from the input phase (right) are shown in the middle row. The field of view is 128 nm $\times$ 128 nm. The projected charge density profile across the centre of the image ($x = 0$) extracted from the reconstructed (red) and input (green) charge density distributions and their difference (blue) are shown in the lower row.

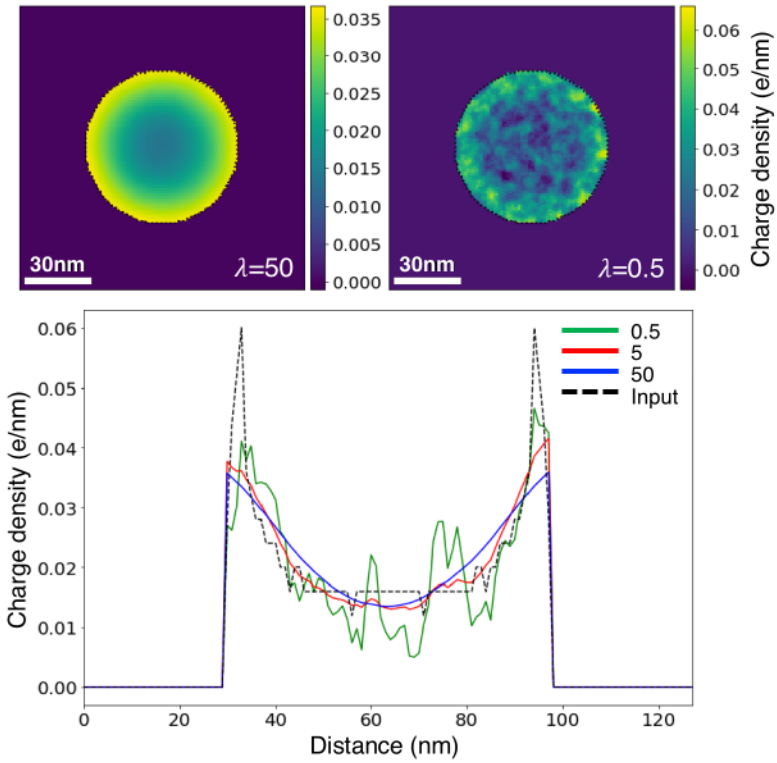

Fig. 5.9 Comparison between reconstructed projected charge density distributions from the phase image shown in Fig. 5.5 for regularisation parameters λ of 50 and 0.5 (upper row). The field of view is 128 nm $\times$ 128 nm. The lower panel shows projected charge density profiles across the centre of the sphere for the input projected charge density (black) and reconstructed projected charge density distributions for three different regularisation parameters: 0.5 (green), 5 (red) and 50 (blue).

5.4.3 Confidence mask

Experimental phase images usually contain artefacts, which may originate from the specimen (*e.g.*, unwanted effects of dynamical diffraction, contamination or electron-beam-induced charging), from the microscope (*e.g.*, distortions or instabilities), from the detector (*e.g.*, under-sampling or dead pixels) or from image analysis (*e.g.*, imperfect scaling or misalignment of phase images in magnification, position or rotation before evaluating their difference). For instance, it may not be possible to remove the contribution to the phase everywhere across the FOV associated with electron-beam-induced charging of the specimen,

or some parts of the specimen may be too thick for electrons to penetrate through it. For all of these reasons, a confidence mask is useful for defining the confidence with which the signal in each pixel in a phase image can be trusted. Regions that contain fully trustworthy values of phase are assigned a value of 1, while other regions are assigned smaller values. A weighted norm is used to calculate the cost of the residuals. The weighting matrix $\mathbf{S}_{\varepsilon}^{-\mathbf{1}}$ is a diagonal matrix, with each entry on the diagonal corresponding to a single pixel in the phase image. These values correspond to entries in the confidence matrix. If its confidence value is 0, then the corresponding residual does not contribute to the cost function, whereas if its confidence value is 1 then its residual contributes fully to the cost function. The weighted norm therefore takes the form $||\mathbf{Fx}-\mathbf{y}||^2_{S_{\varepsilon}^{-1}}$.

Fig. 5.10 shows a reconstructed result assuming that all of the pixels in the charged region (*i.e.*, inside the charged sphere) are untrustworthy. The reconstructed projected charge density is then determined only by the phase outside the charged sphere and is found to deviate significantly from the input charge density (see upper images and the projected charge density profiles at the bottom). Interestingly, even though the charge density cannot be reconstructed reliably, the retrieved phase outside the charged sphere is almost consistent with the input phase in this region (see middle images), implying that the projected electric field can still be retrieved correctly outside the sphere even without phase information from within the boundary of the specimen itself. This result is anticipated, as the algorithm should always deliver a unique solution (mathematically) for a given type and strength of regularisation. However, without information about the phase inside the specimen, reconstruction of the charge density inside it cannot be unique. For instance, the charge density on the surface of a metallic ellipsoid produces the same electric field outside the ellipsoid as a line of constant charge density located on its axis [71]. This result is consistent with a general property of the homogeneous Laplace equation that values that lie with the domain volume depend solely on values or their derivatives on the domain boundary. The possibility of being able to reconstruct the electrostatic potential and field outside a specimen without a knowledge of the phase information inside it has significant implications for applications such as characterisation of the electric fields of electrically-biased needle-shaped specimens that are of interest for atom probe tomography, for which the electric field outside the specimen rather than the charge density inside it is of primary interest for the calculation of ion trajectories. Whereas the DPC STEM technique could be used to directly record images of the projected in-plane electric field, an argument in favour of reconstructing the charge density from an off-axis electron hologram before using it to calculate the projected electric field is that it is localised inside the specimen rather than spreading outside the FOV and can therefore be uniquely reconstructed in 3D.

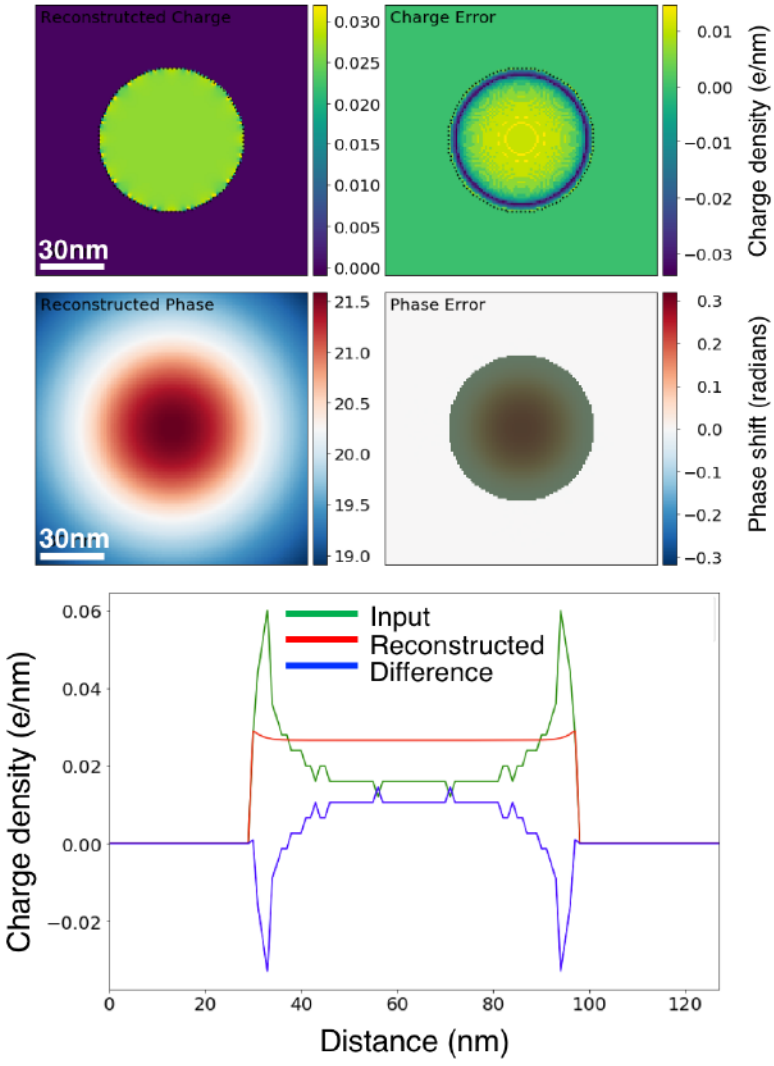

Fig. 5.10 Reconstruction of the projected charge density shown in Fig. 5.4 when using a confidence mask that specifies that the phase in the entire charged region (*i.e.*, within the boundary of the sphere) is untrustworthy. The upper panel shows the reconstructed projected charge density (left) and its deviation from the input charge density (right). The middle panel shows the phase determined from the reconstructed charge density (left) and its deviation from the phase calculated from the input charge density (right). The field of view is 128 nm $\times$ 128 nm. The bottom panel shows projected charge density profiles across the centre of the sphere: input (green), reconstructed (red) and their difference (blue).

5.4.4 Charges outside the field of view

As a result of the limited lateral extent of a phase image, it is generally not possible to include all of the specimen or all of the phase change associated with the charge density inside the FOV. This problem is especially apparent when examining needle-shaped specimens, *e.g.*, atom probe needles and field emitters, whose bases and supports typically extend far outside the FOV.

The uniform two-dimensional shell-like charge density shown in Fig. 5.11 is used to show the effect of charges outside the FOV. The phase of the entire shell (not shown) is initially calculated using the charge density of the full shell (Fig. 5.11a). However, only half of the calculated phase image is used in the reconstruction. The resulting reconstructed charge density, which is shown in Fig. 5.11b, deviates significantly from the original input charge density (Fig. 5.11a), as the algorithm assumes that charges are present only in the masked region, whereas charges outside the FOV also contribute to the phase. Since the forward model does not include any boundary conditions (with the exception of image charges), the presence of charges outside the FOV is tackled here by including additional buffer pixels, which are placed around the edges of the FOV. These buffer pixels can be used to introduce an artificial distribution of charge density around the edge of the image, in order to take into account the influence of unknown charges outside the FOV. They are only used for reconstruction and are discarded when displaying the final reconstructed charge density inside the FOV. In the present example, Fig. 5.11d shows that the reconstructed result is almost consistent with the input charge density when 8 buffer pixels are used around the edge of the image for reconstruction.

5.4.5 Perturbed reference wave

As discussed in Section 2.1, the PRW can prohibit the direct interpretation of holographic phase images if the vacuum reference wave that is used to form the off-axis electron hologram is perturbed by the presence of long-range electrostatic (and magnetic) fields, which originate from the specimen itself. The influence of the PRW can be incorporated in the reconstruction by implementing Eqs. 2.1 and 2.6 in the forward model.

Fig. 5.12 shows a schematic illustration of the influence of the PRW on a recorded phase image for a single positive point charge inside the FOV. In the absence of a PRW, *i.e.*, without the tail of the electric field arising from the positive point charge penetrating into the vacuum reference wave, the measured phase distribution represents the projected electrostatic potential of the positive charge faithfully and is symmetrical. However, the region from which the vacuum reference wave originates may be affected by the electrostatic

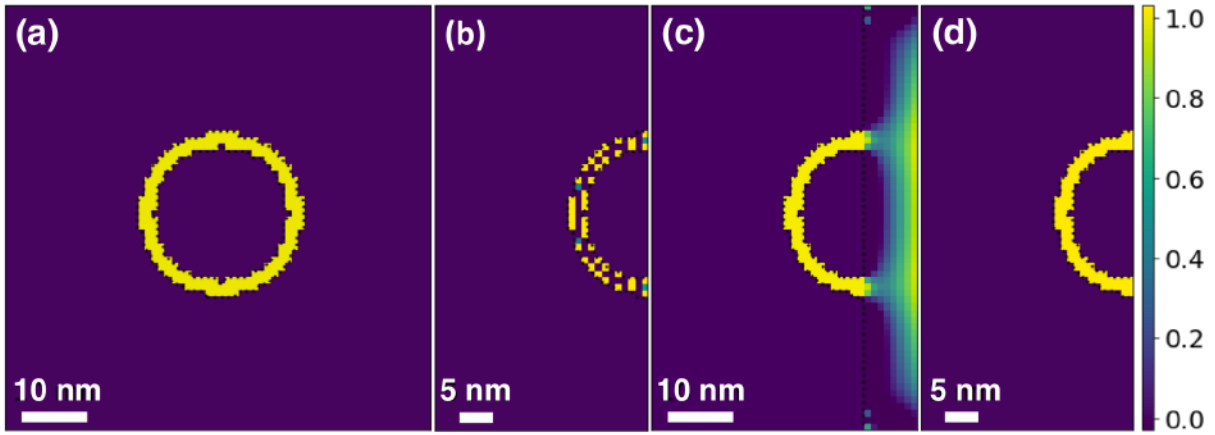

Fig. 5.11 Reconstruction of part of a charge density to highlight the influence of the presence of charges outside the FOV. (a) Uniform 2D shell-like charge density. The field of view is 128 nm × 128 nm. (b) and (c) Reconstructed charge density distributions calculated using only the left half of the phase image; (b) was reconstructed without using any boundary pixels; (c) was reconstructed by allowing additional charge density to be fitted in a boundary region has a width of 8 pixels outside the right edge of the image. (d) Reconstructed charge density inside the FOV from (c) with the 8 boundary pixels discarded. The field of view is 128 nm × 64 nm.

potential of the positive point charge itself, which decays slowly outside the FOV, as shown by the solid red line in Fig. 5.12. The measured phase shift is then given by the difference between the projected electrostatic potential of the charge inside the FOV and the projected electrostatic potential in the vacuum reference wave region. The red dashed line in Fig. 5.12 shows the projected electrostatic potential in the vacuum reference wave region, which has to be added to the projected electrostatic potential inside the FOV with a negative sign to take the PRW effect into consideration. The resulting phase image is asymmetrical with respect to the location of the positive point charge. The red dashed line could equivalently be described as originating from a negative (virtual) point charge located on the other side of the electrostatic biprism, as shown by a solid blue line in Fig. 5.12.

The influence of the PRW can be imagined as resulting from a region of virtual charges of opposite sign (*i.e.*, mirror charges) located on the opposite side of the electrostatic biprism at a distance that is equal to the interference distance. It can therefore be treated either in the same way as any other source of charges located outside the FOV, as described in Section 5.4.4, or by using a modified forward model that incorporates the PRW effect directly.

5.4.6 Reconstruction from an experimental phase image

An experimental phase image recorded from a LaB_6 field emitter that was electrically biased at 50 V (Fig. 4.5c) was used to asses the reconstruction of charge density using the algorithm described in the previous sections. The phase inside as well as outside the emitter was used for reconstruction. The positions of image charges in the forward model were chosen by assuming a distance between the emitter and the counter-electrode of 6 μm. The sampling density of the image is 7 nm. A mask was used to define the specimen, *i.e.*, the positions inside the FOV that are able to host charges. A 4-pixel-wide buffer region was set to host charges around the borders of the image, in order to compensate for contributions from the presence of charges at unknown positions outside the FOV, as well as to take the presence of the PRW effect into account, as described in Sections 5.4.4 and 5.4.5. 0^{th} order Tikhonov regularisation was used. An optimal value for the regularisation parameter λ of 10 was determined from L-curve analysis, as shown in Fig. 5.13.

The reconstructed projected charge density, which is shown in Fig. 5.14a, highlights the fact that charge accumulates around the outer edge of the electrically-biased field emitter (including on the internal boundary between the emitter and the region of contamination visible at its lower right side), but most strongly at its apex. The horizontal band of charge visible at the lower boundary of the image results from compensation for the presence of charges outside the FOV, in particular in the base of the needle-shaped specimen, as described in Section 5.4.4. The cumulative charge profile (red squares in Fig. 4.6c, calculated by

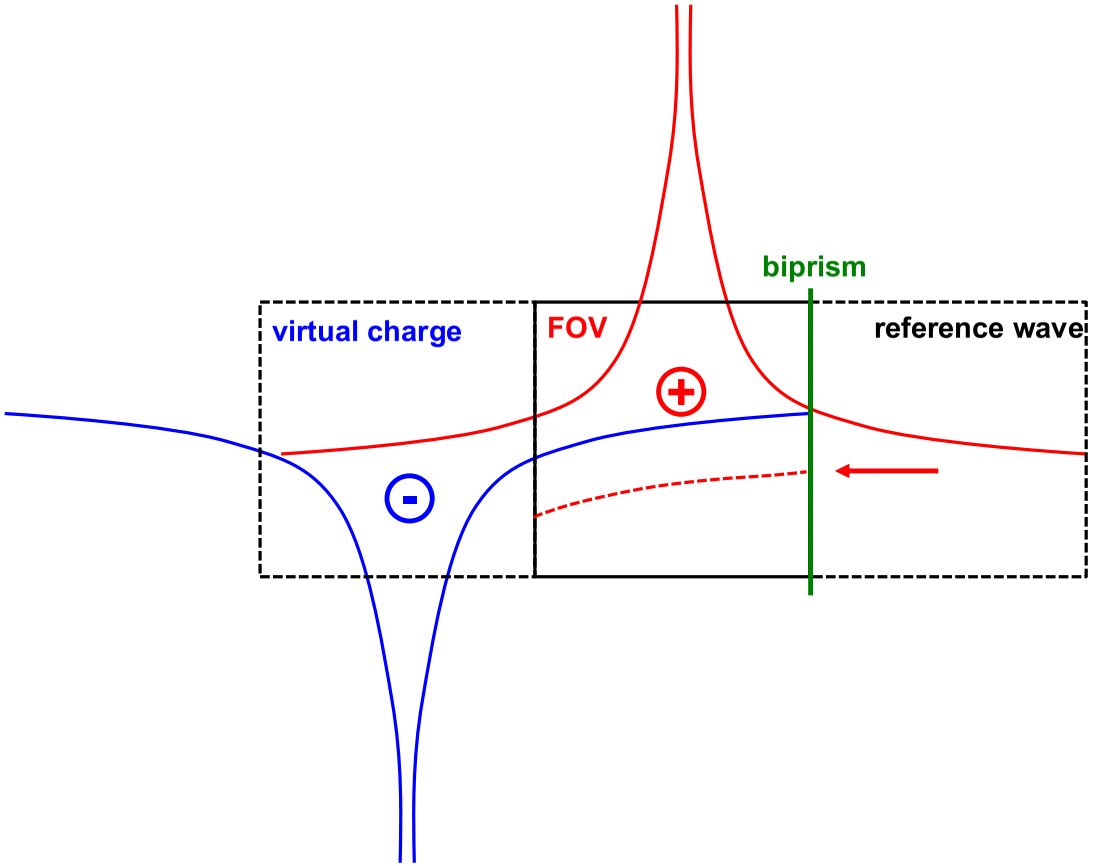

Fig. 5.12 Schematic illustration of the perturbed reference wave effect for a positive point charge, which is located inside the FOV. The tail of its projected electrostatic potential spreads into the vacuum reference wave region, which is defined by the position of the electrostatic biprism (green line) and has the same size as the FOV. The red dashed line represents the projected electrostatic potential in the vacuum reference wave region, which has to be added to the potential inside the FOV with opposite sign. It can be described equivalently as the projected electrostatic potential of a negative point charge (blue) that is located in a "virtual charge" region. The vertical axis schematically shows the magnitude of the projected electrostatic potential.

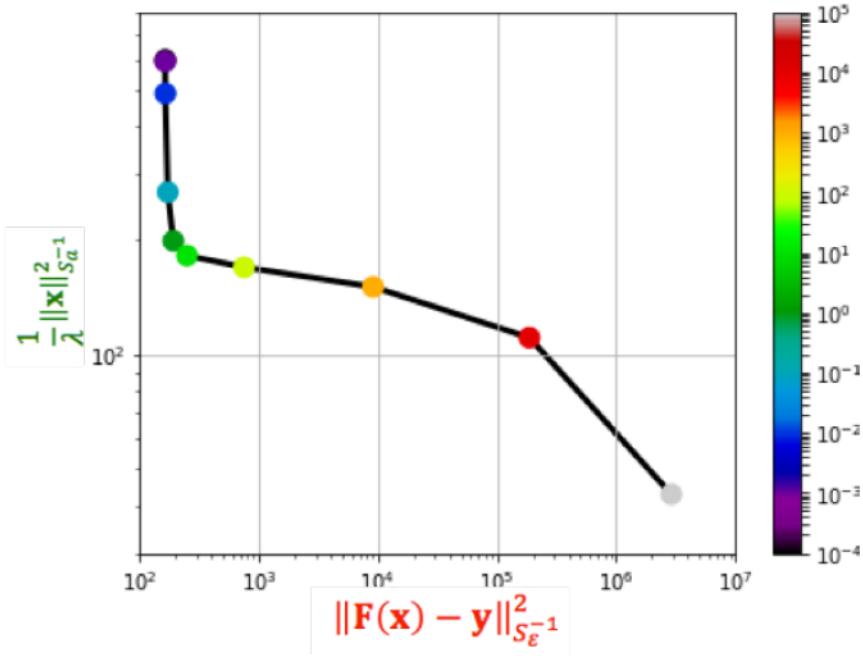

Fig. 5.13 L-curve analysis used for reconstruction of the projected charge density of the electrically-biased LaB_6 field emitter shown in Fig. 4.5c. The optimal value of the regularisation parameter λ is 10.

integrating the reconstructed charge density along the emitter axis) is found to increase linearly and agrees quantitatively with the result obtained using the model-independent approach (Section 4.2.1), as shown in Fig. 4.6. This agreement provides confidence in the MBIR algorithm. Although the reconstructed phase deviates slightly from the original experimental phase image (Figs. 5.14c and 5.14d), this discrepancy is at a level of below 1% and may result from a slight error in the definition of the mask, or from the finite sampling of the phase, especially at the narrow apex of the emitter. Comparing the reconstructed charge density (Fig. 5.14b) with that obtained from the Laplacian of the phase (Fig. 4.6a), it is clear that the noise in the reconstructed charge density is greatly suppressed as a result of the use of *a priori* knowledge (in particular, the mask and the choice of regularisation parameter). However, it should also be noted that the reconstruction depends strongly on the values of several input parameters, which should be chosen with great care when implementing the MBIR approach.

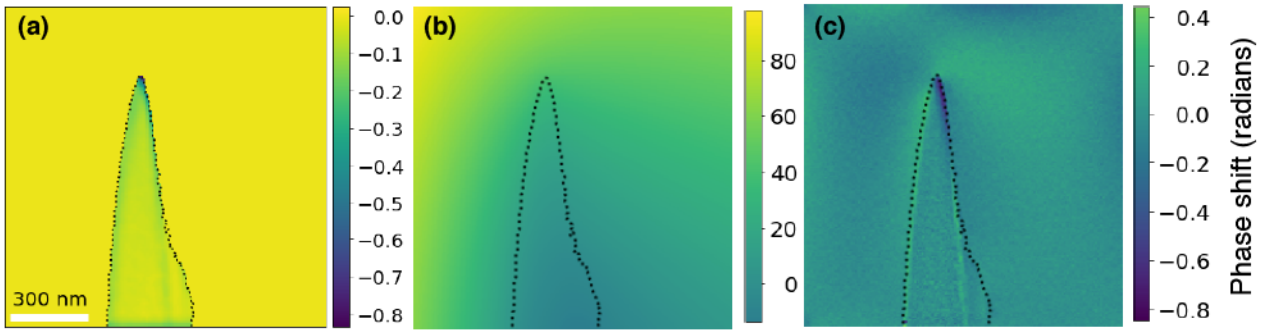

Fig. 5.14 Reconstruction of projected charge density from an experimental phase image of a needle-shaped LaB_6 field emitter that was electrically biased *in situ* in the TEM at 50 V, from which the MIP contribution to the phase had been subtracted (Fig. 4.5c). 0^{th} order Tikhonov regularisation was used for reconstruction. (a) Reconstructed projected charge density, shown in units of *e*/pixel. (b) Phase image determined from the reconstructed projected charge density. (c) Difference between the reconstructed phase shown in (c) and the experimental phase image shown in Fig. 4.5c. Note the different intensity scales in (b) and (c).

5.5 Charge density reconstruction in three dimensions

The 3D charge density can in principle be reconstructed using both the model-independent approach and the numerical MBIR approach by applying standard backprojection-based tomographic reconstruction algorithms to projected charge density distributions reconstructed as a function of specimen tilt angle. However, the MBIR approach also allows the 3D charge density to be reconstructed directly, while making use of all of the constraints and *a priori* information described above. It should be noted that the reconstructed 3D charge density is affected by all of the aforementioned choices of parameters and sources of error, as well as by errors in the mutual alignment of images across the entire tilt series, tilt axis determination, incompleteness of experimental datasets and geometrical image distortions.

5.5.1 3D mask

The influence of using a 3D mask on the reconstruction of 3D charge density is first illustrated for the uniform charge density on the surface of a hollow sphere, as shown in Fig. 5.4. A corresponding calculated phase image is shown in Fig. 5.5. As the charge density is symmetrical, phase images recorded in any direction are identical. Gaussian noise of 0.05 rad was added to each phase image in the simulated tomographic tilt series of phase images. The tilt angle range was chosen to be $\pm 50^{\circ}$ about a single axis ($x = 0$ across the centre), as this is representative of the tilt range that can be accessed experimentally. The tilt increment between successive phase images was 10°, resulting in an input dataset for the MBIR algorithm of 11 phase images in total. Three different 3D masks were used: the shell, the outer surface of the sphere and the full 3D volume. 0^{th} order Tikhonov regularisation was used and the regularisator parameter λ was set to 100 for all three cases.

Figs. 5.15 and 5.16 show 2D slices and line profiles through the reconstructed 3D charge density distributions. It is anticipated that the use of a shell mask, which defines the true positions of the charges should deliver the best results. If only the outer surface of the sphere is chosen as a mask, then the algorithm is expected to retrieve the main features of the charge density (the homogeneous surface charge density) correctly. However, the reconstructed charge density is then expected to be smoothed slightly into the volume of the sphere and to exhibit oscillations inside the shell region. This behaviour is observed in Figs. 5.15 and 5.16. If the full 3D volume is used, then the basic features of the charge density are reproduced (see Fig 5.16), but additional spreading of the charge density and high frequency artefacts are present across the entire FOV. Although further work is necessary to fully optimise the use of the MBIR approach for the reconstruction of 3D charge density, the present results are highly encouraging.

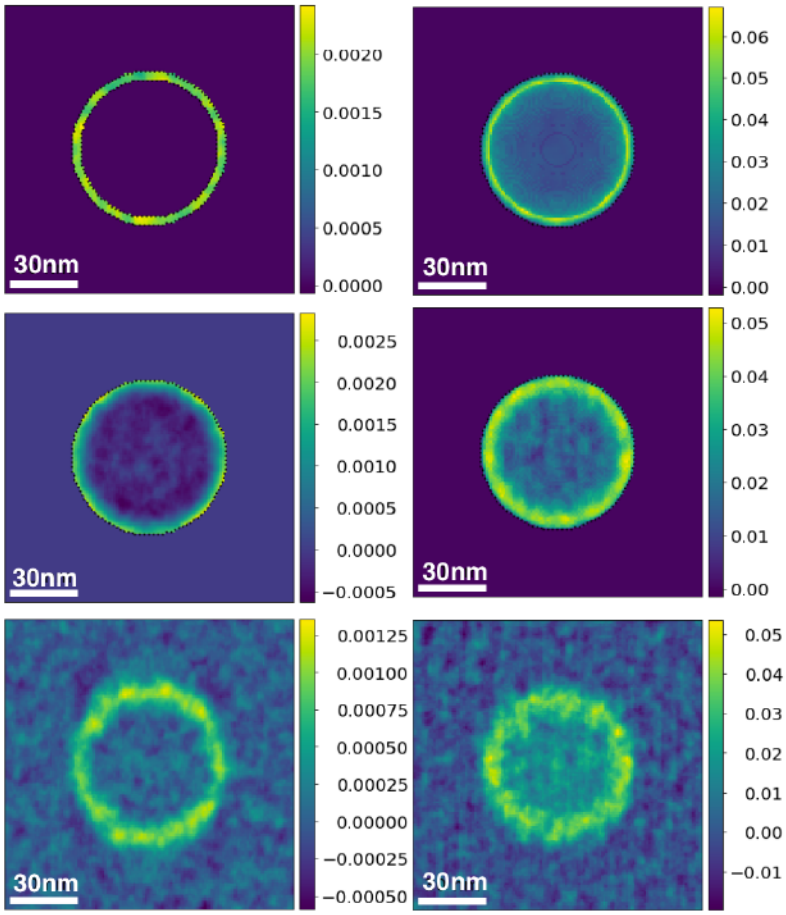

Fig. 5.15 Reconstruction of 3D charge density using the MBIR approach from a tilt series of 11 simulated phase images of uniform surface charge density on a hollow sphere, shown in units of e/nm. Gaussian noise of 0.05 rad was added to each phase image in the tilt series. The tilt angle range was chosen to be $\pm 50°$ about a single axis ($x = 0$ across the centre). The tilt increment between successive phase images was 10°. The regularisation parameter λ was set to 100. Different 3D masks were used to define the possible location of the reconstructed charge: a shell that defines the original charge density (upper row); the outer surface of the sphere (middle row); the full 3D reconstruction volume (lower row). The left column shows the reconstructed charge density in the central slice ($z = 0$), while the right column shows the corresponding projected charge density. The field of view is 128 nm $\times$ 128 nm.

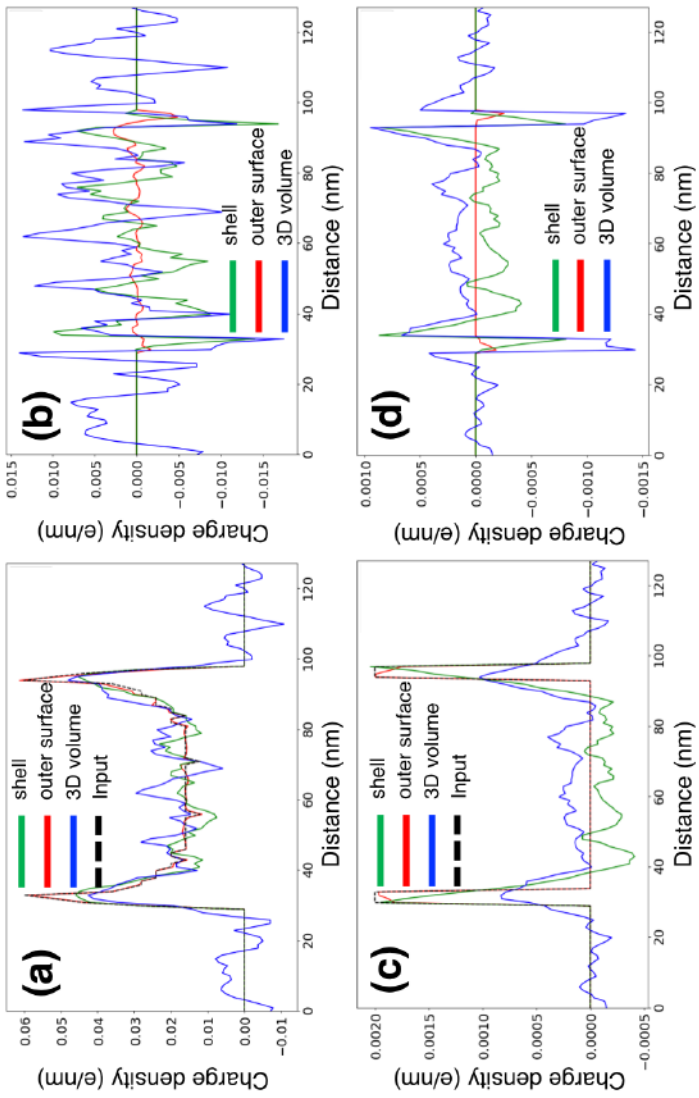

Fig. 5.16 (a, c) Line profiles extracted from the reconstructed charge density distributions and (b, d) differences from the input charge density in Fig. 5.15(a, b). The profiles in (a, b) are extracted across the centres ($x = 0$) of the projected charge density distributions, while the line profiles in (c, d) are taken from central slices of the 3D volumes ($z = 0$; $x = 0$).

5.5.2 3D buffer pixel approach

The use of a 3D buffer pixel approach (*cf.* Section 5.4.4) to compensate for the presence of charges outside the FOV and for the PRW effect is now assessed.

Uniform surface charge density on a hollow sphere was again considered. In order to reduce the computation time, the reconstruction volume was set to 64 × 64 × 64 pixels. The sampling density is 2 nm. The inner and outer radius of the hollow sphere were set to 15 and 17 pixels, respectively and the charge density was set to 5×10^{-2} electrons per voxel. Charges outside the reconstruction volume (corresponding to another uniform surface charge density on a hollow sphere)) were placed (0, -96) pixels from the centre of the FOV. These charges were also used to assess the PRW effect, as discussed in Section 5.4.5. The resulting calculated phase image with Gaussian noise of 0.05 rad added is shown in Fig. 5.17. The tilt range was chosen to be ±90° about a single axis (the horizontal x axis across the centre of the sphere) with a tilt increment of 15°, resulting in a total of 13 phase images. The 3D mask was chosen to be the 3D outer surface of the sphere, as discussed in Section 5.5.1. A 16-pixel-wide buffer region was used outside each edge of the volume. The regularisation parameter was set to 10.

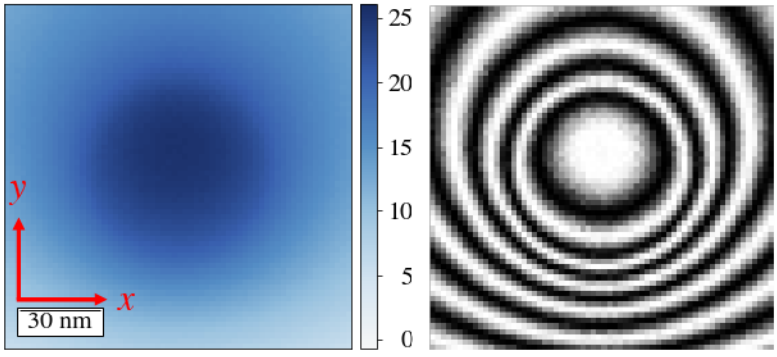

Fig. 5.17 Simulated phase image and corresponding phase contour map generated for uniform surface charge density on a hollow sphere, with additional charges (another uniform surface charge density on a hollow sphere) outside the FOV located (0, -96) pixels from the centre of the FOV. Gaussian noise of 0.05 rad is added to the phase image. The charge density in each voxel is 5×10^{-2} electrons. The phase is shown units of radians. The phase contour spacing is 2π radians. The field of view is 128 nm × 128 nm. The sampling density is 2 nm.

Fig. 5.18 shows the 3D charge density reconstructed using the MBIR approach. Without using buffer pixels, the reconstructed charge density (middle column of Fig. 5.18) shows an

accumulation of charge inside the sphere in the direction towards to the external charges and deviates from the input charge (left column of Fig. 5.18). When using 16 buffer pixels outside each edge, the reconstructed charge density (right column of Fig. 5.18) is now symmetrical, indicating that a 3D buffer pixel approach can be used to compensate for the effects of the PRW and charges outside the FOV. Line profiles along the x (solid line) and y (dashed line) axes for each charge density are plotted in Fig. 5.19. Along the x axis, the charge density is symmetrical. However, it deviates from the input charge density when reconstruction is performed without using buffer pixels (solid blue line). When using buffer pixels (solid green line), it is symmetrical and deviates much less from the input charge density. In the y direction, the charge density is asymmetrical when buffer pixels are not used (dashed blue line). When using buffer pixels (dashed green line), it is symmetrical and comparable to that in the x direction. It should be noted that a "dipole" is present on the surface when no buffer pixels are used (middle column of Fig. 5.18 and blue profiles in Fig. 5.19), probably due to the fact that the algorithm attempts to represent the presence of external charges by setting some *negative* charges in the region (defined by the mask) that are close to the position of the external charges, *i.e.*, the surface of the sphere towards the $-y$ direction. Together with positive charges (as the sphere is positively charged), a "dipole" on the surface is then formed. The use of a 3D buffer pixel approach is therefore essential for the 3D reconstruction of charge density in the presence of significant charges outside the FOV and PRW effects.

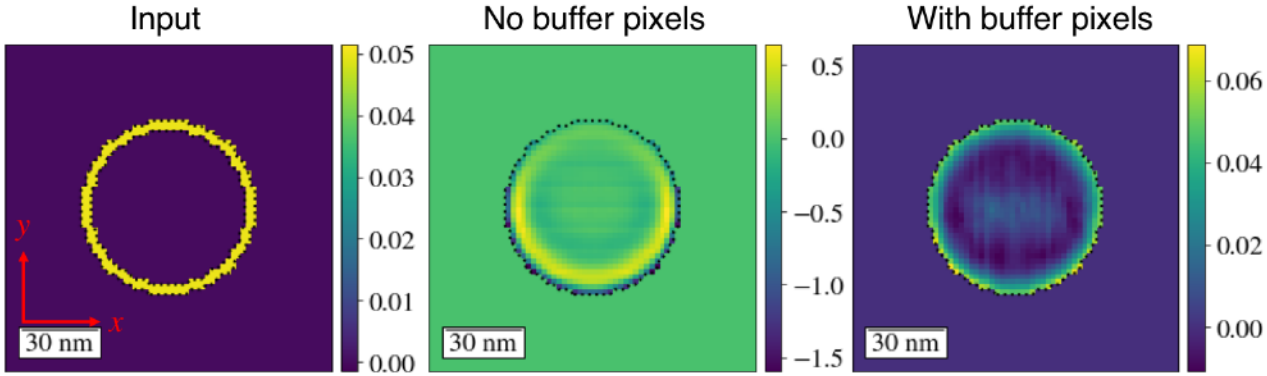

Fig. 5.18 Input charge density (left) and charge density distributions reconstructed without using buffer pixels (middle) and using buffer pixels (right). In each image, the central slice ($z = 0$) is shown in units of e/pixel. Note the different scales in each charge density. The field of view is 128 nm × 128 nm. The sampling density is 2 nm. See text for reconstruction details.

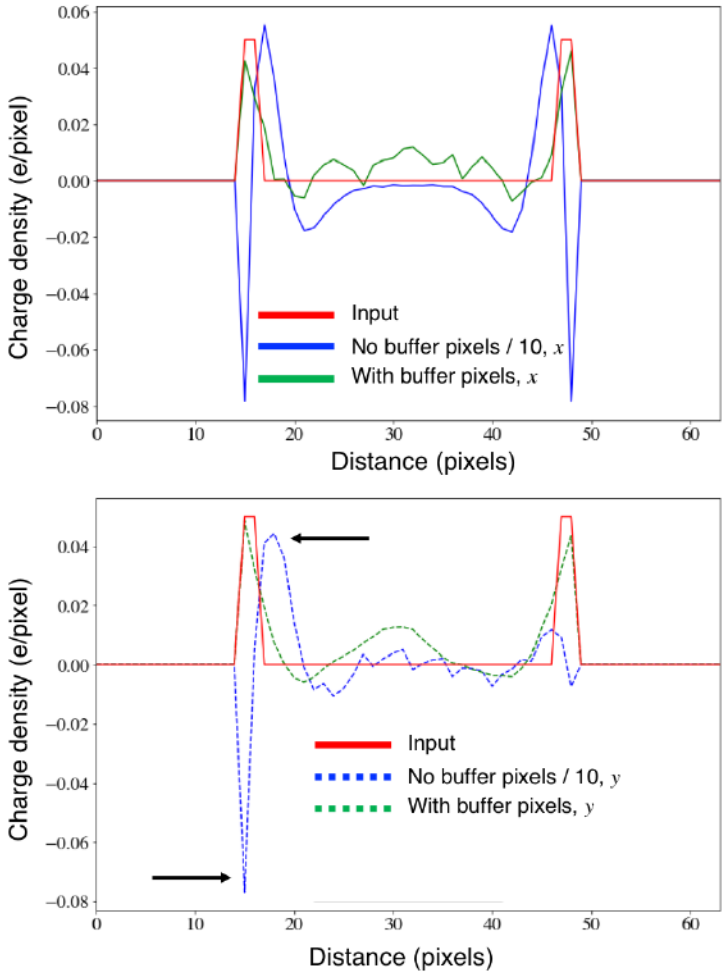

Fig. 5.19 Line profiles extracted along the x (upper frame) and y (lower frame) axes for each charge density shown in Fig. 5.18: input (red), without using buffer pixels (blue) and using buffer pixels (green). The arrows in the lower frame mark a "dipole" on the surface. See text for details. The values reconstructed without using buffer pixels are divided by 10 for better visualisation.

5.6 Uniqueness of reconstruction

In this section, the uniqueness of the reconstructions is discussed for both 2D projected and 3D charge density distributions, with particular emphasis on the MIP contribution to the phase and the use of a confidence mask (*cf.* Section 5.4.3). The same example is considered here as in Section 5.5.2. Reconstructions were performed using the phase across the entire FOV, only inside the sphere and only outside the sphere. The scenario of using the phase across the entire FOV resembles the situation when the MIP contribution to the phase is removed. The use of only the phase outside the sphere resembles the situation when the MIP contribution to the phase has not been removed. The use of only the phase inside the sphere is considered to assess whether this information is adequate to obtain a reliable solution.

5.6.1 Reconstruction of projected charge density

The input phase image shown in Fig. 5.17 was used for reconstruction of the projected charge density. The mask that was used here to define where to allow charges to be placed was the outer edge of the sphere. The regularisation parameter wast set to 1. Fig. 5.20 shows the reconstructed projected charge density obtained by using different regions of the phase image. Use of only the phase outside the sphere results in a solution that deviates significantly from the input. The other reconstructions show an accumulation of charge at the edge of the sphere, which is similar to that in the input. Fig. 5.21 shows corresponding profiles of projected charge density distributions across the centre along the horizontal axis. When only the phase outside the sphere is used, the reconstruction contains uniform charge density inside the sphere (green line in Fig. 5.21). In this case, the algorithm does not fit the phase inside the specimen and selects the smoothest solution that is allowed by the regularisation term. The other two solutions show parabolic projected charge density distribution, similar to that in the input (black line in Fig. 5.21). When the entire phase image is used (red line in Fig. 5.21), the reconstruction is closest to the input. In both cases, the edge regions show the greatest discrepancy from the input.

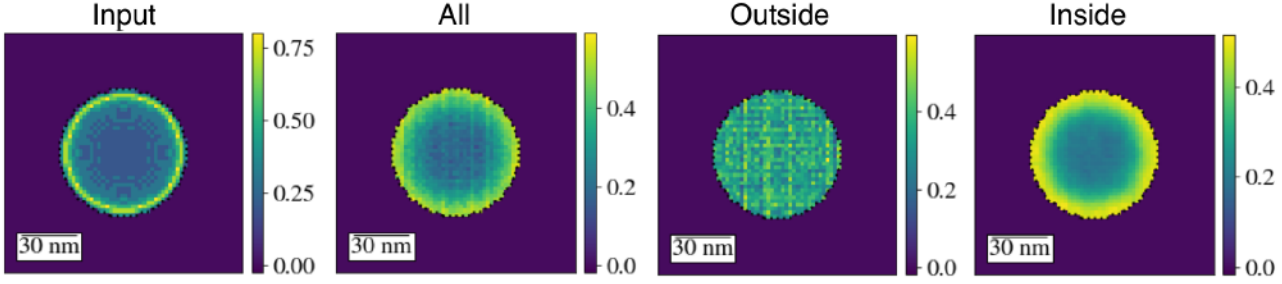

Fig. 5.20 Input projected charge density and projected charge density distributions reconstructed using using the phase across the entire FOV, the phase outside the sphere and the phase inside the sphere, shown in units of *e*/pixel. The input phase image shown in Fig. 5.17 was used for reconstruction. The mask that was used here to define where to allow charges was the outer edge of the sphere. The regularisation parameter was set to 1. The field of view is 128 nm × 128 nm. The sampling density is 2 nm.

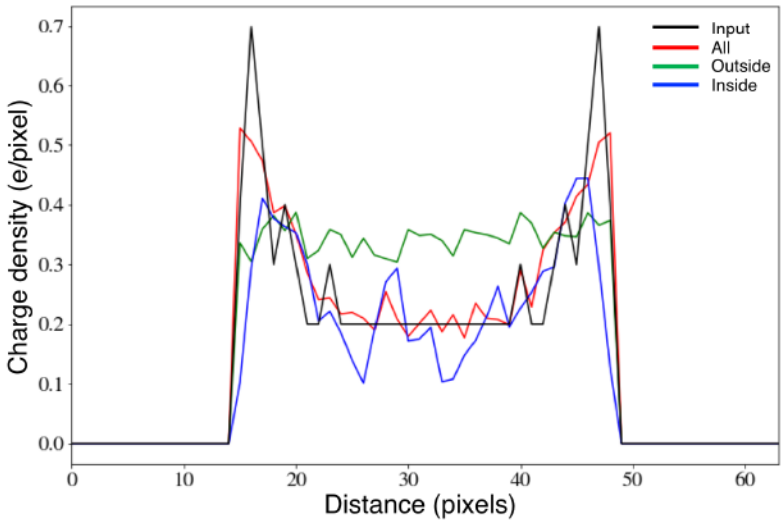

Fig. 5.21 Line profiles extracted from the input projected charge density and from reconstructed projected charge density distributions obtained using the phase across the entire FOV, the phase outside the sphere and the phase inside the sphere (shown in Fig. 5.20) plotted through the centre of the sphere along the horizontal axis.

5.6.2 Reconstruction of 3D charge density

The 3D dataset, comprising a tilt series of phase images, was the same as that used in Section 5.5.2. The mask used here was the outer surface of the sphere. The regularisation parameter was set to 100. Fig. 5.22 shows the reconstructed 3D charge density (central slice $z = 0$) obtained by using different regions of the input phase images. Similar to the situation described above, reconstruction using only the phase outside the sphere results in a solution that deviates significantly from the input. The other reconstructions show an accumulation of charge at the edge of the sphere, which is similar to that in the input. Fig. 5.23 shows corresponding profiles of the charge density in the central slice ($z = 0$). When the phase across the entire FOV or the phase only inside the sphere is used (red lines in Fig. 5.23), the charge density along both the x and the y axis is close to the input (black line in Fig. 5.23). The slight difference in the profiles along the x and y axes is probably associated with the missing wedge, as only one tilt series about the$x$ axis was used for reconstruction. When only the phase outside the sphere was used, the reconstruction again contains a flat charge density in both directions, similar to that obtained for the 2D reconstruction (Section 5.6.1).

Several conclusions can be drawn from the above reconstructions performed both in projection and in 3D: When using only the phase outside the specimen, the true charge density is not retrieved and therefore the (physical) uniqueness of the solution is not guaranteed; when using only the phase inside the specimen, the reconstruction deviates from the input charge density. In all of the cases, the phase outside the sphere obtained from the reconstructions is in perfect agreement with the phase calculated from the input charge density, even though the charge density may be different, confirming that different charge density distributions inside a specimen can result in the same electrostatic potential and therefore the same phase outside the specimen.

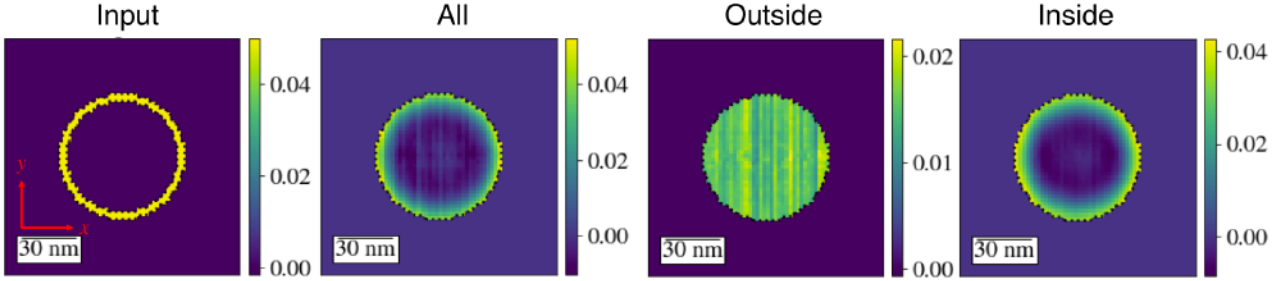

Fig. 5.22 Input charge density and charge density distributions reconstructed using the phase across the entire FOV, the phase only outside the sphere and the phase only inside the sphere. The central slice $z = 0$ is shown, in units of *e*/pixel. The 3D dataset of tilt series phase images was the same as that used in Section 5.5.2. The mask used here was the outer surface of the sphere. The regularisation parameter was set to 100. The field of view is 128 nm $\times$ 128 nm. The sampling density is 2 nm.

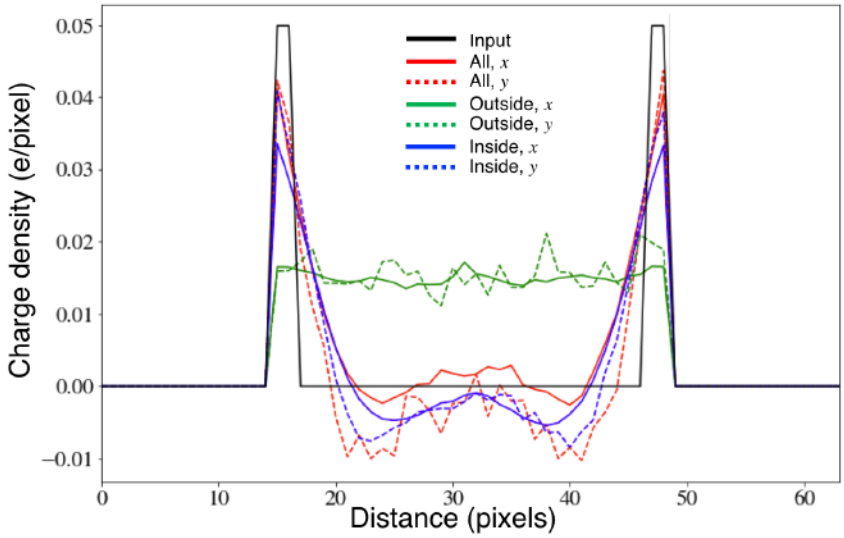

Fig. 5.23 Line profiles extracted from the x (solid lines) and y (dashed lines) axes of the input charge density and reconstructed charge density distributions (shown in Fig. 5.22) in the central slice ($z = 0$).

5.7 Summary and conclusions

In this chapter, a model-based iterative reconstruction algorithm has been adapted and developed to solve the inverse problem of determining the charge density in a specimen from one or more electron holographic phase images. The approach relies on the use of a forward model to create simulated phase images by approximating each voxel as a homogeneously charged sphere and by a mirror charge. The algorithm can incorporate *a priori* knowledge through the use of masks, regularisation parameters and other physical constraints, in order to provide reconstructed charge density distributions that have fewer artefacts and reduced noise. Great care is required in the selection of these parameters to avoid the introduction of artefacts. Boundary buffer pixel regions can be used to take into account the presence of charges outside the field of view and the perturbed reference wave. An experimental phase image was used to test the approach. The result of the reconstruction was found to be quantitatively consistent with the result obtained using the model-independent approach. The charge density on the surface of a hollow sphere was used to test the use of a 3D mask in the reconstruction of 3D charge density, as well as to investigate the uniqueness of the solution through the use of different regions of the input phase images to perform the reconstruction.

In summary, this approach allows additional *a priori* information about the specimen to be included, including the possible positions of charges inside the specimen and untrustworthy regions of the phase images. It allows a regularisation term that can enforce a physical constraint to be incorporated, and can take into account the presence of charges outside the field of view and the perturbed reference wave effect. This approach will be applied to experimental data in the next few chapters.

Chapter 6

Charge density measurement in a W_5O_{14} field emitter

This chapter is adapted from one of my own publications [112]. Field emitters have been used in a wide variety of applications, including as coherent electron sources in electron microscopy (*e.g.*, [42, 24]). There has been considerable interest in exploiting the field emission performance of nanostructures, as a result of the enhanced field strengths at tips that have high aspect ratios, such as nanotubes, nanocones and nanowires [113–115, 47].

Following extensive efforts to develop carbon-based nanostructures, *e.g.*, carbon nanotubes [113] and carbon-cone nanotips [114] for field emitters, tungsten oxide nanostructures, *e.g.*, W_5O_{14}) nanowires [96, 116, 117] and $W_{18}O_{49}$ nanowires [118, 117], are attracting attention due to their promising field emission performance.

Here, the model-based iterative reconstruction algorithm developed in Chapter 5, together with the model-independent approach and the analytical model-dependent approach, are used to measure the charge density along a W_5O_{14} nanowire both before and during field emission *in situ* in the TEM.

6.1 Geometry and experimental setup

Fig. 6.1 shows representative low-magnification SEM images of the W_5O_{14} nanowires studied here. (See Chapter 3 for synthesis details.) Each nanowire typically has a length of several tens of μm and a width of 60-100 nm, as shown in Figs. 6.1a-b. The nanowires have quasi-rectangular cross sections, as shown in Fig. 6.1c.

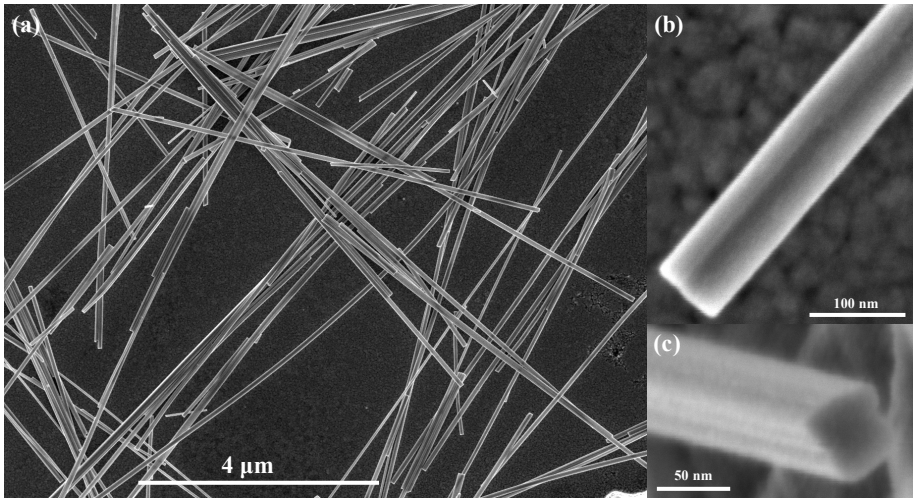

Fig. 6.1 SEM images of as-synthesised W_5O_{14} nanowires. (a) Low-magnification SEM image. (b, c) Higher-magnification images of a single nanowire viewed in longitudinal and cross-sectional directions, respectively. Courtesy of Luka Pirker (Jozef Stefan Institute, Slovenia).

In order to study field emission from an individual W_5O_{14} nanowire *in situ* in the TEM, the electrical biasing setup described in Chapter 3 was used [1]. A 12-μm-long, 100-nm-wide W_5O_{14} nanowire was chosen for detailed examination. (See Figs. 6.2 and 6.3.) This nanowire was attached (using Pt deposition in a FIB workstation) to a sub-μm-sized W wire and mounted onto the fixed side of the TEM specimen holder, while an electrochemically-sharpened μm-sized W wire was used as the counter-electrode and placed on the movable side of the holder. The distance between the nanowire and the counter-electrode was set to approximately 1.5 μm, as shown in Fig. 6.2.

[1] In order to trigger field emission, a negative bias voltage was applied to the nanowire. For simplicity, in this chapter all the descriptions refer only to absolute values of applied bias voltage.

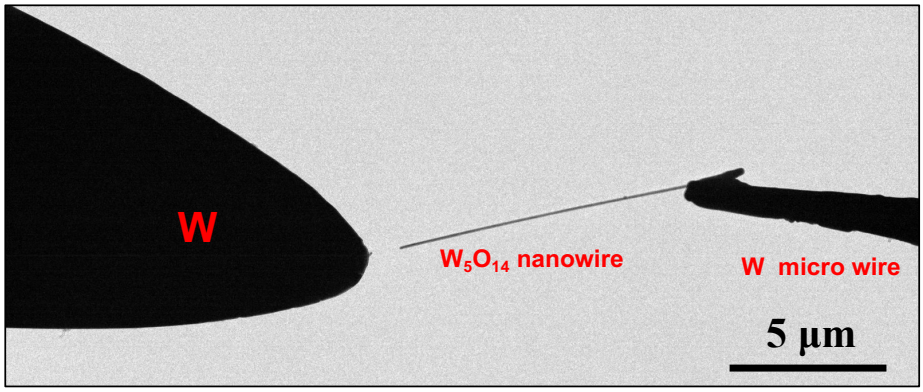

Fig. 6.2 Electrical biasing setup used for field emission from a W_5O_{14} nanowire *in situ* in the TEM. The left side of the image shows a μm-sized W wire, which serves as a counter-electrode. The right side shows a 12-μm-long, 100-nm-wide W_5O_{14} nanowire, which is attached to a sub-μm-sized W wire.

Off-axis electron holograms were recorded using 8 s exposure times with a direct electron counting Gatan K2-IS camera. The holographic interference spacing was 2.4 nm (5.4 pixels), resulting in a spatial resolution of 7.2 nm in reconstructed (phase) images. The interference width was approximately 2.4 μm. Holograms were recorded with the nanowire electrically biased at voltages of between 0 and 200 V. A vacuum reference hologram was recorded far from the nanowire without a bias voltage applied. A representative off-axis electron hologram with the nanowire electrically biased at 150 V is shown in Fig. 6.3. The inset shows a magnified region of interference fringes around the apex region. This nanowire was found to be slightly contaminated/oxidised by an approximately 10-nm-thick amorphous layer. This amorphous layer stayed almost unchanged before and after field emission experiments.

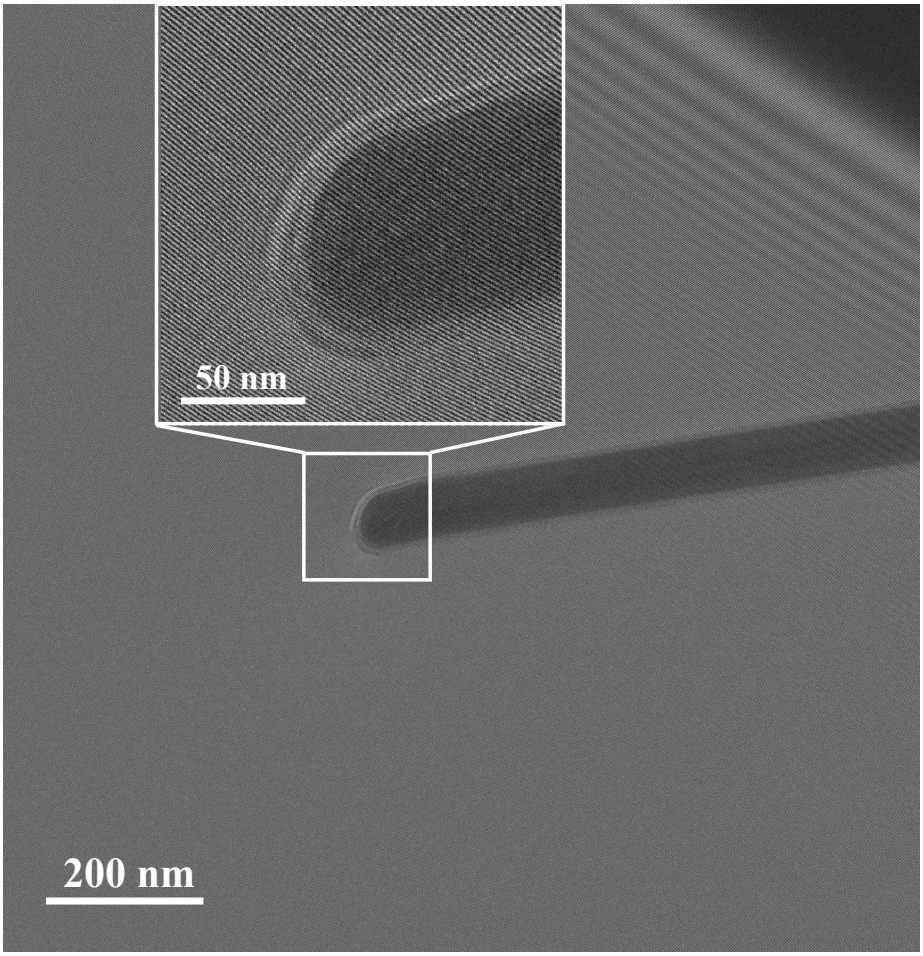

Fig. 6.3 Representative off-axis electron hologram recorded with the W_5O_{14} nanowire electrically biased at 150 V. The inset shows a magnified view of the interference fringes around the apex region, as well as an approximately 10-nm-thick amorphous layer. The holographic interference spacing was 2.4 nm (5.4 pixels) and the interference width was approximately 2.4 μm. The shadow in the upper right of the image indicates the orientation of the biprism.

Fig. 6.4 shows a representative reconstructed phase image (left) and a corresponding phase contour map (right) with the nanowire electrically biased at 150 V. The MIP contribution to the phase was not removed here. The phase shift is in the order of hundreds of radians, which is much higher than the MIP contribution to the phase of approximately 5

radians. The phase increases from the nanowire into the vacuum, indicating that the nanowire is negatively charged. The phase contours in the upper part of the image are less dense than those in the lower part, as a result of the PRW effect, as the electric field penetrates into the vacuum region, from which the reference wave is obtained.

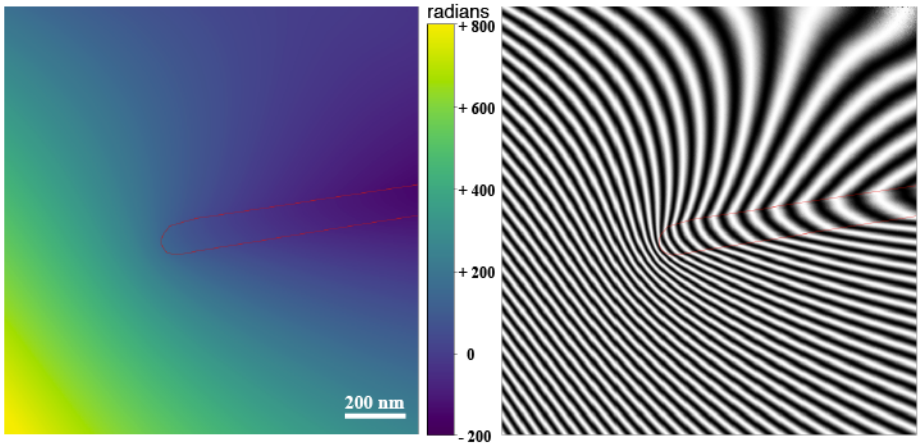

Fig. 6.4 Representative phase image (left) and corresponding phase contour map (right) with the W_5O_{14} nanowire electrically biased at 150 V. The outline of the nanowire is marked by a red line. The phase contour spacing is 8π radians. The MIP contribution to the phase was not removed here.

6.2 Field emission

Fig. 6.5 shows an *I-V* curve measured *in situ* in the TEM from the nanowire shown in Figs. 6.3 and 6.4 using the experimental setup described in the previous section. The nanowire started to field emit at approximately 148 V, when the emission current increased dramatically with applied bias voltage.

The measured emission current was observed to fluctuate with time after the onset of field emission. The magnitudes of the fluctuations are indicated in the form of error bars in Fig. 6.5. This instability may result from the fact that the emitted electrons are not all collected by the counter-electrode, either colliding with the gas atoms in the TEM column or travelling far from the counter-electrode, or alternatively because they are attracted by positively-charged ions. Another possible reason is that the surface of the nanowire changes slightly during field emission due to contamination from gas atoms in the TEM column,

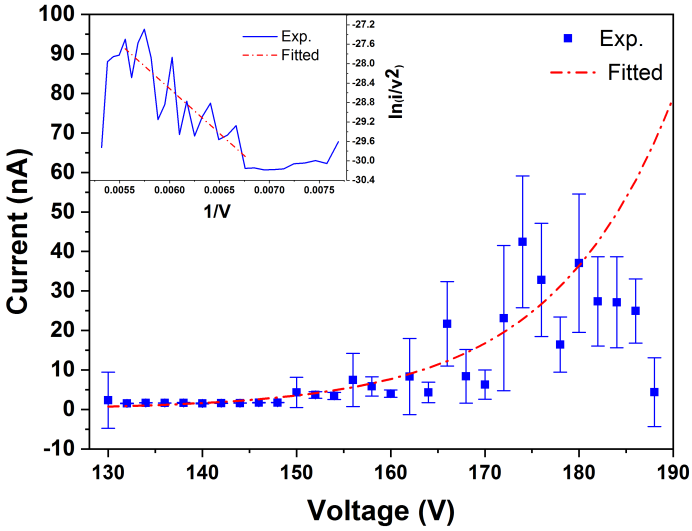

Fig. 6.5 *I-V* measurements of field emission current I as a function of applied bias voltage V for the W_5O_{14} nanowire examined in the experimental setup described in Section 6.1. The red dot-dashed line shows an exponential profile fitted to the data measured between 130 and 180 V. The inset shows a *F-N* plot (blue) of $\ln \frac{I}{V^2}$ plotted as a function of $\frac{1}{V}$ determined from the measured *I-V* data. The red dot-dashed line in the inset shows a linear fit to the points between 148 and 180 V.

the emission of surface atoms, *e.g.*, from the amorphous layer, or the Brownian motion of atoms on the emitting surface [119]. Interestingly, this instability in field emission was not associated with a similar instability in the electrostatic potential or electric field around the emitter, as no double-exposure effect was typically seen in holograms recorded with 8 s exposure times, independent of whether the nanowire was field emitting or not. Related discussions are presented in the literature [46, 48].

One example where a double-exposure effect was seen is shown in Fig. 6.6. For this measurement, the nanowire was electrically biased at 171 V and the field emission current was approximately 100 nA. Moiré-like fringes are visible in the hologram (Figs. 6.6a-b) and in the reconstructed phase contour map (Fig. 6.6c) and amplitude image (Fig. 6.6d). This double-exposure effect results from the electrostatic potential or charge density varying during the exposure time [120]. Detailed interpretations of double-exposure holograms are presented in the literature [121].

The measured current started to drop at an applied voltage of 180 V and decreased to zero at 188 V. This drop may have resulted from the distance between the nanowire and the counter-electrode increasing as a result of a combination of the electrical force acting on the nanowire, the instability of the movable hat, changes to the surface of the nanowire, the field emitted electrons creating ions at the counter-electrode that are attracted by the nanowire, or the nanowire becoming shorter due to the field emission or heating current. The inset to Fig. 6.5 shows a corresponding *F-N* plot. It should be noted that the validity of the *F-N* theory for nanostructures is still under debate [45]. In the region between 148 and 180 V, the plot shows a linear relationship between $\ln \frac{I}{V^2}$ and $\frac{1}{V}$, which can be interpreted using the expression

$$\ln \frac{I}{V^2} = -1842.73 \frac{1}{V} - 17.46. \tag{6.1}$$

The slope of the *F-N* plot is linked directly to the field enhancement factor and the work function [122, 123], according to the relation

$$1842.73 = \frac{B\phi^{1.5} d_{capacitor}}{\gamma}, \tag{6.2}$$

where B is a constant, which takes a value of 6.83×10^9 V$\cdot$ eV$^{-1.5}\cdot$m^{-1}, ϕ is the work function of the W_5O_{14} nanowire, $d_{capacitor}$ is the distance between the electrodes, *i.e.*, the counter-electrode and the μm-sized W wire where the nanowire was attached, and γ is the field enhancement factor. The work function is reported to take a value of 4.3 eV [116]. The distance $d_{capacitor}$ was measured to be 10.5 μm (Fig. 6.2). The field enhancement factor could then be estimated to be approximately 350. On the assumption that the onset voltage for field emission was 148 V, the local electric field as a result of field enhancement from the nanowire was calculated to be $E_{loc} = \gamma \frac{V}{d_{capacitor}} = 4.90$ V/nm.

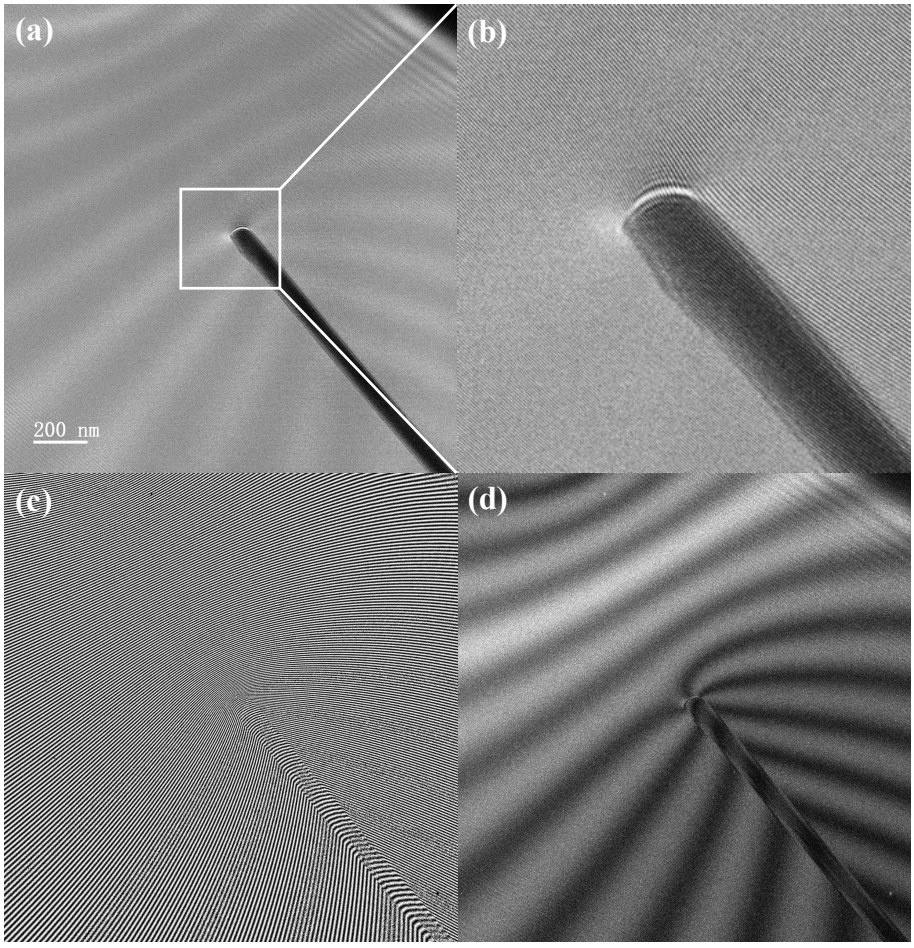

Fig. 6.6 Example of a double-exposure effect. (a) Off-axis electron hologram and (b) magnified region around the apex. (c) Phase contour map and (d) amplitude image reconstructed from the hologram shown in (a). The W_5O_{14} nanowire was electrically biased at 171 V and the measured field emission current was approximately 100 nA. The phase contour spacing is 2π radians. See text for details.

6.3 Model-independent reconstruction of charge density

A series of off-axis holograms was recorded with the W_5O_{14} nanowire electrically biased at between 130 and 188 V. *I-V* measurements were not performed at the same time as hologram acquisition. The phase was reconstructed from each hologram in order to calculate cumulative charge profiles. When the nanowire was biased at 188 V, the phase jump between adjacent pixels exceeded 2π and phase information could not be retrieved reliably.

6.3.1 Mean inner potential contribution to the phase

As a result of the fact that a strong electrostatic force acted on the nanowire when it was subjected to a high electrical bias, it was observed to bend. The alignment of phase images to calculate differences between results recorded at different applied bias voltages, in order to subtract the MIP contribution to the phase, was then difficult or impossible. Therefore, the analyses presented in the following section were performed without subtracting the MIP contribution to the phase, resulting in the possibility of artefacts in subsequent charge density measurements [102]. The influence of the MIP contribution to the phase on charge density measurements is considered below.

Fig. 6.7a shows a phase image recorded in the absence of an applied bias voltage, *i.e.*, comprising only the MIP contribution. Such an image is directly proportional to the projected thickness of the nanowire (in the absence of dynamical diffraction). It can be used to determine the influence of the MIP contribution to the phase on the calculated charge density. A line profile extracted from the phase image across the nanowire axis (marked by a magenta line in Fig. 6.7a) suggests that it has a quasi-rectangular cross-section (Fig. 6.7c, magenta). A second line profile extracted along the nanowire axis (marked by a green line in Fig. 6.7a) indicates that the nanowire has a sharply-terminated thickness profile at its apex (Fig. 6.7c, green), with a transition distance that is not greater than 15 nm, including the 10-nm-thick amorphous layer. The flatness of the phase in the vacuum region in both phase profiles confirms that the unbiased nanowire is not significantly charged electrically in the presence of the high-energy electron beam.

Additional contributions to the charge density arising solely from the MIP contribution to the phase can result from gradients in phase at the edge of the object, where its projected thickness is changing. Such "artificial" or effective charges are visible in Figs. 6.7d-e, which show cumulative charge profiles integrated along the dashed rectangle marked in Fig. 6.7a from the base to the apex (red arrow) and from one edge to the other (blue arrow), respectively. The *total* effective charge associated with the MIP contribution to the phase is zero in both cases. Therefore, measurements of the *total* charge are likely to be free of artefacts, even in

the presence of the MIP contribution to the phase. For integration along the nanowire axis, as indicated by the red arrow in Fig. 6.7a and by Fig. 6.7d, the cumulative charge is always zero except when the integration region approaches the apex of the nanowire. The fact that the cumulative charge profile is negative and then returns to zero is consistent with the Laplacian of the MIP contribution to the phase shown in Fig. 6.7b. As the "artificial" charges due to the MIP contribution to the phase are present in a narrow (15 nm) region at the apex of the nanowire, this region is excluded from the analysis (*i.e.*, the fitting of the profiles) presented in the following section.

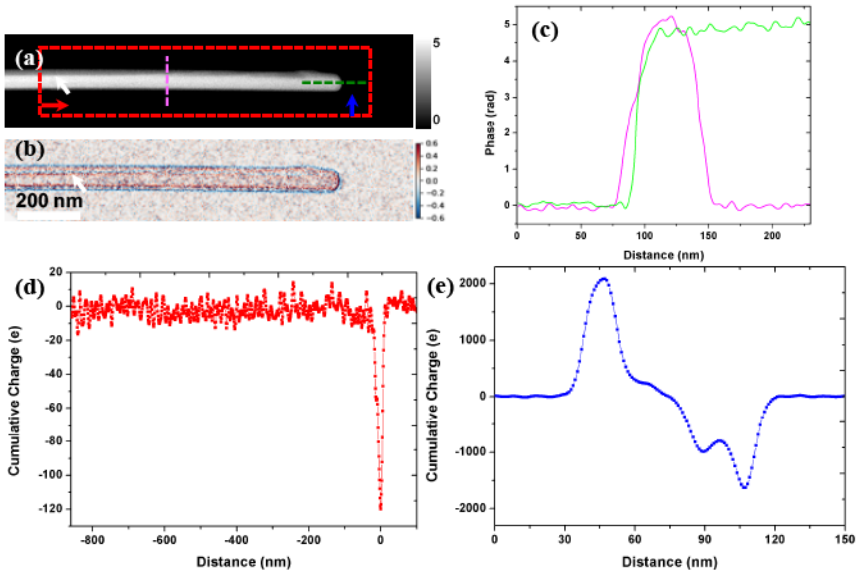

Fig. 6.7 MIP contribution to the phase alone and its effect on the measurement of cumulative charge profiles: (a) Phase image recorded without an applied electrical bias, *i.e.*, corresponding to the MIP contribution only. (b) Effective charge density calculated from the Laplacian of (a) using Eq. 2.7. (c) Phase profiles extracted from (a) along the nanowire axis (green) and across the nanowire axis (magenta). (d) and (e) Cumulative charge profiles measured from (b) along the nanowire axis and across the nanowire axis, respectively, from the region marked by a red dashed rectangle in (a). The integration region was allowed to shrink in the direction of the red/blue arrow to create the line profiles shown in (d) and (e), respectively.

6.3.2 Cumulative charge profiles

Since the net contribution to the cumulative charge from the MIP contribution to the phase is zero (although there are jumps in the cumulative charge profiles at the very edge

and apex of the nanowire), the cumulative charge in the presence of an applied bias can be calculated using total phase images (*i.e.*, without removing the MIP contribution) by using Eq. 2.9 directly.

Fig. 6.8 shows cumulative charge profiles for voltages up to 186 V. The integration region (marked by a red rectangle in the top panel of Fig. 6.8) is similar to that labelled by a red rectangle in Fig. 6.7a. In order to obtain the cumulative charge at every position x, the integration region was allowed to shrink progressively in the direction indicated by a red arrow.

The total charge in the selected region (the red rectangle marked in Fig. 6.8), *i.e.*, the value at $x = 0$ nm in the chosen reference system, increases linearly with applied bias voltage, as shown in the inset to Fig. 6.8. This measurement allows the capacitance of this part of the nanowire to be determined to be 8.78 ± 0.04 aF.

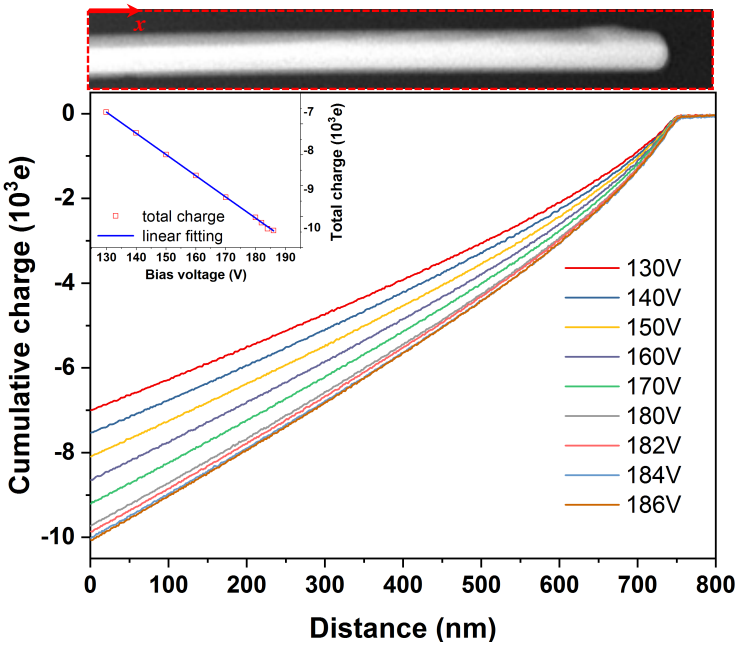

Fig. 6.8 Cumulative charge profiles along the W_5O_{14} nanowire measured from electron optical phase images for applied bias voltages of 130 to 186 V. The upper panel shows the MIP contribution to the phase (recorded in the absence of an applied electrical bias), with the integration region marked. The x axis points to the right. The origin is chosen to be at the left edge of the image. The inset shows the total charge in the chosen region of the nanowire plotted as a function of applied bias voltage (red squares) and a linear fit to these values (blue line).

The fact that the cumulative charge changes in a quasi-parabolic manner as the width of the integration region decreases suggests that the charge density along the nanowire is approximately linear. However, in Fig. 6.9, a quadratic (2^{nd} order polynomial) fit to the cumulative charge profile for an applied electrical bias voltage of 150 V was determined from values measured more than 200 nm from the apex of the nanowire. This result shows that the experimental cumulative charge profile (black) deviates significantly from the parabolic trend (blue) at a distance of approximately 200 nm from the apex of the nanowire and that there is an accumulation of charge at the apex of the nanowire in the presence of an applied electrical bias.

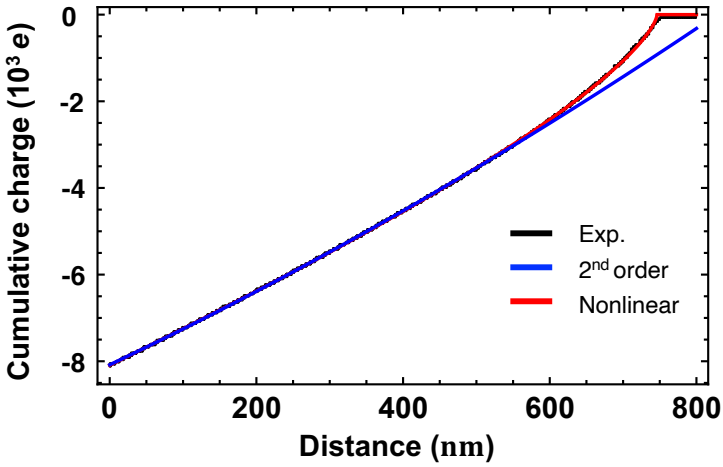

Fig. 6.9 Fitting of cumulative charge profile based on line charge models. Comparison between experimentally-measured cumulative charge profile (black) and best fits based on a nonlinear line charge model described by Eq. 6.3 (red) and a 2^{nd} order polynomial fit (blue). The nanowire was electrically biased at 150 V.

As a result of accumulation of charge at the apex of the nanowire, 2^{nd} order polynomial fitting to the experimental cumulative charge profiles was performed separately for the region far from the apex and for the region close to the apex of the nanowire, as shown in Fig. 6.10. The nanowire was electrically biased at 150 V. The fitting confirms that the line charge densities in the two regions are significantly different. The corresponding line charge density at each applied bias voltage can be derived directly from the derivative of the fitted 2^{nd} order polynomial, as shown in Fig. 6.11.

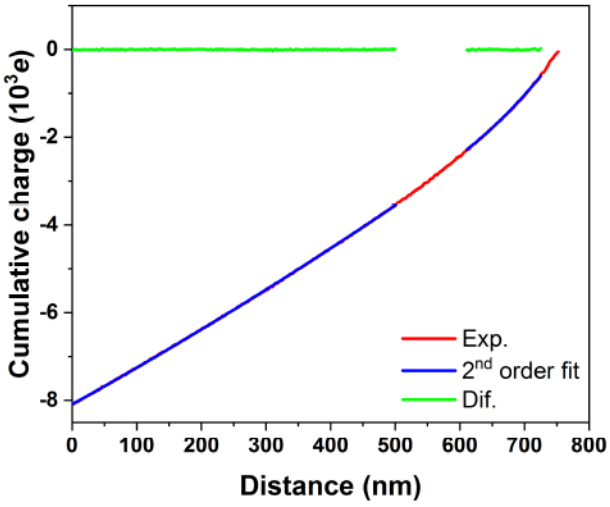

Fig. 6.10 Comparison between experimental cumulative charge profile (red) and fitted profiles (blue) to regions far from the apex and close to the apex separately based on 2^{nd} order polynomial fits. The difference between the two profiles is shown in green. The nanowire was electrically biased at 150 V.

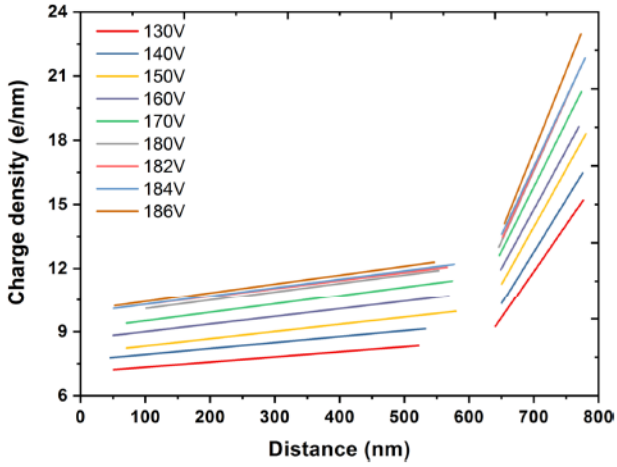

Fig. 6.11 Derived line charge density profiles with the W_5O_{14} nanowire biased at different voltages from 130 to 186 V, obtained from 2^{nd} order polynomial fits to the experimental cumulative charge profiles. See text for details.

Fig. 6.12 shows the slopes and intercepts of the fitted line charge densities plotted as a function of applied bias voltage. The slopes and intercepts in both the region close to the apex and the region far from the apex increase almost linearly with applied bias voltage up to the onset of field emission. The slope can be interpreted as a changing rate in the line charge density along the length of the nanowire, while the intercept can be interpreted as the line charge density at the apex of the nanowire; on the assumption that the effect of the MIP contribution to the phase and under sampling can be neglected. Close to the apex (red), the slopes are one order of magnitude higher than those far from the apex (blue), *i.e.*, the increasing rate in the line charge density far from the apex is on the order of 10^{-3} e/nm^2, while that close to the apex is on the order of 10^{-2} e/nm^2. When the nanowire arrived at 180, 182 and 184 V, the slope of the line charge density stabilised at approximately $6.55 \times 10^{-2} e$/nm^2 in the region close to its apex, while the slope of the line charge density started to increase again at a bias voltage of 186 V. In Fig. 6.12b, the line charge density at the apex (red squares) continues to increase from 16.23 e/nm at 130 V to 21.86 e/nm at 170 V and then remains constant at 23.22 e/nm when it reaches a stable state at bias voltages of 180, 182 and 184 V. After a slight increase to 186 V, the line charge density increases to 24.50 e/nm. The fact that both the slopes and the intercept at bias voltages of 180, 182 and 184 V remain unchanged suggests that the nanowire reaches a field emission state.

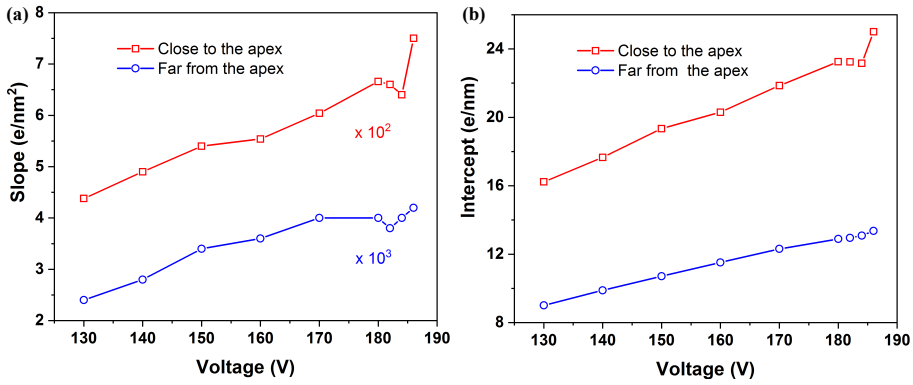

Fig. 6.12 (a) Slopes and (b) intercepts of derived line charge densities, with the nanowire electrically biased at different voltages. (See Fig. 6.11.) For convenience, the slopes are multiplied by 10^2 and 10^3 in the regions close to and far from the apex, respectively. See text for details.

6.4 Analytical model-dependent measurement of charge density

In previous experimental studies of electrically-biased carbon nanotubes [74] and sharp metallic needles [72, 124], it was shown that a linear or constant charge density distribution is associated with a tip shape, whose equipotential surface is similar to that of a paraboloid or an ellipsoid of rotation. Such shapes are markedly different from that of the present nanowire, which can be described more closely as a cylinder on the assumption of rotational symmetry.

A similar accumulation of charge to that observed here has been discussed in a series of didactic papers about the equilibrium charge distribution along a conducting needle [125–127]. These works highlight the influence of the detailed shape of the needle on the charge distribution along it. Starting from these different numerical [125] and analytical [126, 127] studies, we focus here on adapting the discrete model of Griffiths and Li [125] for a single needle to the more complex configuration of the present setup. Our starting point is to consider three aligned line charges that have different constant charge densities and lengths and to adjust their parameters to describe the fixed side of the specimen holder, the attached nanowire and the counter-electrode. The shape of the nanowire near the tip then resembles that of very elongated ellipsoid. (See Appendix C for further details).

In order to obtain a better approximation to the cylindrical shape of the nanowire, the line charge that was used to model it was substituted by N discrete equidistant point charges. By varying the magnitudes of these charges and imposing the condition that the potential between them must be constant [128], it is possible to obtain a better approximation to the shape of a real specimen. When $N = 601$ charges were used, the cumulative charge up to a distance of 700 nm from the apex of the nanowire was found to exhibit a similar behaviour to that of the experimental cumulative charge profile. (See Appendix C Fig. C.4). The observation of charge accumulation at the apex was well reproduced, apart from a difference between the experimental and theoretical charge at the very apex (737 *vs* 400 electrons, respectively), which may be attributed to the fact that the model does not fully represent the shape (square *vs* circular cross-section) and sharpness of the apex of the nanowire.

6.4.1 Nonlinear line charge density

An advantage of using the approach of Griffiths and Li [125] is that, inspired by the treatment of a finite cylinder by Smythe [129], they proposed an empirical analytical expression for the charge density in a needle. Based on their work and by limiting the present considerations to the tip of the nanowire, the line charge density λ in the present nanowire is

assumed to take approximately the following form, which comprises a constant term C, a linear term Dx and a divergent term $\frac{B}{(A-x)^{1/3}}$ that corresponds to the "fundamental term" in Smythe's expansion [129]:

$$\lambda(x) = C + Dx + \frac{B}{(A-x)^{1/3}}, \tag{6.3}$$

where A, B, C and D are fitting parameters. The cumulative charge can then be calculated by integrating the line charge density along the length of the nanowire. (See Appendix C for further details.) Eq. 6.3 fits the present experimental measurements well, as shown in Fig. 6.9 for an applied bias voltage of 150 V. (See Appendix C Fig. C.5 and Table C.2 for further details of the fits to all of the experimental measurements.) The corresponding line charge density along the nanowire, which can be plotted by using the best-fitting parameters, as shown in Fig. 6.13, reveals the divergence of the charge density at its apex.

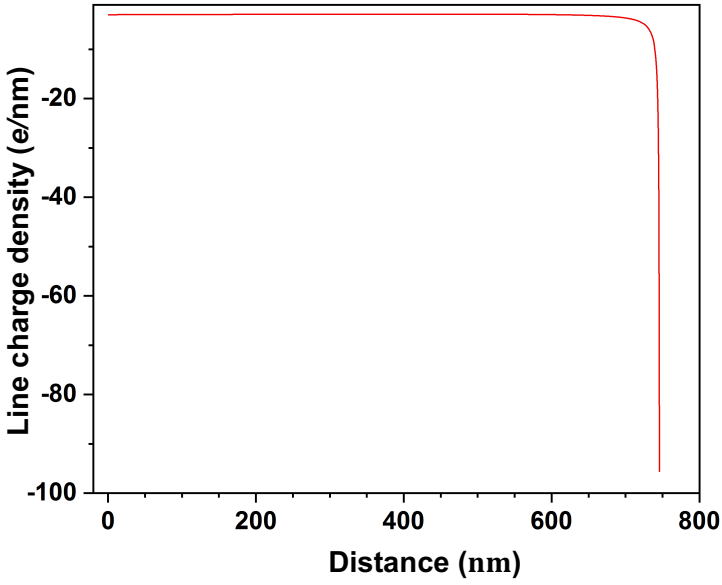

Fig. 6.13 Line charge density along the nanowire obtained from the best-fitting parameters based on Eq. 6.3. The nanowire was electrically biased at 150 V.

Although the close fit provides strong evidence for the validity of Eq. 6.3, it is not possible to provide values of the fitting parameters for the full length of the nanowire due to the limited field of view in the recorded holograms. In order to infer this information from the present measurements and to assess the relative weights of the linear and additional contributions

to the field enhancement factor, the standard geometry of a line charge distribution that protrudes perpendicular to a conducting plane in the presence of an electric field that is asymptotically uniform and parallel to the direction of the line charge is assumed here [130, 93, 131]. For a *linear* charge distribution, the surface that corresponds to $V = 0$ has the shape of a hemi-ellipsoid and is suitable for representing the surface of a field emitter that has such a shape. A similar procedure was used here to assess the effect on the field enhancement factor of adding a nonlinear term (*i.e.*, the divergence term in Eq. 6.3) to a linear charge distribution. Satisfyingly, the additional nonlinear term changes the shape of the equipotential surface from an elongated ellipsoid to a rounded cylinder. (See Appendix C for further details.)

6.4.2 Field enhancement factor and emission current

It is assumed that the length of the line charge is equal to that of the nanowire (*i.e.*, $A = 9.4\ \mu$m) and that the charge density vanishes at the conducting plane (*i.e.*, $\lambda(0) = 0$). The remaining parameters are expressed in terms of the total charge in the linear contribution, q_{lin}, as well as the additional (*i.e.*, nonlinear) term, q_{tip}. The expression for the line charge density in Eq. 6.3 becomes

$$\lambda(x) = -2\frac{q_{tip}}{A} + 2\frac{q_{tip}}{A^{2/3}(A-x)^{1/3}} + 2q_{lin}\frac{x}{A^2}. \tag{6.4}$$

The electrostatic potential and electric field can then be calculated based on image charge theory. (See Appendix C for further details.) Here, the radius of the nanowire at its base is fixed to (in this case, 40 nm), *i.e.*, the aspect ratio of the nanowire is kept constant. The ratio between the linear and nonlinear terms is then considered as a free parameter (taking $q_{lin} = 1$), which affects the overall shape of the nanowire. A knowledge of the electric field at any position on the surface of the nanowire allows us to calculate the field enhancement factor to be calculated, as well as, upon further integration, the emission current from the Fowler-Nordheim expression. (See Appendix C for further details.)

The results are shown in Figs. 6.14a-c, in the form of two-dimensional maps of the magnitude of the electric field for ratios between the linear and nonlinear terms of 4, 5 and 6, respectively. In each case, the black area represents the shape of the tip. The maximum value at the apex gives the field enhancement factor, as shown in Figs. 6.14d-f, which illustrate the trend of the electric field along the axis from the apex. The field enhancement factor is approximately 340 when the ratio is 5, which is close to the experimental estimate of $\sim$350. It should be noted that the latter value, which is derived from the fit to the F-N plot, is an average over the entire surface of the nanowire where field emission happened. Figs. 6.14g-i

show the calculated emission current plotted as a function of the applied bias voltage for the above ratios. (See Appendix C for details about the field emission calculations.) Despite the use of several assumptions and the relative simplicity of the model, it is encouraging that the result for a ratio of 5 is in good agreement with the present experimental measurements (Fig. 6.5).

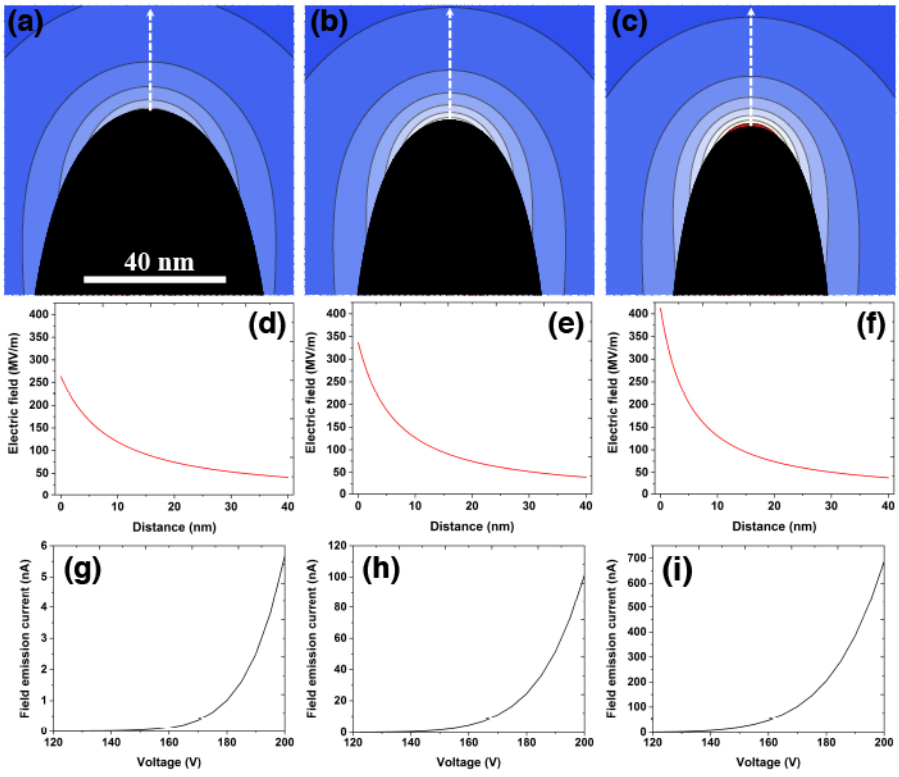

Fig. 6.14 Simulations based on a nonlinear charge density model: (a)-(c) Electric field maps in a central slice. The contour spacing is 50 V/μm. The black shadow marks the apex of the nanowire. (The rest of the nanowire is not shown); (d)-(f) Field enhancement factors along the axis of the nanowire (indicated by white arrows in (a)-(c)); (g)-(i) Field emission current for ratios between the linear and nonlinear contributions of 4, 5 and 6, respectively. A ratio of 5 delivers the most satisfying agreement with the experiments.

6.5 Model-based iterative reconstruction of charge density

In addition to the model-independent (Section 6.3) and model-dependent (Section 6.4) measurements of charge density, the MBIR approach developed in Chapter 5 can also be used to reconstruct the charge density in the W_5O_{14} nanowire. It should be noted that, as a result of the instability in its field emission behaviour, only a single hologram of the nanowire was recorded at each applied bias voltage, preventing 3D mapping of the charge density inside it during field emission. Nevertheless, the projected charge density can still be retrieved.

A single phase image recorded with the nanowire electrically biased at 184 V was used for reconstruction of the charge density using the MBIR approach. Since the MIP contribution to the phase was significantly lower than that results from the applied bias voltage, the phase inside the specimen was also used for reconstruction. An 8-pixel-wide buffer layer was set outside each border to taken into account the PRW effect and the presence of charges outside the FOV. The regularisation parameter was set to 500. The sampling density is 2.86 nm.

Fig. 6.15 shows the reconstructed projected charge density, which reveals charge accumulation at the apex and the edges of the nanowire. The presence of charges at the bottom the nanowire (at the left border) is thought to result from the fact that the presence of charges outside the FOV is not fully compensated by the 8-pixel-wide buffer region.

Two line profiles of the reconstructed charge density confirm the presenec of charge accumulation at the apex and edges of the nanowire, as shown in Figs. 6.16a-b. The projected charge density along the length of the nanowire (Fig. 6.16a, marked by a red arrow in Fig. 6.15) increases rapidly at a distance of approximately 100 nm from the apex to a maximum of approximately 1.5 e/nm^2 at the apex of the nanowire. The projected charge density plotted across the width of the nanowire (Fig. 6.16b, marked by a blue arrow in Fig. 6.15) shows a maximum of approximately 0.6 e/nm^2 at the edges and a minimum of 0.3 e/nm^2 at the centre of the nanowire. For comparison with the line charge density, the reconstructed projected charge density (Fig. 6.15) was integrated along the width of the nanowire to obtain the line charge density along its length, as shown in Fig. 6.16c. The charge profile increases first slowly and then more rapidly, in a manner that is consistent with the discussion presented in Section 6.3.2. Linear fits to the two separate regions allow the line charge density to be expressed by the slope and intercept: (-5.20 $\times 10^{-3}$, -13.50) in the region far from the apex and (-1.85 $\times 10^{-1}$, -30.24) in the region close to the apex. In the region far from the apex, the MBIR-derived line charge density is almost consistent with that derived from 2^{nd} order fitting (see Fig. 6.12, (-4.00 $\times 10^{-3}$, -13.10). In the region close to the apex, the greater slope (-1.85×10^{-1}) in the reconstructed line charge density is approximately twice as large as that obtained from the fit to the experimental cumulative charge profile (6.40×10^{-2}). The line charge density at the apex of the nanowire also deviates by approximately 30% (-23.16

vs -30.24). The cumulative charge profile from the reconstruction, which is shown in Fig. 6.16d, is in agreement with that obtained from experimental data except in the region close to the left border of the image. This difference is probably a result of the presence of charges outside the FOV (in the bottom of the nanowire).

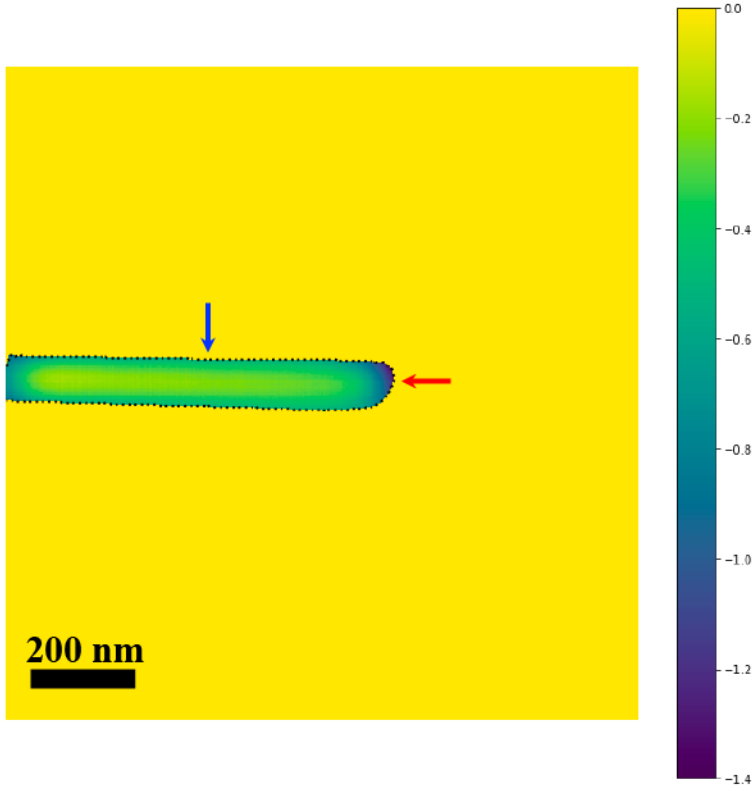

Fig. 6.15 Model-based iterative reconstruction of the projected charge density with the W_5O_{14} nanowire electrically biased at 184 V, shown in units of e/nm^2. The phase across the entire FOV was used for reconstruction without the MIP contribution removed. An 8-pixel-wide buffer layer was set outside each border to taken into account the PRW effect and the presence of charges outside the FOV. The regularisation parameter was set to 500. The sampling density is 2.86 nm.

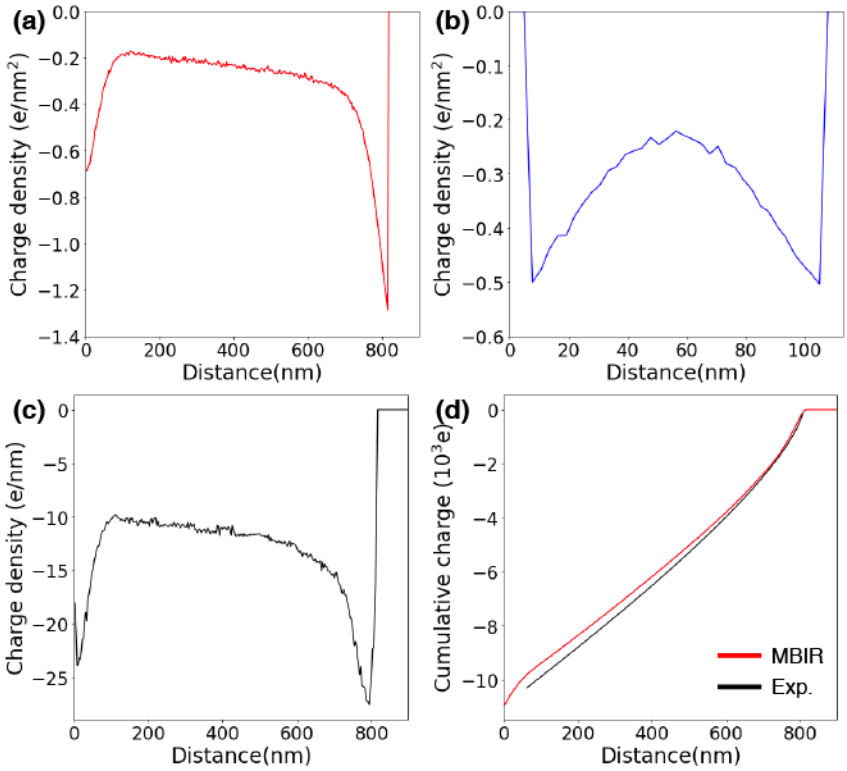

Fig. 6.16 Line profiles of the projected charge density shown in Fig. 6.15. (a, b) Line profile of the reconstructed charge density along the length of the nanowire (marked by a red arrow in Fig. 6.15) and along its width (marked by a blue arrow in Fig. 6.15), respectively. (c) Line charge density along the length of the nanowire. (d) Cumulative charge profiles from MBIR reconstruction (red line) and using the Laplacian approach (black line) along the nanowire axis.

There are several possible explanations for this discrepancy, including: 1) the smoothing effect of the regularisator (see Section 5.3), which can suppress noise in the reconstructed solution by increasing the regularisation parameter, aiming to pick a solution with a smaller Euclidean norm; 2) the fact that the MIP contribution to the phase was not removed, which results in uncertainty in the uniqueness of the reconstruction (see Section 5.6.1); 3) the combined effect of under sampling and charge accumulation at the apex of the nanowire, which may result in a Gaussian smoothing effect; 4) the accuracy of the selection of the mask to determine where charges can be located, in particular in the region close to the apex of the nanowire (see Section 5.4.1); 5) from the rounding of the apex of the nanowire.

The projected in-plane electric field was calculated from the gradient of the phase after removing the PRW effect (see Section 5.4.5), as shown in Fig. 6.17. The projected in-plane electric field is nearly symmetrical with respect to the nanowire axis, is localized at the apex region and decreases rapidly with distance from the apex of the nanowire. The maximum projected in-plane electric field strength is approximately 1.4 V/nm.m.

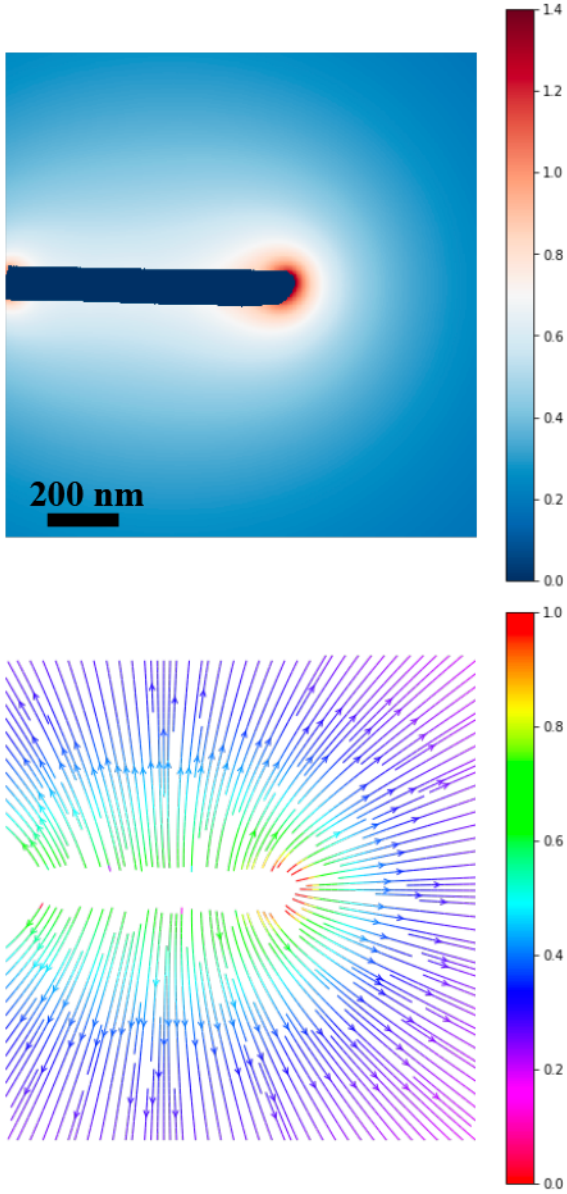

Fig. 6.17 Projected in-plane electric field inferred from the reconstructed projected charge density obtained using MBIR. Top: Strength of the projected in-plane electric field, shown in V/nm.m. Bottom: Streamline plot of the projected electric field. The shadow of the nanowire is marked in blue (top) or in white (bottom).

6.6 Discussion

6.6.1 Model-independent, model-dependent and model-based iterative reconstruction

Both the model-dependent approach (Section 6.4) and the model-based iterative reconstruction approach (Section 6.5) confirm the presence of charge accumulation in the nanowire that was measured using the model-independent approach (Section 6.3).

In the model-dependent approach (Section 6.4 and Appendix C), a three-line-charge model was used to represent the three components in the experimental setup (*i.e.*, the support to which the nanowire was attached, the nanowire and the counter-electrode). By making use of several assumptions (*e.g.*, the fact that an equipotential surface should resemble the shape of the electrode), the model is shown to predict a similar charge distribution to that obtained using the model-independent approach (see Appendix C Fig. C.4). A discrepancy results from the fact that the model is not accurate enough to describe the true shape of the setup, including the assumption of cylindrical symmetry to describe the quasi-rectangular cross-section of the nanowire. This shortcoming of the model-dependent approach results from the fact that the exact geometrical setup describing the experiment has to be reproduced in the model. In addition, the model and the associated boundary conditions need to be treated analytically or numerically. Based on the model-independent measured cumulative charge profiles (Section 6.3.2), an empirical expression for the line charge density along the nanowire was obtained, offering an alternative way for interpreting of measured field emission data based on several assumptions (Sections 6.4.1 and 6.4.2).

The model-based iterative reconstruction approach (Section 6.5) also reproduces the results obtained using the model-independent approach (Section 6.3), providing good agreement to the cumulative charge profile (Fig. 6.16d) and the charge density profile along the length of the nanowire (Fig. 6.16c). It also allows the projected charge density of the nanowire to be reconstructed with reduced noise, confirming the accumulation of charge at the apex and at the edges of the nanowire (Fig. 6.15). This consistency relies on an accurate specification of the mask that defines where charges can be located, the use of boundary buffer pixels to take into account the presence of charges outside the field of view and the perturbed reference wave effect, the choice of a suitable regularisation strength, subtraction of the mean inner potential contribution to the phase image and an assessment of the uniqueness of the reconstruction. It should be noted that there is a slight discrepancy in the line charge density at the apex of the nanowire obtained using the model-independent and model-based iterative reconstruction approaches. This discrepancy may result from the sampling density

or spatial resolution used in the reconstruction, or from the smoothing effect associated with the choice of regularisation strength in the model-based iterative reconstruction approach.

In the model-independent approach (Section 6.3), the MIP contribution to the phase can result in the appearance of artificial charges where the specimen thickness changes. (See Section 6.3.1.) In the model-dependent approach, the shape of the specimen is used to define the equipotential surface. When using the model-based iterative reconstruction approach, the presence of the MIP contribution to the phase can affect the uniqueness of the reconstruction. (See Section 5.6.1.) For the reconstruction of charge density in the nanowire described in Section 6.5, the phase across the entire field of view was used without removing the MIP contribution to the phase, as it was significantly smaller than that from the applied bias voltage. For comparison, a reconstruction was performed without using the phase inside the nanowire, as shown in Fig. 6.18, showing no localisation of charge at the edges of the nanowire. This is different from the result obtained for reconstruction with the phase inside the specimen used (Fig. 6.15 and Fig. 5.14b in the LaB_6 field emitter). Such a localisation of charge is expected based on classical electrostatics, highlighting the fact that access to the phase inside the specimen is important for accurate reconstruction of the charge density inside the specimen.

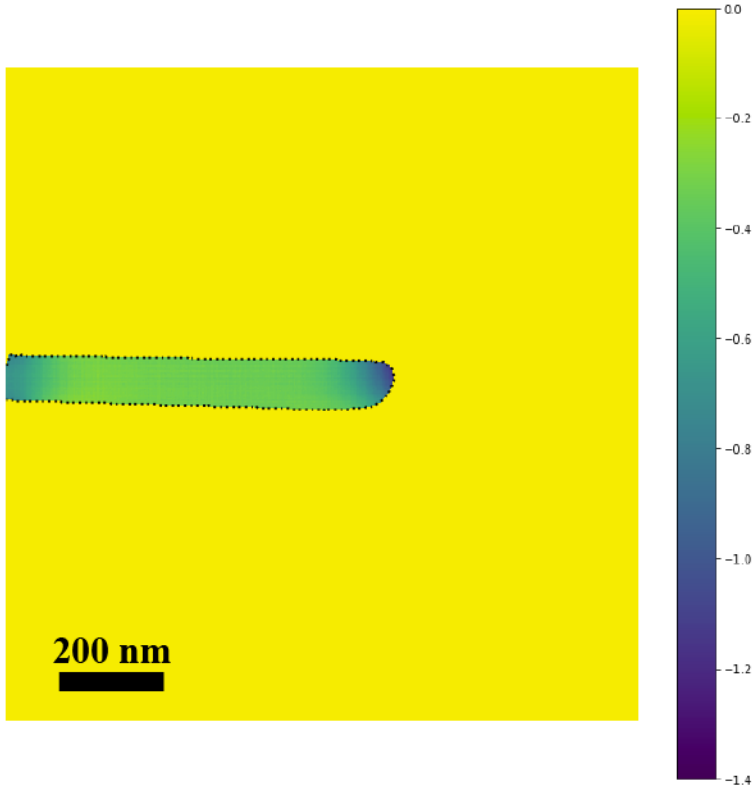

Fig. 6.18 Model-based iterative reconstruction of the projected charge density with the W_5O_{14} nanowire electrically biased at 184 V, shown in units of e/nm^2. The phase inside the nanowire was not used for reconstruction. The reconstruction parameters were the same as those shown in Fig. 6.15

6.6.2 Comparison with results from a CdS nanocomb

The slope of the charge density profile along the length of the W_5O_{14} nanowire is not constant and the profile has two distinct regions: a linearly-decreasing charge density far from the apex and charge accumulation close to the apex. This behaviour is different from that expected for a line charge model that is based on a constant charge density [71] or a linear charge density [72, 73]. Constant and linear charge density profiles are typically associated with equipotential surfaces that resemble ellipsoids [93, 72]. For the W_5O_{14} nanowire, which has a quasi-rectangular cross-section and a sharply-terminated apex, such a line charge model is therefore not valid.

In order to confirm the influence of geometry on charge density, a CdS nanocomb, which also has a quasi-rectangular cross-section and a sharply-terminated apex, was studied. A CdS nanocomb was electrically biased in the same experimental setup. The distance between the counter-electrode and the nanocomb was set to 3 μm. Fig. 6.19a shows the MIP contribution to the phase recorded using off-axis electron holography. The diameter of the CdS nanocomb is approximately 140 nm. Fig. 6.19b shows two representative phase profiles extracted parallel and perpendicular to the axis of the comb axis along the lines marked in Fig. 6.19a. The phase profile parallel to the axis of the comb (green) jumps abruptly from vacuum to the nanocomb, implying that the apex is sharply terminated. The phase profile perpendicular to the axis of the comb (magenta) is similar to that expected for a quasi-rectangular cross-section, with the edges rounded either due to the synthesis procedure or due to surface contamination.

Three phase images were recorded with the nanocomb biased at voltages of 120, 130 and 140 V and used to calculate cumulative charge profiles (using Eq. 2.9) and line charge density profiles (as described in Section 6.3.2). Fig. 6.19c shows the resulting cumulative charge profiles and corresponding line charge density profiles (inset). The CdS nanocomb behaves similarly to the W_5O_{14} nanowire. It can be concluded that its geometry, in particular its prismatic cross-section and the termination of its apex, plays a crucial role in determining the charge density along its length.

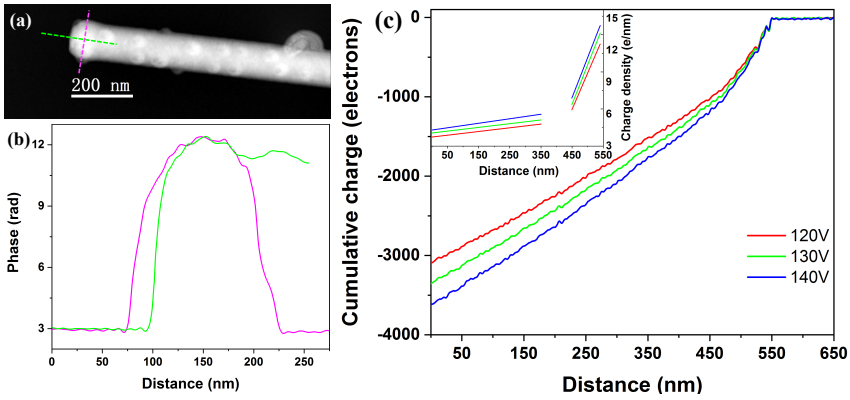

Fig. 6.19 Charge density measurement in a CdS nanocomb in the presence of applied electrical bias. (a) Phase image recorded without an applied bias voltage. (b) Two representative phase profiles extracted parallel (green) and perpendicular (magenta) to the comb axis along the marked dashed lines in (a). (c) Cumulative charge profiles and (inset) corresponding line charge density profiles along the axis of the CdS nanocomb for different applied bias voltages of 120 V (red), 130 V (green) and 140 V (blue). See text for details.

6.7 Summary and conclusions

This chapter contains measurements of charge density along a W_5O_{14} nanowire, which has a sharply-terminated apex and a quasi-rectangular cross-section, both before and during field emission, in an electrical biasing setup in the TEM. The model-independent, model-dependent and model-based iterative reconstruction approaches are used for the reconstruction of charge density along the nanowire. Their advantages and disadvantages are compared. The combined use of the three approaches helps to obtain a more reliable interpretation of the experimental data. Charge is observed to accumulate at the apex of the nanowire, while the charge profile far from the apex of the nanowire can be described using a linear approximation. Similar charge accumulation is observed at the apex of a CdS nanocomb, which also has a sharply-terminated apex and a quasi-rectangular cross-section.

Chapter 7

Charge density measurement in a carbon fibre needle

In order to demonstrate the ability to measure 3D charge, electric field and electrostatic potential distributions using the MBIR algorithm, an electrically-biased needle-shaped carbon fibre specimen is studied in this chapter. An advantage of examining a carbon fibre is that carbon is a light element that scatters electrons weakly. In addition, a carbon fibre is not fully crystallised and only has a highly-textured structure along the fibre axis. These two reasons reduce the presence of diffraction contrast when recording a tomographic tilt series of off-axis electron holograms, which is required for retrieval of the desired 3D information.

7.1 Electrical biasing setup

The carbon fibre needle was prepared using a standard FIB preparation procedure. Fig. 7.1a shows a low-magnification bright-field TEM image of the experimental setup of the needle and a μm-sized Au tip, which serves as a counter-electrode. The diameter of the apex of the needle is approximately 60 nm (see the higher-magnification image in Fig. 7.1b) and the length of the needle is approximately 2.5 μm. The distance between the counter-electrode and the needle is approximately 4.5 μm.

Off-axis electron holograms were recorded using exposure times of 6 s with a direct electron counting Gatan K2-IS camera. The voltage of the electrostatic biprism was set to 150 V. The holographic interference fringe spacing was approximately 1.7 nm and the inference width was approximately 1.8 μm. 30 holograms were recorded for each tilt angle to increase the signal-to-noise ratio.

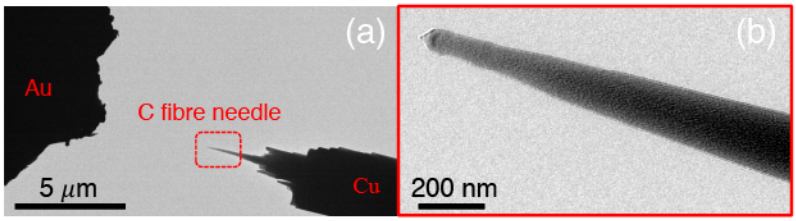

Fig. 7.1 Experimental setup for electrical biasing of a carbon fibre needle. (a) Low-magnification bright-field TEM image showing the experimental setup for electrical biasing of a carbon fibre needle. (b) Higher-magnification image of the carbon fibre needle.

Fig. 7.2a shows the MIP contribution to the phase of the needle with no applied bias voltage and a corresponding phase contour map. The flatness in the vacuum region indicates that electron-beam-induced charging of the needle is negligible. Fig. 7.2b shows a phase image recorded with the needle biased at +40 V and a corresponding phase contour map. The asymmetry of the images results from the PRW effect. Fig. 7.2c shows the difference between the phase images (shown in Figs. 7.2a-b) after alignment and a corresponding phase contour map. The difference image therefore represents the contribution from electrical biasing alone.

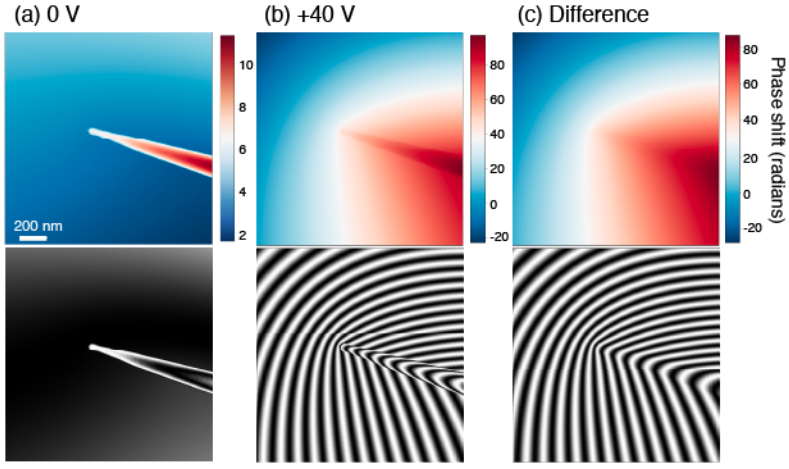

Fig. 7.2 Phase images (top) and corresponding phase contour maps (bottom) recorded with the needle biased at 0 and +40 V and their difference. (a) The MIP contribution to the phase (0 V). (b) Phase including contributions from the MIP and the applied electrical bias at +40 V. (c) Difference between (a) and (b) after alignment. The tilt angle is 0°. The phase contour spacing is 2π radians.

7.2 3D reconstruction of charge, electric field and electrostatic potential

A single phase image recorded in projection can convey information about the 3D electrostatic potential within and around the specimen projected along the electron beam direction. In some cases, an assumption of (rotational) symmetry of the specimen allows the 3D electrostatic potential to be retrieved from a single image (*e.g.*, [132, 133]). Nevertheless, 3D information should in general be obtained from tilt series of images, as a perfectly symmetrical object hardly exists in practice.

7.2.1 3D data acquisition

Two tomographic tilt series of holographic phase images were recorded. One series was recorded without an electrical bias applied to the needle. This dataset therefore only includes the MIP contribution to the phase. It can be used both to remove the MIP contribution to the phase from a dataset with the needle electrically biased (see Fig. 7.2) and to reconstruct the 3D shape of the needle. A second dataset was recorded with +40 V applied to the needle. Tomographic data were recorded over a tilt range of -52° to $+48^\circ$ with a tilt increment of 4°. Fig. 7.3 shows a schematic representation of the acquisition of a holographic tomography dataset with the needle electrically biased at +40 V. Each sub-image shows a phase contour map generated after removing the MIP contribution to the phase at each individual specimen tilt angle.

7.2.2 3D mask

The successful application of the MBIR approach to reconstruct a 3D charge density requires the use of a 3D mask to define where the charge can be located. (See Chapter 5.) Since charge can only be located inside the needle, its outer surface can serve as a 3D mask. Such a mask can be obtained from the MIP contribution to the phase. Here, the tomographic reconstruction of such images to generate a 3D mask was realised by using the ASTRA toolbox [134]. A discrete algebraic reconstruction tomography (DART) algorithm was used to avoid artefacts originating from the missing wedge [135]. Fig. 7.4 shows the reconstructed 3D shape of the carbon fibre needle. This reconstruction shows that the needle-shaped geometry (side view in Fig. 7.4a) has a rounded rectangular cross-section (top view in Fig. 7.4b). Two central slices from the *xy* and *yz* planes, which are also shown in Figs. 7.4c-d, respectively, indicate slight asymmetry in the x and z directions of the cross-section of the needle.

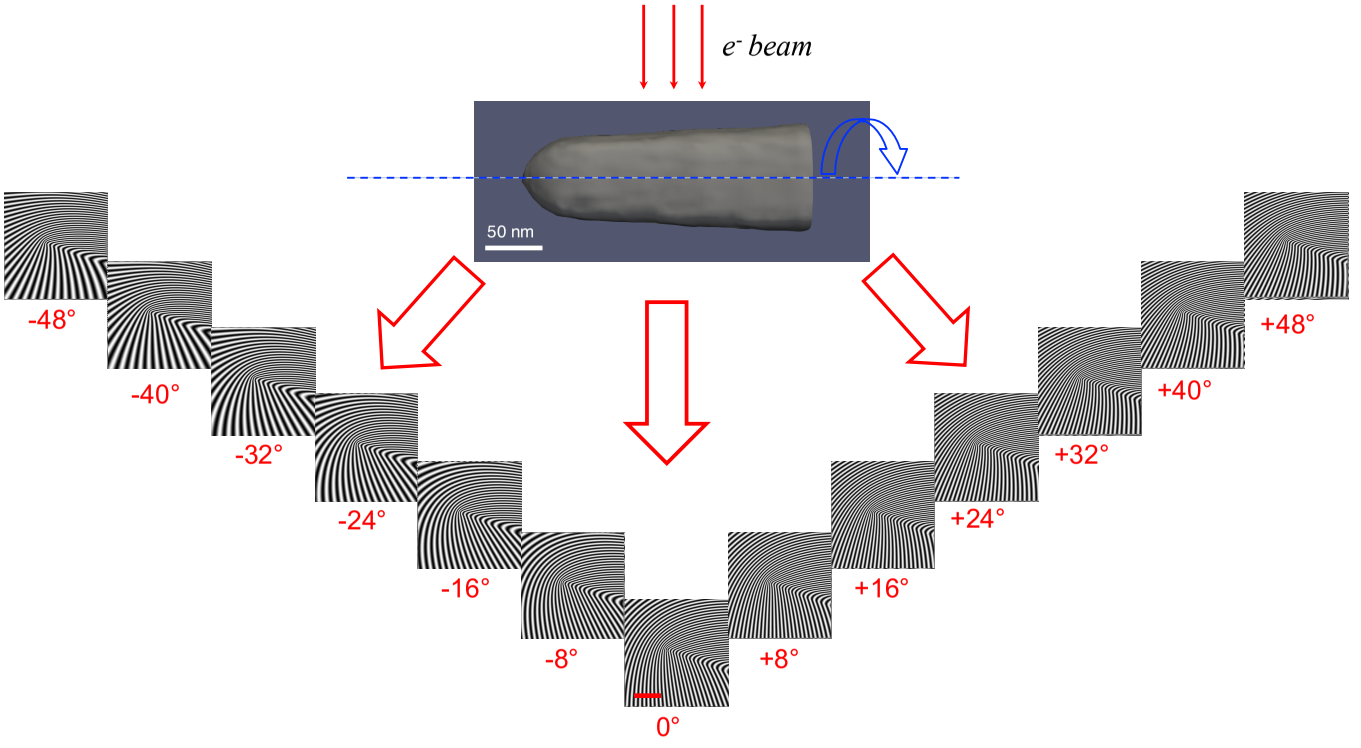

Fig. 7.3 Examples of phase contour maps generated from a tomographic tilt series of off-axis electron holograms with the needle electrically biased at +40 V. The tilt angle is indicated next to each image. The contour spacing is π radians. The MIP contribution to the phase was removed before calculating each phase contour map. In the full tilt series, the tilt increment is 4° and the tilt angle range is from $-52°$ to $+48°$. The scale bar (shown in the 0° image) is 400 nm.

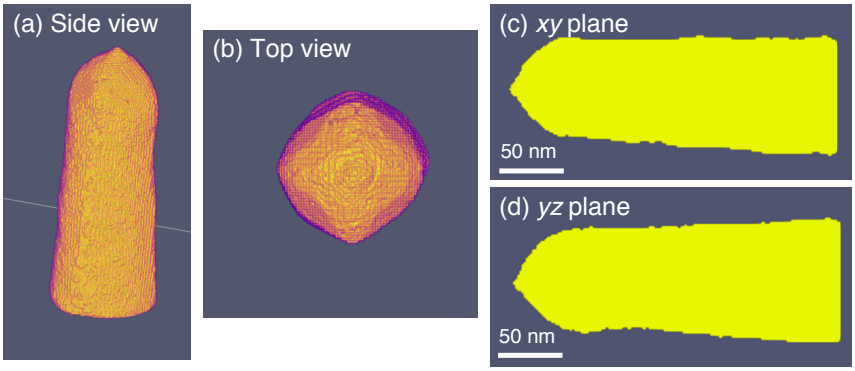

Fig. 7.4 3D shape of the carbon fibre needle reconstructed from a tomographic tilt series of images of the MIP contribution to the phase, showing (a) a side view and (b) a top view. (c, d) Two central slices showing the *xy* and *yz* planes. The needle is marked in yellow. The reconstructed surface was used as a 3D mask for model-based iterative reconstruction of charge inside the needle-shaped specimen. See text for details.

7.2.3 3D charge, electric field and electrostatic potential

3D reconstruction of the charge density in the needle was carried out using the model-based iterative reconstruction approach described in Chapter 5. The position of the surface normal vector of the counter-electrode was measured experimentally to be (-4.5, 0, 0) μm from the apex of the needle and the counter-electrode. The sampling density of the original holograms was approximately 1.7 nm. The final voxel size in the reconstruction was therefore chosen to be 1.7 nm. However, the true spatial resolution of each reconstructed phase image was limited (by the size of the sideband used for reconstruction) to be approximately 5 nm. An 8-pixel-wide buffer region was used to take into account contributions from charges outside the FOV and the PRW effect. The optimal regularisation parameter was set to 1000 based on L-curve analysis.

Fig. 7.5 shows a visualisation of the reconstructed 3D charge density in the carbon fibre needle. The charge density is greatest at the apex of the needle, which has the highest curvature. The maximum charge density is 2.94 $\times 10^{18}$ cm^{-3}. The charge is distributed asymmetrically on the sides of the needle, as it is not exactly round. It should be noted that such an effect can also originate from the reconstruction algorithm, for example if the boundary buffer pixel approach that is used to represent charges outside the FOV and the PRW effect does not work effectively, or if the 3D mask is not defined correctly.

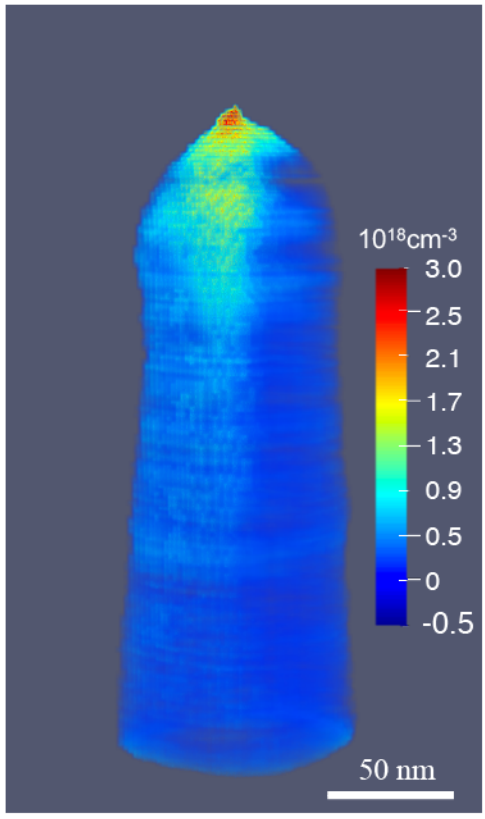

Fig. 7.5 Visualisation of the 3D charge density in a carbon fibre needle reconstructed using the MBIR approach. The carbon fibre needle is biased at +40 V with a distance of 4.5 μm from the counter-electrode. See text for details.

Selected 2D slices extracted from the 3D reconstruction are shown in Figs. 7.6 and 7.7. The *xy* plane of the reconstructed charge density (Fig. 7.6a) reveals an asymmetry in the charge density (white arrow "1"), which is absent in the *yz* plane (Fig. 7.6b). This difference may be a result of the missing wedge, since the tilt series is recorded about a single axis (the *y* axis). The fact that the majority of the charges are located on the surface of the needle (although their penetration into the surface is considerable) is visible in the *yz* plane (Fig. 7.6b) and is consistent with the prediction based on classical electrostatics that charges reside on the outer surface of a conductor [127]. Interestingly, in both planes, there is another region with a locally increased charge density, which is marked by red dashed ellipses in Figs. 7.6a-b. This observation may be associated with the fact that the apex of the the carbon fibre needle was damaged by sample preparation (*e.g.*, Ga bombardment) and its conductivity was

locally reduced. The apex and perhaps also the surface of the needle can then be regarded as more insulating than the rest of the needle. In the presence of an applied electrical bias, charge may then build up at the interface between the insulating apex (as well as the surface) and the more conductive shank of the needle.

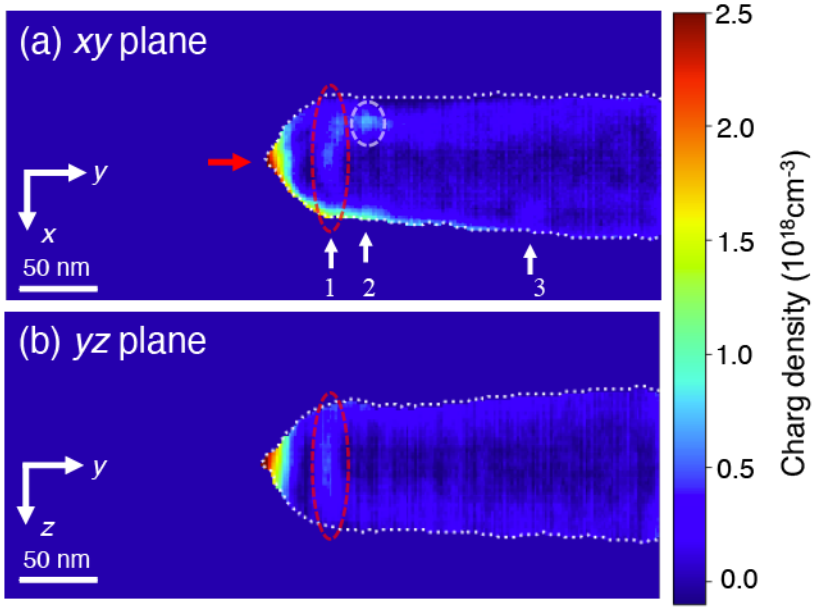

Fig. 7.6 2D slices of charge density in the (a) *xy* and (b) *yz* plane extracted from the 3D reconstructed charge density (shown in Fig. 7.5). The white dashed lines mark the outline of the needle.

In three representative *xz* planes, the charge can be seen to be located primarily at the surface of the needle (Figs. 7.7a-c). Plane "1" (labelled in Fig. 7.6a) corresponds to the interface that is expected to be present between the more insulating apex and the conductive shank of the needle. Plane "2" intersects a local maximum in the charge density (marked by a white dashed ellipse in Fig. 7.6a). Plane "3" corresponds to a plane that is at a greater distance from the apex. Planes "2" and "3" shows an approximately core-shell-like charge distribution, with the charge localised at the outer surface of the needle. Plane "2" shows an additional localisation of charge at one corner, as also shown in Fig. 7.6a.

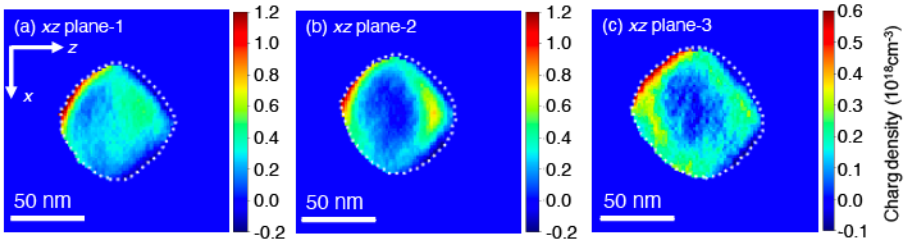

Fig. 7.7 Three representative 2D slices of charge density in the *xz* plane extracted from the 3D reconstructed charge density (shown in Fig. 7.5). The planes are indicated by white arrows and numbers in Fig. 7.6a. The white dashed lines mark the outline of the needle.

Corresponding charge density profiles are shown in Fig. 7.8 for a quantitative comparison. Fig. 7.8a shows a line profile of the charge density in the *xy* plane along the needle axis (indicated by a red arrow in Fig. 7.6a). In addition to a maximum at the apex, there is another local maximum with a charge density of approximately 0.5×10^{18} cm^{-3}. The charge density along the axis of the rest of needle is almost zero, as expected for a conductor. For the three chosen *xz* planes, line profiles of the measured charge density are plotted in both the *z* and the *x* direction in Figs. 7.8b-c, respectively. In the *z* direction (Fig. 7.8b), the green and blue profiles from planes "2" and "3" are almost symmetrical with respect to the needle axis. The red profile from plane "1" is higher than those from planes "2" and "3" on the axis of the needle. In the *x* direction (Fig. 7.8c), the blue profile from plane "3", which is far from the curved apex, is symmetrical. The red profile from plane "1" is again higher on the axis of the needle than the other two profiles. The cumulative charge integrated along the axis of the needle, which is shown in Fig. 7.6d, follows an almost linear trend, indicating an almost constant line charge density along the needle. However, at the apex of the needle, the slope of the cumulative charge profile is slightly greater than in the shank, indicating a greater line charge density in this region, perhaps because of its more insulating character or because of a deviation from ellipsoidal geometry at the apex of the needle.

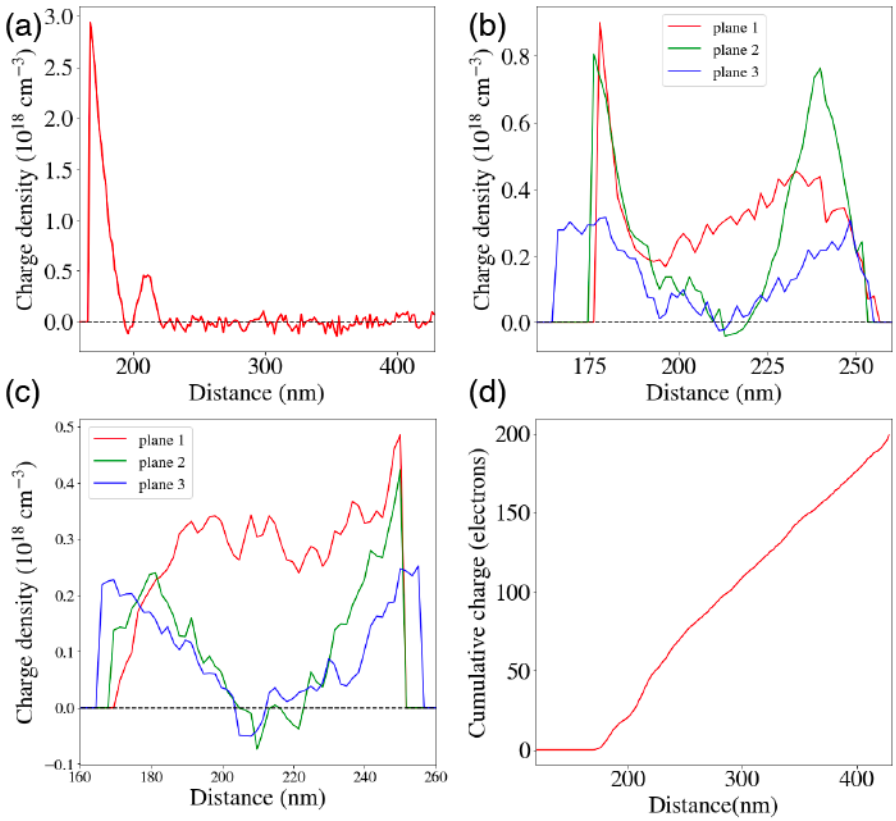

Fig. 7.8 Line profiles of charge density extracted from the 3D charge density shown in Fig. 7.5 (a) along the axis of the needle (y) in the central xy plane (marked by a red arrow in Fig. 7.6a) and (b, c) along z and x in three different xz planes (1-red, 2-green, 3-blue) marked in Fig. 7.6a. (d) Cumulative charge profile integrated along the axis of the needle.

The 3D electric field and electrostatic potential can be calculated from the 3D reconstructed charge density, on the assumption that the image charges are defined by the counter-electrode having a norm vector with respect to the apex of the needle of $(-4.5,\ 0,\ 0)$ μm. Fig. 7.9a show a 3D visualisation of the electric field strength of the needle, while Figs. 7.9b-c show two slices of electric field strength in the central xy and yz planes. The electric field is almost rotationally symmetrical about the needle axis, with slight asymmetry resulting from the asymmetry in the reconstructed charge density (as seen in the xy plane in Fig. 7.9b). The fact that the electric field is strongest close to the apex is visible in the xy and yz planes shown in Figs. 7.9b-c. The electric field decays rapidly into the vacuum region with increasing

distance from the apex. Detailed comparisons with models for electric fields used by the atom probe community and finite element simulations of electric fields of needle-shaped specimens will be beneficial in the future. The maximum electric field strength measured in the present study is approximately 0.25 GV/m. Based on a single projection model [59] used by the atom probe community, the geometric field factor here is predicted to be approximately 5.33, which falls within theoretical values ranging between 3 and 8 [136, 137]. Inside the needle (Figs. 7.9b-c), the physical meaning of the electric field remains to be discussed, with reference to the dielectric constant of the specimen. It is interesting that the electric field appears to be finite only in the region of the specimen close to the surface, where it may be less conducting. Nevertheless, the measurement of the electric field around the needle is likely to be adequate for the atom probe or field emission community to calculate the trajectories of ions or electrons.

Figs. 7.10a-b show two slices of the electrostatic potential from the central *xy* and *yz* planes, respectively. The electrostatic potential is almost symmetric with respect to the axis of the needle in both planes. The outer surface of the needle is measured to be an equipotential of 25 V, which is smaller than the applied bias voltage of 40 V. This drop in voltage may result from the contact of the specimen to ground or the presence of less conducting surface of the needle due to sample preparation damage.

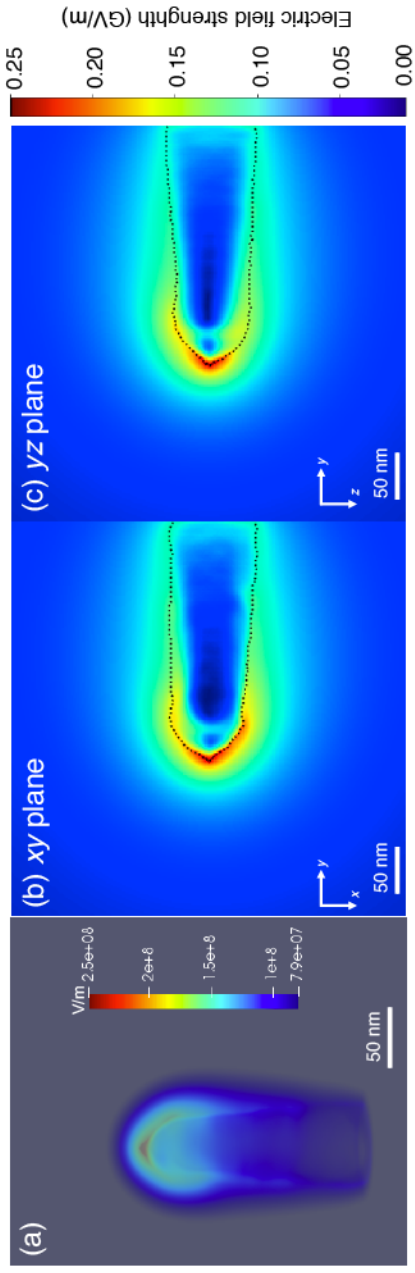

Fig. 7.9 3D electric field determined from the reconstructed 3D charge density shown in Fig. 7.5 for the electrically-biased carbon fibre needle. (a) Strength of the electric field (plotted on a logarithmic scale). (b, c) Strength of the electric field in the central xy and yz planes, respectively. The black dashed line shows the outline of the needle.

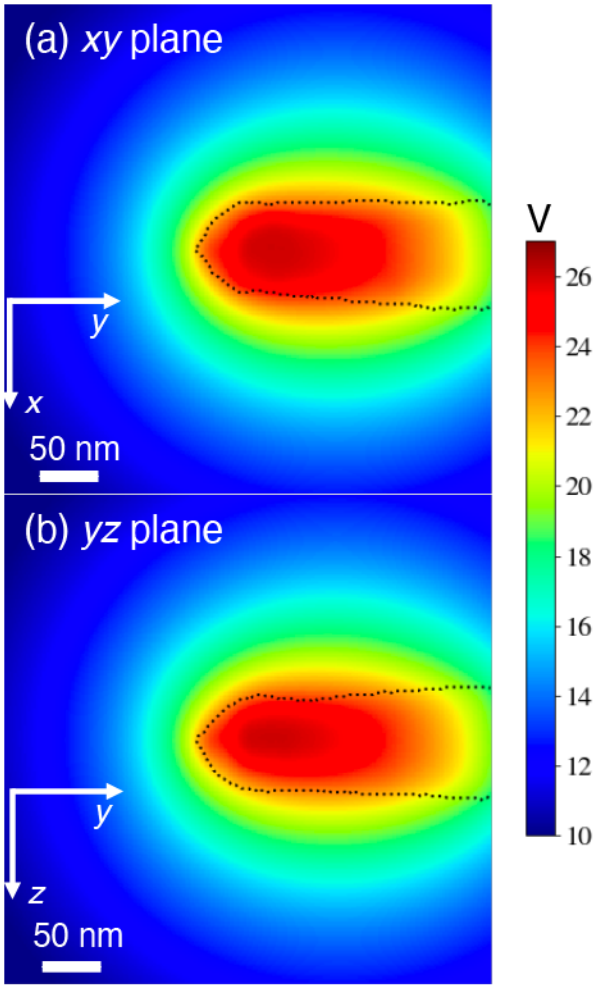

Fig. 7.10 3D electrostatic potential determined from the reconstructed 3D charge density shown in Fig. 7.5 for the electrically-biased carbon fibre needle. (a, b) slices of the electrostatic potential in the central *xy* and *yz* planes, respectively. The black dashed line shows the outline of the needle.

For better visualisation, a combination of a streamline plot in the central *xy* plane of the electric field and a contour map of the electrostatic potential is presented in Fig. 7.11. The fact that the field lines on the right side of the image (close to the bottom the needle in the FOV) lie at an inclined angle to the surface of the needle results from the presence of charges, which are not fully compensated by the boundary buffer pixel approach. Nevertheless, in the

middle region of the needle, the field lines travel along the normal to its surface, implying that charges outside the FOV do not influence the reconstruction of charge density and electric field far from them. This result highlights the fact that the electric field around the apex of a needle can be reliably calculated using the MBIR approach.

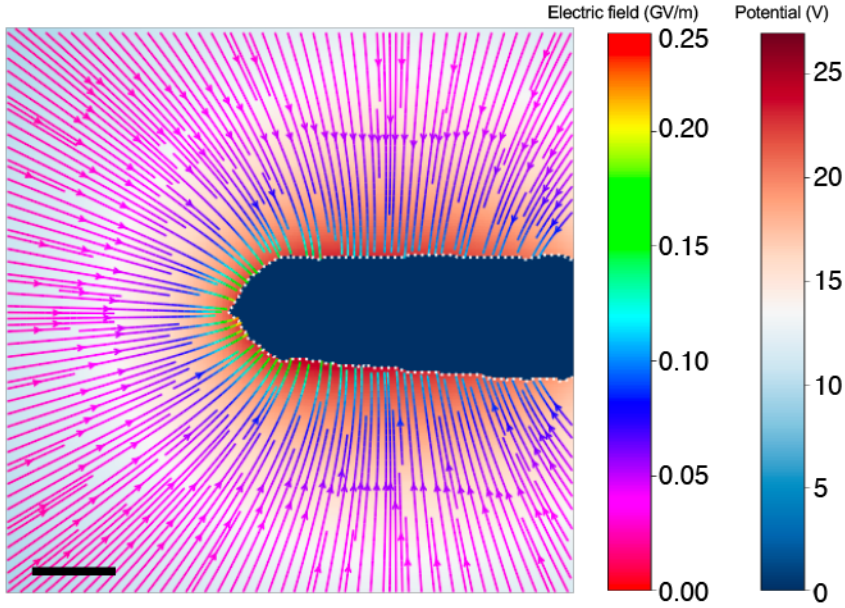

Fig. 7.11 Combination of a streamline plot of the electric field and a plot of the electrostatic potential in the central *xy* plane of the reconstructed volume of a carbon fibre needle. The interior of the needle is marked in blue. The scale bar is 50 nm.

7.3 Summary and conclusions

In this chapter, the 3D charge density, electric field and electrostatic potential of an electrically-biased carbon fibre needle have been determined experimentally using the model-based iterative reconstruction approach. Tomographic tilt series of holographic phase images with the needle biased at 40 V were used as input to the algorithm after subtracting the MIP contribution to the phase from each image in the tilt series. The reconstructed charge density is greatest at the apex of the needle and is localised primarily on its surface, as expected based on classical electrostatics. The cumulative charge profile displays an almost linear behaviour, which is consistent with the presence of a constant line charge density along

the needle. Asymmetry in the reconstructed charge density can be ascribed to the local curvature of the needle or to artefacts of the reconstruction procedure. The algorithm is robust against many of the artefacts that would affect conventional backprojection-based tomographic reconstruction methods and is able to retrieve 3D details of the charge density regardless of the symmetry of the specimen. The 3D electric field and electrostatic potential are then calculated from the reconstructed 3D charge density on the assumption that the positions of image charges can be determined by the position of the counter-electrode. The inferred electric field and electrostatic potential both have almost rotational symmetry about the needle axis. The strength of the electric field is greatest close to the apex region of the needle (outside it) and has a maximum value of approximately 0.25 GV/m for an applied bias voltage of 40 V and a distance of 4.5 μm from the counter-electrode. Further work is required to compare the present results with finite element simulations of the electric field, as well as with calculations that the atom probe community routinely use for the reconstruction of 3D atom positions. Nevertheless, the results presented here is highly encouraging and the approach can be used routinely for 3D characterisation of charge, electric field and electrostatic potential distributions from limited datasets.

Chapter 8

Measurement of electron-beam-induced charging

Electron-beam-induced charging is a fundamental phenomenon that particularly affects electron microscopy studies of non-conductive materials (including biological specimens) and semiconductors. It is influenced by the electronic band structure and secondary electron generation and emission from the specimen (in particular from its surfaces).

In order to investigate electron-beam-induced charging phenomena, needle-shaped specimens comprising an insulating apex (Al_2O_3) and a conductive Cr_2AlC base were studied. (See Chapter 3 for details about the specimens.)

8.1 Specimen geometry and morphology

Fig. 8.1a shows the geometry of a Cr_2AlC-Al_2O_3 needle. The needle has a length of 15 μm and is attached to a conductive Cu post (not shown). Two other protrusions from the post, which are present approximately 10 μm from the primary needle, are assumed to have little influence on its charging state. Fig. 8.1b shows a high-magnification bright-field TEM image of the interface between the Cr_2AlC phase and the Al_2O_3 apex viewed almost edge-on.

Fig. 8.2 shows elemental maps of the needle recorded using STEM-EDS. This figure also shows a STEM-HAADF image, in which two interfaces are visible: one between the Cr_2AlC phase and Al_2O_3 apex (marked by a red dashed line) and another curved interface (marked by a blue dashed line) resulting from Cr diffusion into the Al_2O_3 apex. Cr in the Al_2O_3 apex may take the form of Cr_2O_3. This specimen geometry suggests that there may be a metal (Cr_2AlC)/semiconductor (possibly $p-$type Cr_2O_3 [138])/insulator (Al_2O_3) junction, instead of a metal/insulator junction, in the present needle.

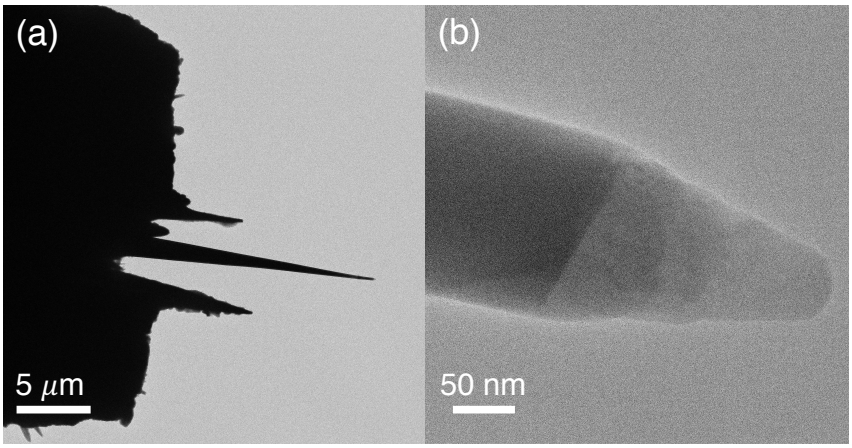

Fig. 8.1 Geometry of the Cr_2AlC-Al_2O_3 needle-shaped specimen examined in this section. (a) The whole needle. (b) High-magnification bright-field TEM image of the apex of the needle.

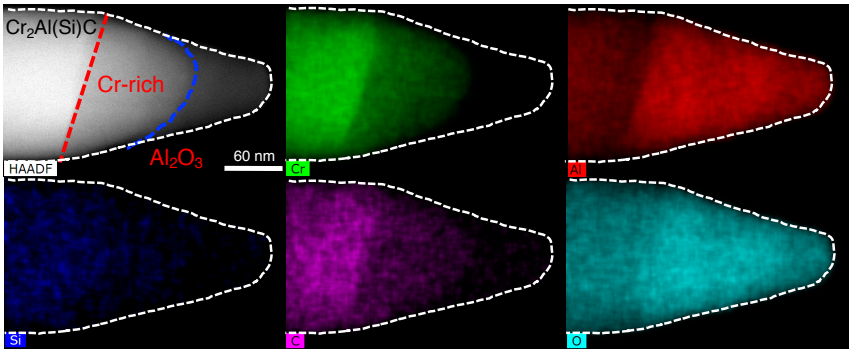

Fig. 8.2 STEM-HAADF and STEM-EDS elemental maps of a Cr_2AlC-Al_2O_3 needle-shaped specimen. The red dashed line in the HAADF image marks the interface between the Cr_2AlC phase and the Al_2O_3 apex. The blue dashed line marks the interface between a Cr-rich area and the Al_2O_3 apex. The white dashed line in each image marks the outline of the needle.

8.2 Electron-beam-induced charging

As a result of the insulating nature of Al_2O_3, the apex of the needle becomes positively charged due to secondary electron emission when it is illuminated by high-energy electrons. Off-axis electron holography was used to evaluate its charging behaviour. Holograms were recorded at a nominal magnification of 24,500 in Lorentz mode, with the needle illuminated by a parallel electron beam at a nominal dose rate of approximately 4.2 $e/\text{Å}^2/\text{s}$ (30 *e.p.s.*). The exposure time for each hologram was set to 6 s. The biprism was oriented perpendicular to the needle axis and the biprism voltage was set to 100 V. A representative hologram is shown in Fig. 8.3a. The FOV is approximately 600 nm. The holographic interference fringe spacing is 1.3 nm, resulting in a spatial resolution of approximately 4 nm in reconstructed amplitude and phase images which are shown in Figs. 8.3b-c, respectively.

The fact that the apex is positively charged is apparent from the phase image, as the phase decreases from the apex of the needle into the vacuum surrounding it, as shown in the form of a phase profile in the inset to Fig. 8.3c. A corresponding phase contour map (Fig. 8.3d) reveals the presence of concentric projected equipotential contours, whose form suggests that there is also a negatively charged region (possibly associated with screening charges) in the Cr_2AlC phase adjacent to the interface, as a single sign of the charge density would decay more slowly and result in contours similar to those observed around the emitter. (See Sections 4.2, 6.1 and 7.2.1.) It should be noted that the amplitude is flat in the vacuum region around the needle in Fig. 8.3b, as the electric field is relatively weak in this region and can be treated as a slowing-varying strong phase object. The MIP contribution to the phase could not be removed because the needle was always charged by electron beam illumination.

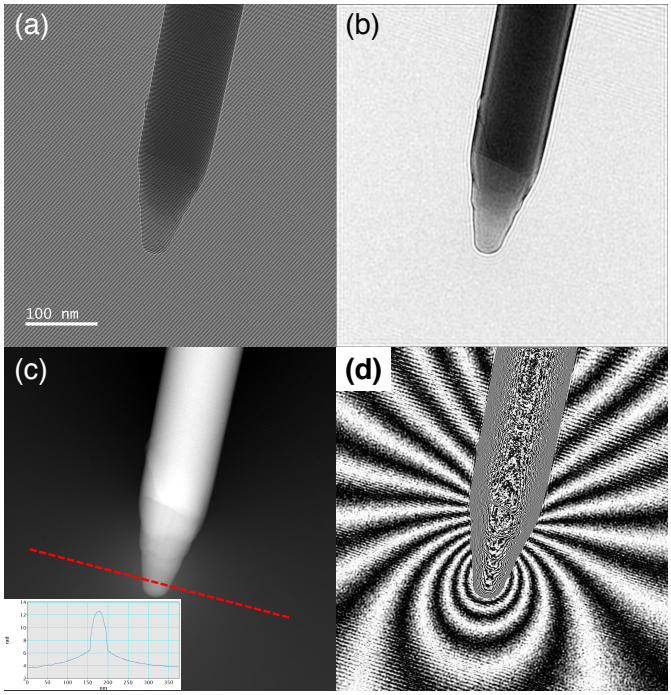

Fig. 8.3 Off-axis electron holography of electron-beam-induced charging of a Cr_2AlC-Al_2O_3 needle-shaped specimen illuminated by high-energy electrons. (a) Off-axis electron hologram. (b) Reconstructed amplitude image. (c) Reconstructed unwrapped phase image shown together with a phase profile across the apex (marked by a red dashed line) in the inset. (d) Phase contour map. The phase contour spacing is $\frac{2\pi}{12}$ radians. The electron dose rate was approximately 4.2 $e/\text{Å}^2/\text{s}$.

An analytical line charge model was used to confirm the presence of a dipole-like charge state in the needle resulting from electron beam illumination. A similar model has been applied successfully in simulations of holographic phase images recorded from charged tips and nanotubes, for which analytical expressions are available both for the electrostatic potential and for the holographic phase shift. (See Chapter 4 and Appendix B.)

For the present inhomogeneous needle, two aligned line charges with different lengths of 10 μm and 100 nm, respectively, were initially used, with image line charges added to model the effect of the conductor at the base of the needle. The base was simply assumed to be a conducting plane perpendicular to the line charges. By adjusting the values of the charge density to obtain a phase contour map that approximates the experimental measurement, satisfactory agreement was only obtained for charge density distributions with different signs.

The phase contour map shown in Fig. 8.4, which covers a square region of side 400 nm, provides a best fit when the charge density in the apex is assumed to be 8 $e/$nm and that in the supporting base is assumed to be -2 $e/$nm. The PRW effect was also taken into account in this analysis, on the assumption of an interference distance of 650 nm.

The presence of a dipole-like charge state in the illuminated needle was therefore confirmed using an analytical line charge model. The origin of the dipole-like charge state is not clear yet, as a result of the complexity of the contact between the apex and the conductive base and the unknown surface state in the needle.

Fig. 8.4 Phase contour map simulated using an analytical line charge model. The phase contour spacing is $\frac{2\pi}{12}$ radians. The white area denotes the needle itself. See text for details.

8.3 Dose rate dependence

In order to asses the dose rate dependence of electron-beam-induced charging of the present needle-shaped specimen, the TEM spot size was changed while keeping the illuminated area the same. The dose rate was estimated from the direct electron counting Gatan K2-IS camera. The total dose was controlled by the exposure time. Off-axis electron holograms were recorded in Lorentz mode at a nominal magnification of 14,500. The holographic

interference fringe spacing was 3 nm. The biprism was oriented parallel to the needle axis and the biprism voltage was set to 100 V.

Fig. 8.5 shows phase contour maps recorded with the needle illuminated using different spot sizes (*i.e.*, different dose rates) and for different exposure times (*i.e.*, different total doses). The rows show phase contour maps with increasing total dose from left to right, corresponding to exposure times of 4, 8, 12, 16 and 20 s. The columns show phase contour maps with different dose rates of 1.84, 0.96, 0.24 $e/\text{Å}^2/\text{s}$ from top to bottom, obtained by changing the spot size from 2 to 3 and then 5. For exposure times longer than 4 s, the dose rate, rather than the total dose, is observed to determine the charge state, as the phase contour maps remain almost unchanged from left to right in Fig. 8.5. Intriguingly, on increasing the dose rate (from bottom to top in Fig. 8.5), the density of the phase contours becomes greater in the region of the conductive base, but smaller in the region of the insulating apex, suggesting that the apex becomes more strongly (positively) charged when the dose rate is decreased.

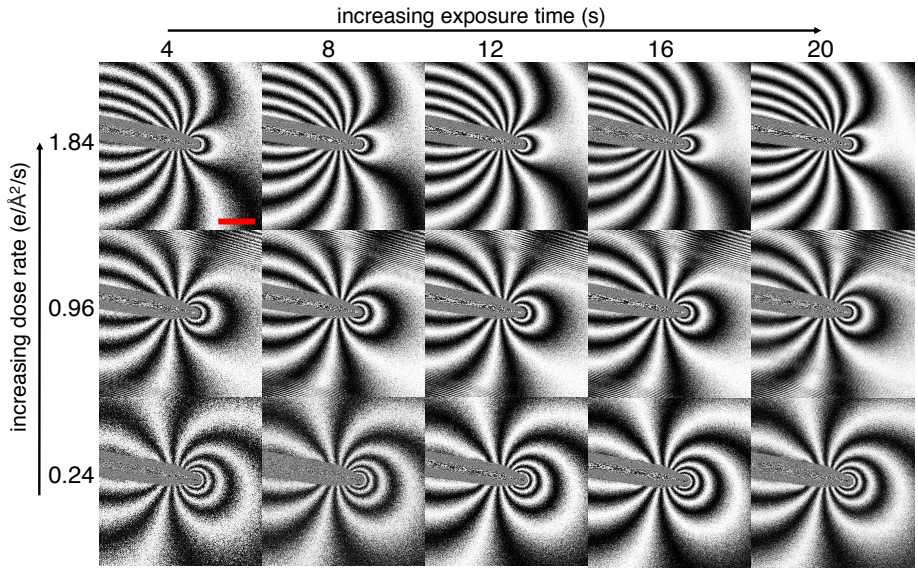

Fig. 8.5 Phase contour maps recorded with the needle illuminated using different dose rates and exposure times. The phase contour spacing is $\frac{2\pi}{12}$ radians. From top to bottom, the dose rate was 1.84, 0.96 and 0.24 $e/\text{Å}^2/\text{s}$, respectively. From left to right, the exposure time was 4, 8, 12, 16 and 20 s, respectively. The scale bar is 300 nm.

8.4 Temperature dependence

As temperature can change the surface state of a specimen, the number of electrons near the Fermi level, as well as its electrical conductivity, is expected to influence its electron-beam-induced charging behaviour.

Fig. 8.6 shows phase contour maps recorded with the needle-shaped specimen studied using different dose rates at different temperatures. At room temperature (upper row in Fig. 8.6), the charge state evolves similarly to the behaviour described above for higher dose rates of 2.68, 1.42 and 0.88 $e/\text{Å}^2/\text{s}$, while at lower dose rates the charge state remains almost unchanged. After cooling to 95 K (middle row in Fig. 8.6), the density of the contours becomes greater than those at room temperature at all dose rates, indicating that the needle is more highly charged. The charge state follows the same dose-rate-dependent behaviour as in the previous section, with the density of the contours becoming greater near the conductive base region and smaller near the insulating apex region at higher dose rates. The needle was then heated to 200 K (lower row in Fig. 8.6). Surprisingly, the charge state did not follow the same trend as in the upper and middle rows in Fig. 8.6, exhibiting no dependence on dose rate, but consistently showing the charge state that was observed at 95 K for a dose rate of 2.68 $e/\text{Å}^2/\text{s}$.

The temperature-dependent charging results suggest that the surface state may play an important role in electron-beam-induced charging, as the temperature of the specimen may modify the presence of hydrocarbons, water or other contamination on its surface. A higher temperature may help to clean the specimen surfaces. The use of a UHV TEM column and the examination of ultra-clean specimen surfaces without preparation damage may ultimately be required to understand intrinsic electron-beam-induced charging phenomena. The present results also highlight the fact that a knowledge or a reasonable assumption of the surface state of a specimen may be necessary to conclusively interpret observations of electron-beam-induced charging.

The observation of "frozen" charges on the specimen surface in this section (200 K, lower panel in Fig. 8.6) highlights the fact that charging effects can depend on physical changes to the surface of the specimen, in addition to other effects, such as the presence of metal/semiconductor/insulator junctions and the generation and recombination of electron-hole pairs. Accordingly, similar experiments were carried out with different bias voltages applied to the needle-shaped specimen. The results are described in the following section.

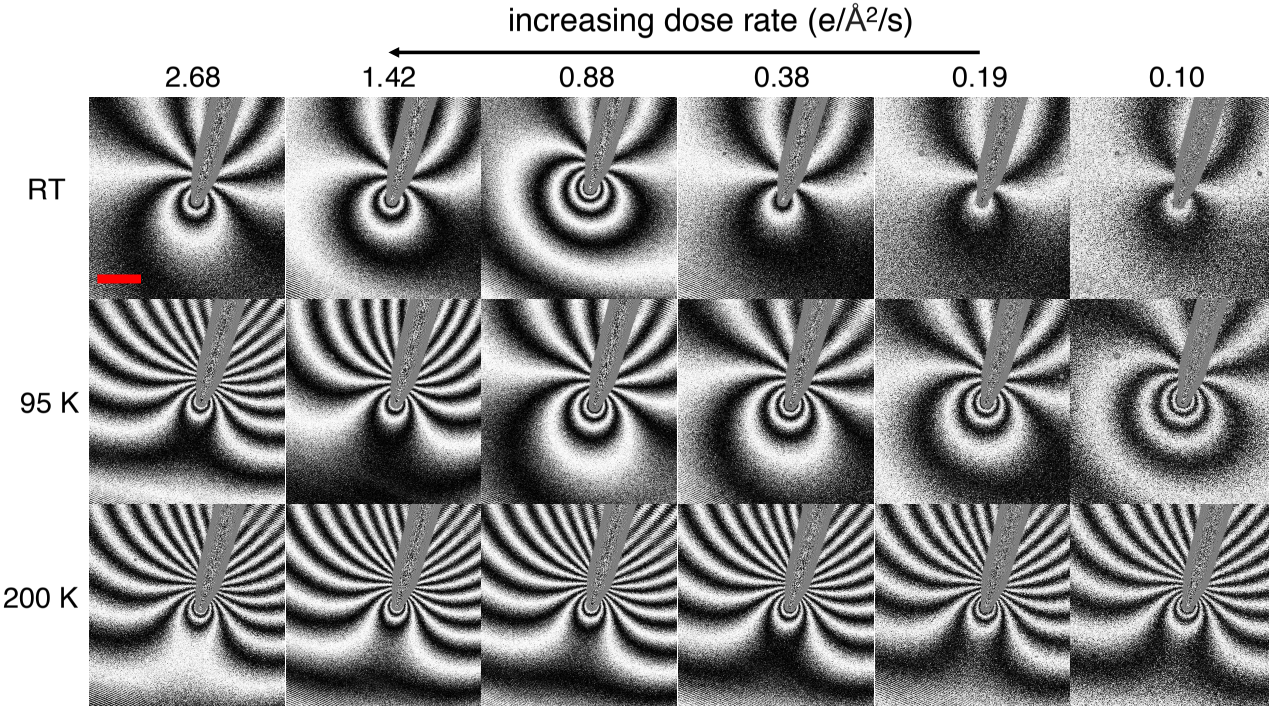

Fig. 8.6 Phase contour maps recorded with the needle illuminated using different dose rates and examined at different temperatures. The phase contour spacing is $\frac{2\pi}{12}$ radians. The annotations on the left denote the temperature while the numbers along the top denote the dose rate. The needle was measured first at room temperature (RT), then at 95 K and finally at 200 K. Holograms were recorded in sequence from the lowest to highest dose rates. The exposure time for each image acquisition was 8 s. The scale bar is 300 nm.

8.5 Bias voltage dependence

As a result of the special requirements for the specimen geometry when using the STM-TEM holder for electrical biasing experiments (see Chapter 3), a different needle-shaped specimen with a similar morphology was used. A low-magnification bright-field TEM image of the specimen is shown in Fig. 8.7a. The needle had a length of approximately 18 μm and widths of 1.5 μm at its lower end and 90 nm at its apex. The separation between the needle and the W counter-electrode was approximately 5 μm. The spot size was set to 3, corresponding to a dose rate of approximately 0.94 $e/\text{Å}^2/\text{s}$. Off-axis electron holograms were taken in Lorentz mode at a nominal magnification of 14,500. The holographic interference fringe spacing was 3 nm and the biprism was oriented parallel to the needle axis. Fig. 8.7b shows a phase image, which includes contributions from the MIP and electron-beam-induced charging. Fig. 8.7c shows a corresponding phase contour map, which confirms that this needle displays similar charging behaviour to the needle described above.

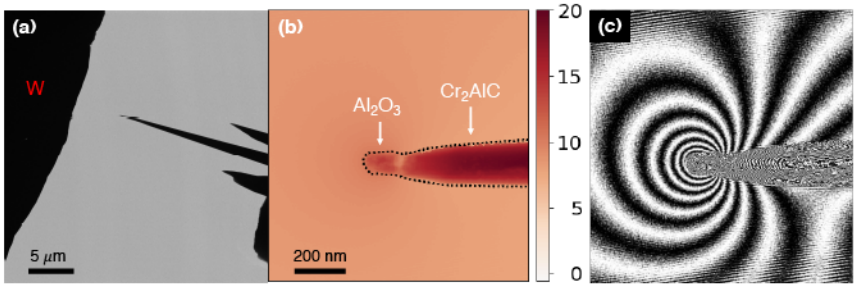

Fig. 8.7 Results obtained from a different Cr_2AlC-Al_2O_3 needle-shaped specimen during electrical biasing experiments. (a) Low-magnification bright-field TEM image of the specimen and the experimental setup. (b) Phase image, which includes contributions from both the MIP and electron-beam-induced charging, shown in radians. (c) Corresponding phase contour map. The phase contour spacing is $\frac{2\pi}{12}$ radians.

The needle was then electrically biased at voltages of between ± 1 and ± 20 V. Fig. 8.8 shows phase contour maps recorded at each applied bias voltage. With the MIP contribution to the phase removed by subtracting the phase image recorded without a bias voltage applied to the needle (Fig. 8.7b), the fact that the density of the phase contours does not depend on the sign of the applied bias voltage suggests that the contribution to the phase from electron-beam-induced charging does not depend on applied bias voltage.

Cumulative charge profiles along the needle were calculated using Eq. 2.9 and are shown in Fig. 8.9. The integration region was allowed to shrink along the needle axis towards the apex (from right to left in Fig. 8.8). The quasi-linearity of the cumulative charge profile is

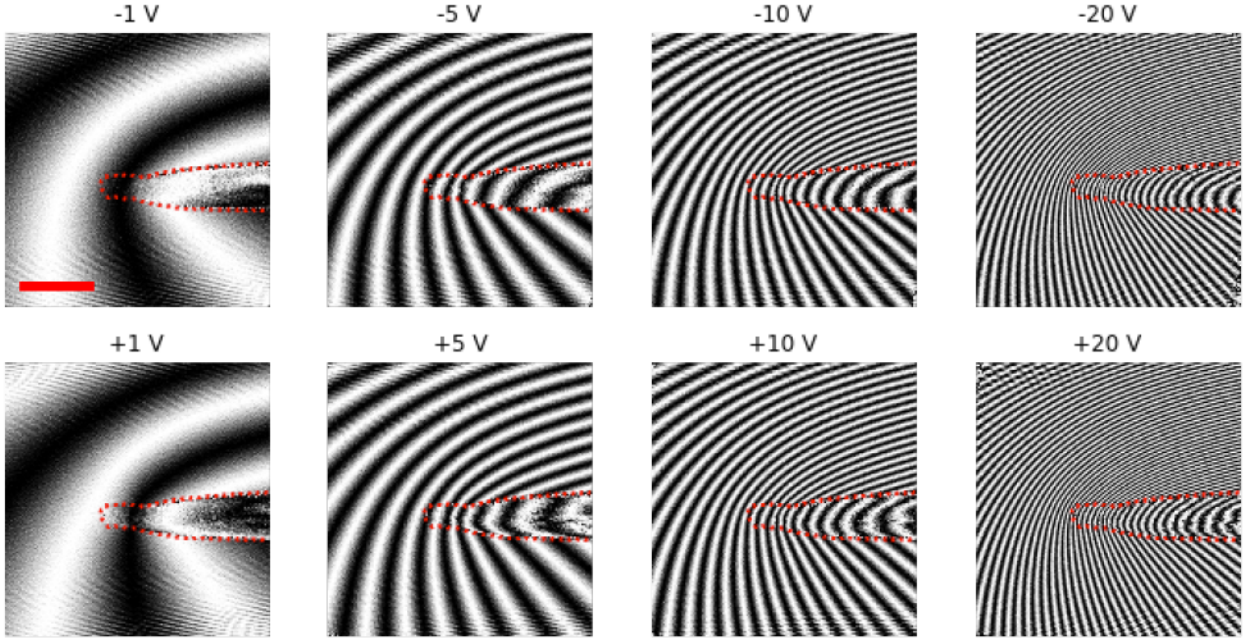

Fig. 8.8 Phase contour maps recorded with the Cr_2AlC-Al_2O_3 needle-shaped specimen electrically biased at voltages of between ± 1 and ± 20 V. The phase contour spacing is $\frac{2\pi}{4}$ radians. Contributions from the MIP and electron-beam-induced charging were removed by subtracting the phase image recorded without a bias voltage applied to the needle. The outline of the needle is marked by a red dashed line in each sub-image. The scale bar is 300 nm.

evident at all of the applied bias voltages, indicating the presence of a constant contribution to the line charge density in the needle from the applied bias voltage, irrespective of the presence of the insulating apex. Slight non-linearity in the apex may be ascribed to the accumulation of charge in this region, as discussed in Chapter 6.

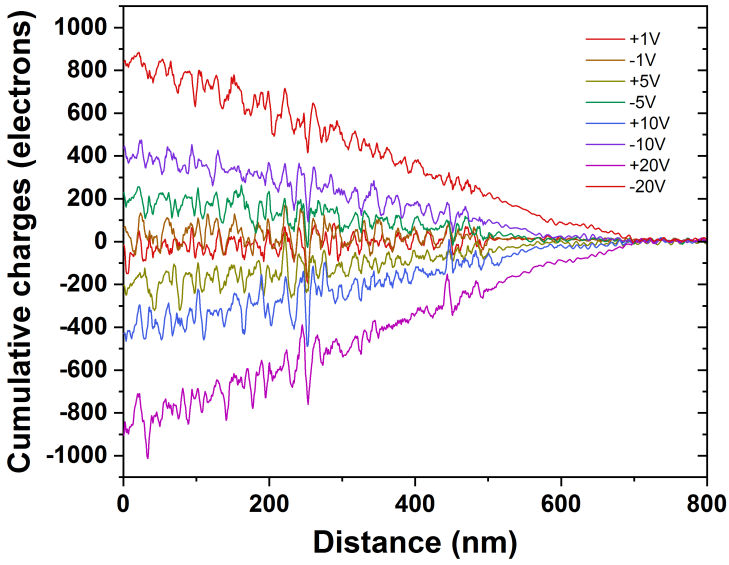

Fig. 8.9 Cumulative charge profiles along the needle axis recorded with the needle electrically biased at voltages of between ± 1 and ± 20 V. See text for details.

The results confirm that the bias voltage applied to the needle does not influence electron-beam-induced charging. This observation is unexpected, as a voltage on the specimen is expected to influence secondary electron emission. As a result of the low energy of the emitted second electrons, which is usually between several eV and several tens of eV, the applied bias voltages used here should have had a considerable influence on charging behaviour. If the specimen is at a positive bias, then emitted secondary electrons should be attracted back to the specimen surface, while at a negative bias, more secondary electrons should be escaped from the surface. Future experiments on specimens with simple geometries of the contact to ground, the shape and morphology of the specimen and the surface would help to understand the charging behaviour of specimens in the presence of an applied electrical bias.

8.6 Examination of an additional needle

An additional (third) similar needle-shaped specimen was examined, both in order to assess the reproducibility of the previous measurements and to perform new experiments that involved changing the energy of the illuminating electrons and to assess the use of plasma cleaning of the needle to alter its surface state.

The third needle has a length of 20 μm and diameters of 80 nm at its apex and 1.5 μm at its lower end. The upper frame in Fig. 8.10a shows a STEM-HAADF image of the apex region of the third needle. The elemental maps in Fig. 8.10 show that this needle contains a triangular-shaped region of Cr diffusion, as highlighted by cyan dashed lines in each image. Inside the Al_2O_3 region, several chromium oxide nanoprecipitates are found. Interestingly, a mixture of (Al, Cr)$_2O_3$ is observed at the very apex of the needle, as labelled by a red dashed line. This morphology is slightly different from that of the two needles that were described in the previous sections. It should be noted that the elemental maps were recorded after the electron-beam-induced charging experiments had been completed, so that the use of a focused scanning TEM probe would not change the surface state of the needle.

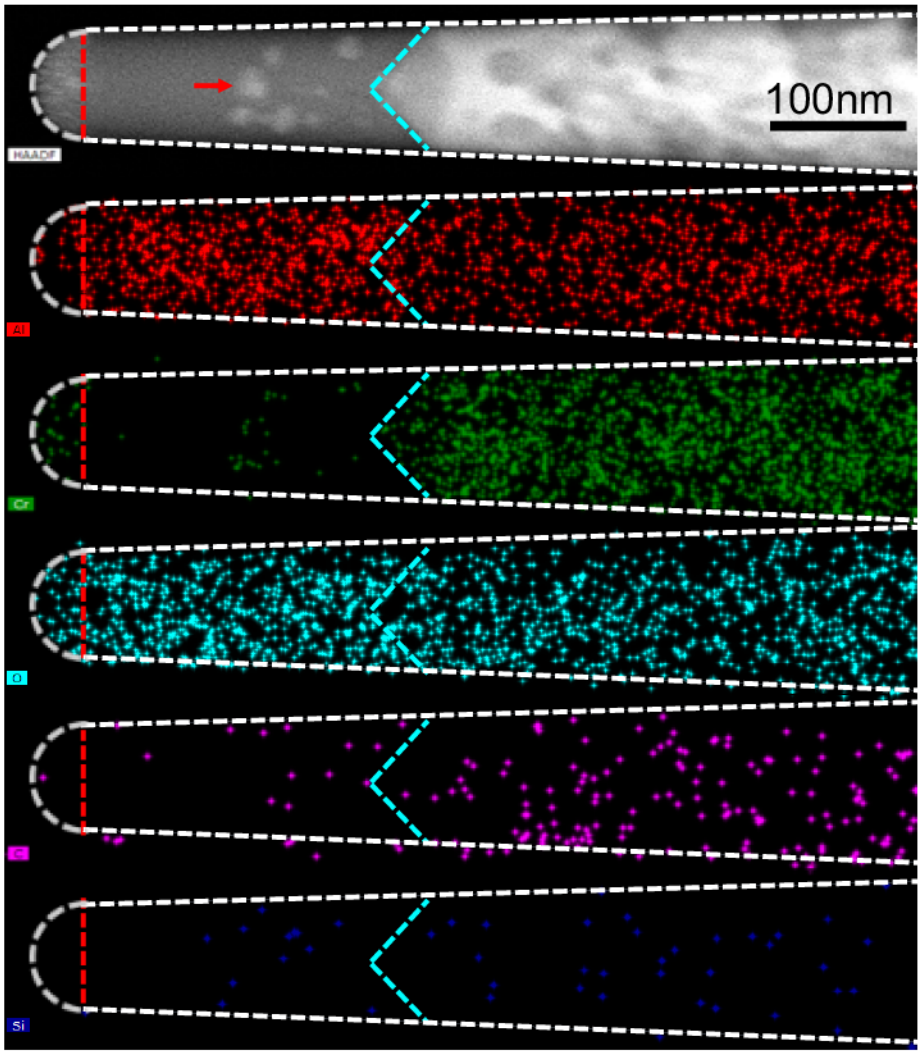

Fig. 8.10 STEM-HAADF image and STEM-EDS elemental maps of the third Cr_2AlC-Al_2O_3 needle-shaped specimen. Elemental distributions for Al, Cr, O, C and Si are shown, as denoted in the lower left corner of each image. A cyan dashed line in each image marks the interface between the Cr_2AlC and the Al_2O_3. A red dashed line marks the interface between the Al_2O_3 and a mixture of $(Al, Cr)_2O_3$ at the very apex. A red arrow in the STEM-HAADF image marks a chromium oxide nanoprecipitate. The outline of the needle is marked by a white dashed line in each sub-image.

8.6.1 Temperature dependence

The temperature dependence of electron-beam-induced charging of this needle was first investigated. Fig. 8.11 shows phase images and corresponding phase contour maps recorded at different temperatures in sequence. All of the images shown here were recorded using a spot size of 2, corresponding to a dose rate of approximately 2.6 $e/\text{Å}^2/\text{s}$ and an exposure time of 8 s, in order to have a high signal-to-noise ratio. Interestingly, no dependence of electron-beam-induced charging on dose or dose rate was observed at any temperature (not shown), in contrast to the results obtained from the first needle. The physics that underlies the dependence of electron-beam-induced charging on dose rate or dose may depend not only on secondary electron emission, but also on the details of the surface state and on contact potentials between different phases in the specimen, which may contain metal/semiconductor/insulator or metal/insulator/semiconductor junctions. Theoretical simulations that include such effects may help to understand experimental measurements in the future.

At room temperature, the third needle became charged in the presence of electron beam illumination (first column in the upper panel in Fig. 8.11), similar to the behaviour observed in the above two needles. The needle was then heated to 50 and 80 °C. Corresponding phase images and phase contour maps are shown in the second and third columns in the upper panel of Fig. 8.11. Charging of the needle was observed to change monotonically with temperature (based on the density of the phase contours at each temperature). This behaviour is expected, as the electron density near the Fermi level and therefore the electrical conductivity is expected to increase with temperature. Surprisingly, however, when the needle was cooled back to room temperature, the charging remained almost the same as at 80°C (fourth column in the upper panel in Fig. 8.11). This observation is unexpected, as the effect of temperature on free charge carrier density should be reversible and suggests that the surface state of the sample changed during examination at different temperatures. The needle was then cooled to −180°C (first column in the lower panel in Fig. 8.11). The number of phase contours increased, indicating stronger charging of the needle, presumably resulting from the thermal dependence of its electrical conductivity. Subsequently, the needle was heated to room temperature (second column in the lower panel in Fig. 8.11), resulting in a reduction in electron-beam-induced charging when compared to any previous state. Interestingly, when the needle was then again heated to 80°C (third column in the lower panel in Fig. 8.11), almost complete elimination of electron-beam-induced charging was observed. This charge state was retained when the needle was finally cooled back down to room temperature (fourth column in the lower panel in Fig. 8.11), in a similar manner to

the first observation during cooling back from 80°C to room temperature (third and fourth columns in the upper panel in Fig. 8.11).

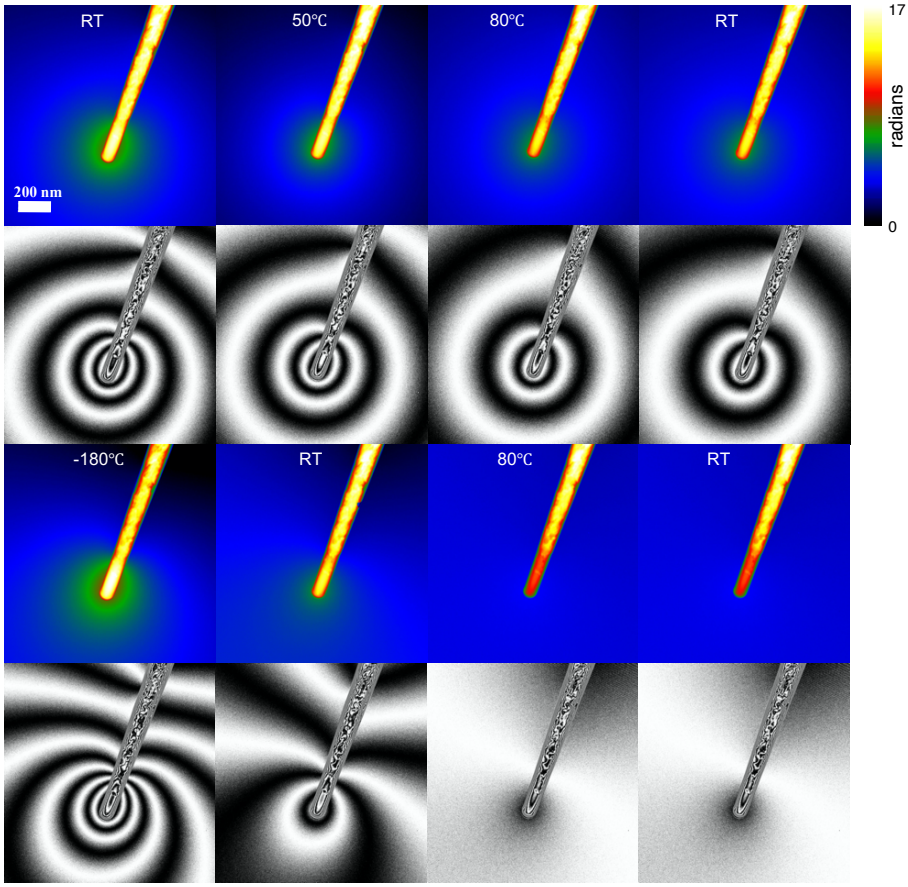

Fig. 8.11 Off-axis electron holography of temperature-dependent electron-beam-induced charging of the third needle, showing phase images (first and third rows) and corresponding contour maps (second and fourth rows). The images are shown in the order, in which they were recorded. The phase contour spacing is $\frac{2\pi}{4}$ radians.

Since electron-beam-induced charging was almost fully suppressed in the final stage of the above cycle, this phase image (fourth column in the lower panel in Fig. 8.11) was used to approximate and subtract the MIP contribution to the phase from the other recorded phase images. The resulting phase difference images could then be used to perform a more reliable and quantitative study of charging using the MBIR approach, as discussed in Chapter 5.

The result of applying this approach to the phase images recorded at room temperature (first column in the upper panel in Fig. 8.11) and at −180°C (first column in the lower panel in Fig. 8.11) are shown in Fig. 8.12. The reconstructed projected charge density distributions in Figs. 8.12a-b show that at −180°C the needle is strongly positively charged in the Al_2O_3 apex. In both cases, the positively-charged region extends approximately 290 nm from the very apex of the needle, which is approximately the same size as the extent of the Al_2O_3 phase (Fig. 8.10).

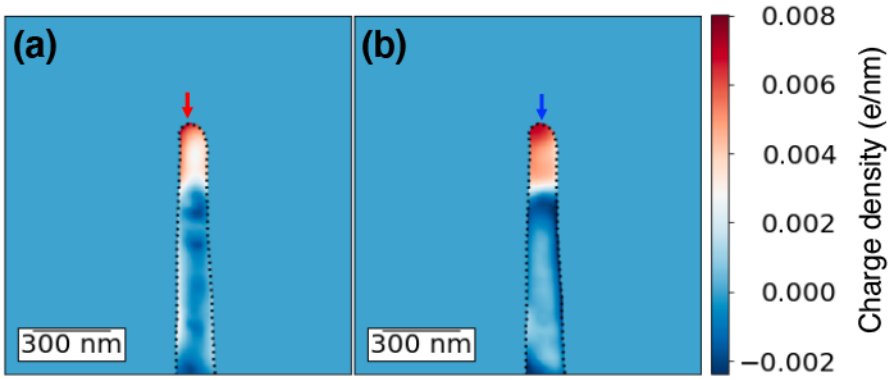

Fig. 8.12 Projected charge density distributions reconstructed from phase images recorded from the third needle at room temperature (first column in the upper panel in Fig. 8.11) and at −180°C (first column in the lower panel in Fig. 8.11), respectively. The MIP contribution to the phase was removed by using the phase acquired at room temperature (fourth column in the lower panel in Fig. 8.11), as electron-beam induced charging was then negligible. The pixel size is 2.86 nm.

The corresponding cumulative charge profiles show that at room temperature (red profile in Fig. 8.13a) the apex of the needle was positively charged with a deficit of 43 electrons, while at −180°C (blue profile in Fig. 8.13a) the apex had a deficit of 52 electrons. Line profiles of the reconstructed projected charge density along the axis of the needle (labelled by an arrow in Figs. 8.12a-b) are shown in Fig. 8.13b. At both temperatures, the charge in the conductive base is relatively small and homogeneous. Interestingly, it is slightly negative at room temperature (red profile in Fig. 8.13b), but slightly positive at −180°C (blue profile in Fig. 8.13b). At −180°C, the charge near the interface reaches a negative maximum and then increases to positive values up to the very apex. These results suggest that the region of Cr diffusion plays a role in charge accumulation near the interface. In the apex region, the charge density at −180°C stayed higher than that at room temperature.

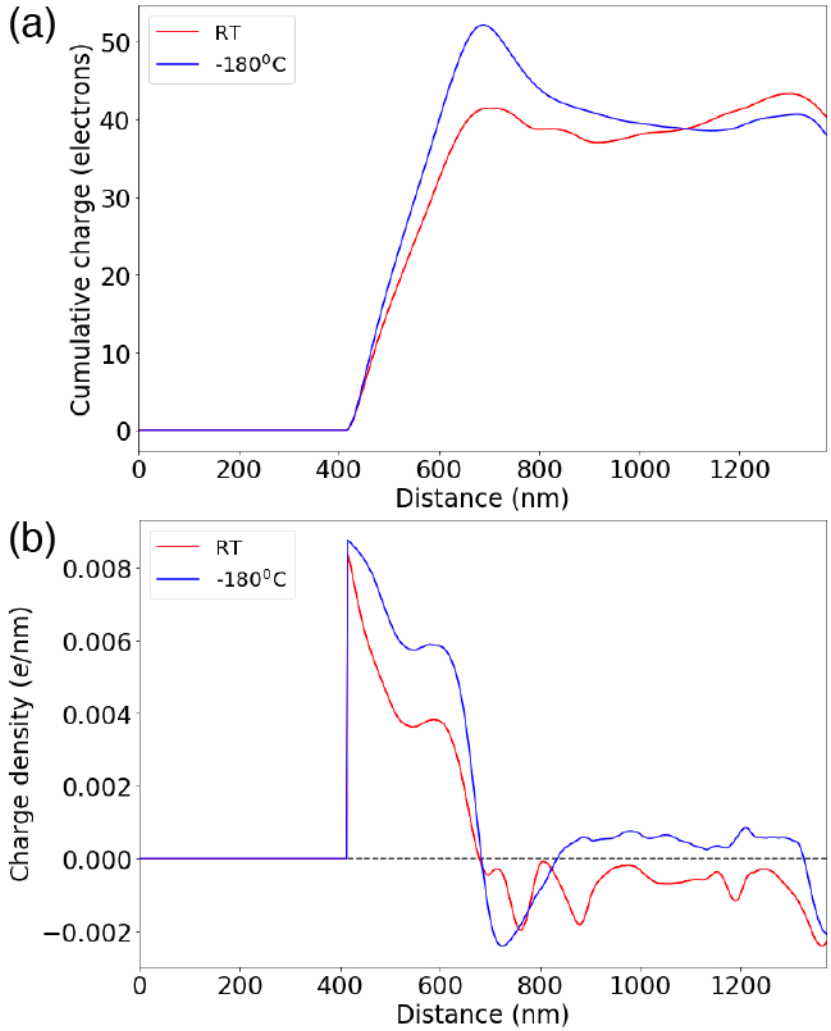

Fig. 8.13 (a) Cumulative charge profiles along the needle axis and (b) line profiles of the projected charge density along the needle axis (labelled by an arrow in Figs. 8.12a-b) extracted from the reconstructed projected charge density distributions shown in Figs. 8.12a-b. The integration region in (a) starts from the top of the images shown in Figs. 8.12a-b.

8.6.2 Influence of plasma cleaning

In order to assess the reproducibility of the effects described above, the charge state on the needle was checked after several days. Unexpectedly, when using parallel illumination with a dose rate of approximately 2.6 $e/\text{Å}^2/\text{s}$, electron-beam-induced charging was found to be negligible, as shown in Fig. 8.14. This observation suggests that exposure to ambient atmosphere can change the surface state and therefore the charging behaviour of a sample. No dependence on either dose rate or dose was found (not shown).

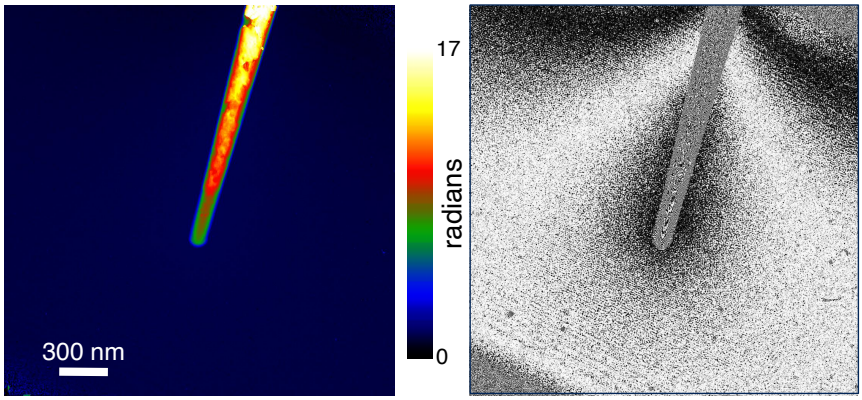

Fig. 8.14 Electron-beam-induced charging of the third needle measured after exposure to air, showing a phase image (left) and a corresponding phase contour map (right) of the third needle illuminated by 300 kV electrons at a dose rate of 2.6 $e/\text{Å}^2/\text{s}$. The phase contour spacing is $\frac{2\pi}{12}$ radians.

An attempt was made to change the surface state of the needle using plasma cleaning (Fischione Instruments, model 1020) with oxygen at a pressure of 10^{-1} mbar), which is expected to remove C, H and O contamination from the specimen surface. Fig. 8.15 shows measurements of electron-beam-induced charging of the needle after one minute of plasma cleaning. When using the same electron beam illumination conditions and microscope parameters as before, it can be seen that the charging behaviour of the needle recovered and is consistent with the results presented above (*e.g.*, in Section 8.6.1). There is also no dependence of electron-beam-induced charging on dose rate (Fig. 8.15) or total dose (not shown).

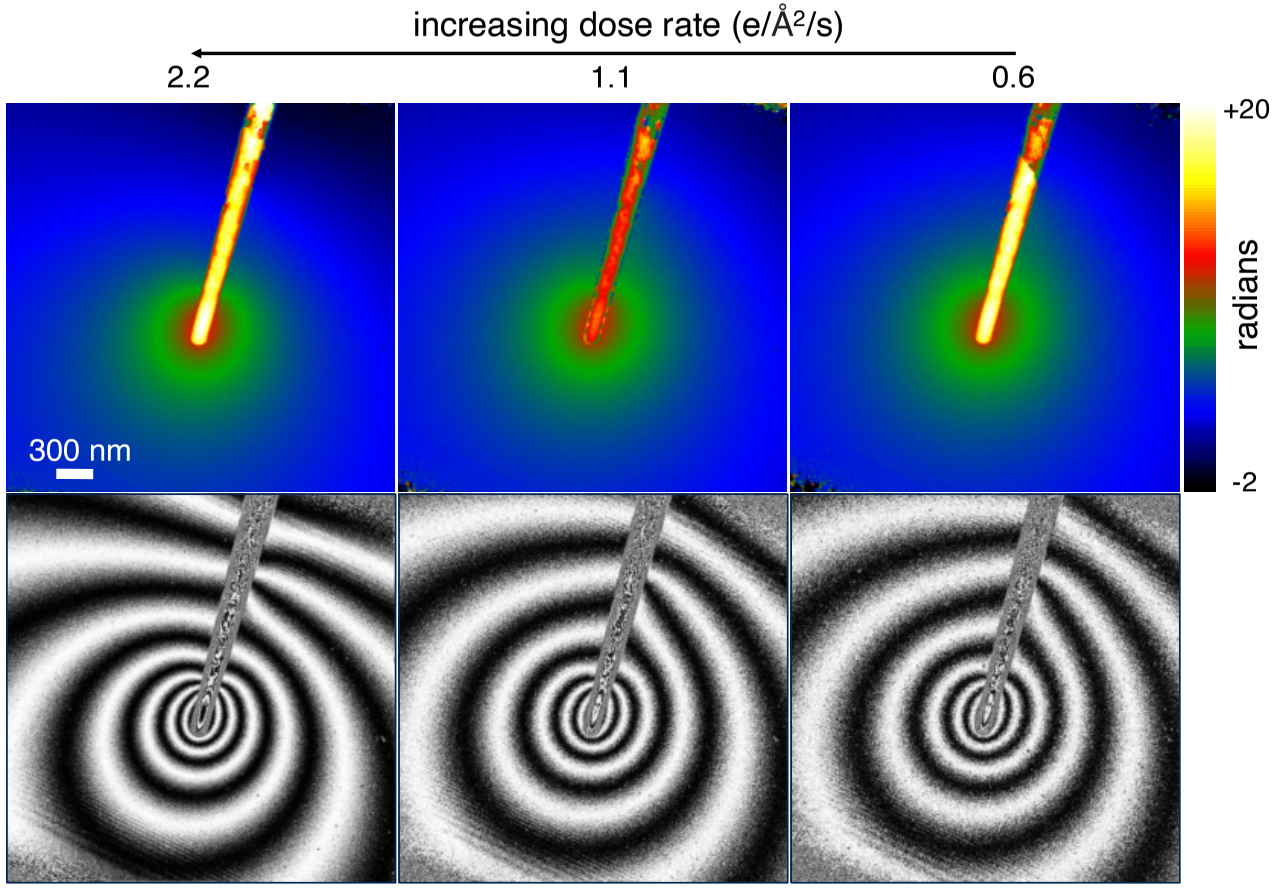

Fig. 8.15 Electron-beam-induced charging of the third needle measured at 300 kV after one minute of plasma cleaning. Phase images (upper row) and corresponding phase contour maps (lower row) are shown for different dose rates (denoted by the number above each image). The phase contour spacing is $\frac{2\pi}{4}$ radians.

8.6.3 Accelerating voltage dependence

In order to assess the dependence of electron-beam-induced charging on the energy of the incident electron beam, the accelerating voltage of microscope was switched from 300 to 60 kV without taking the sample out of the microscope. Fig. 8.16 shows the results of electron-beam-induced charging measurements of the third needle at 60 kV [1]. Just as at 300 kV, there was almost no dependence on dose rate or on dose (not shown).

The MBIR approach was used to reconstruct the projected charge density from the results. The phase inside the needle was not used, as the MIP contribution to the phase could not be removed. Fig. 8.17 shows the reconstructed projected charge density distributions. Before plasma cleaning, there was almost no charge inside the needle (Fig. 8.17a), with the cumulative charge profile (red in Fig. 8.18a) and charge profile (red in Fig. 8.18b) showing that the needle was slightly homogeneously charged, with a total charge inside the FOV of approximately 3 electrons. After plasma cleaning, the needle was positively charged at its apex and negatively charged in its conductive base, both at 300 kV (Fig. 8.17b) and at 60 kV (Fig. 8.17c). The positive charge extended over a greater distance when the needle was illuminated with 60 kV electrons than with 300 kV electrons. The measured charge profiles (blue for 300 kV and green for 60 kV in Fig. 8.18b) show that the needle was negatively charged up to a distance of 188 and 194 nm from the very apex at 300 and 60 kV, respectively, with a minimum charge density of -0.01 and -0.005 e/nm, respectively. Fig. 8.18a shows corresponding cumulative charge profiles. The total positive charge at the apex of the needle corresponds to a deficit of 37 and 48 electrons for 300 and 60 kV, respectively, suggesting that a lower primary electron energy results in the needle becoming more strongly charged in both the insulating apex and the conductive base. This is expected, as the secondary electron emission yield is inversely proportional to the primary electron energy [139, 24]. More data recorded at different accelerating voltages would be helpful for better comparisons with theory. Oscillations in both cumulative charge profiles may be associated with the triangular-shaped Cr diffusion area.

[1] The direct electron counting Gatan K2-IS camera cannot be used at 60 kV. The Gatan Ultrascan camera was used instead.

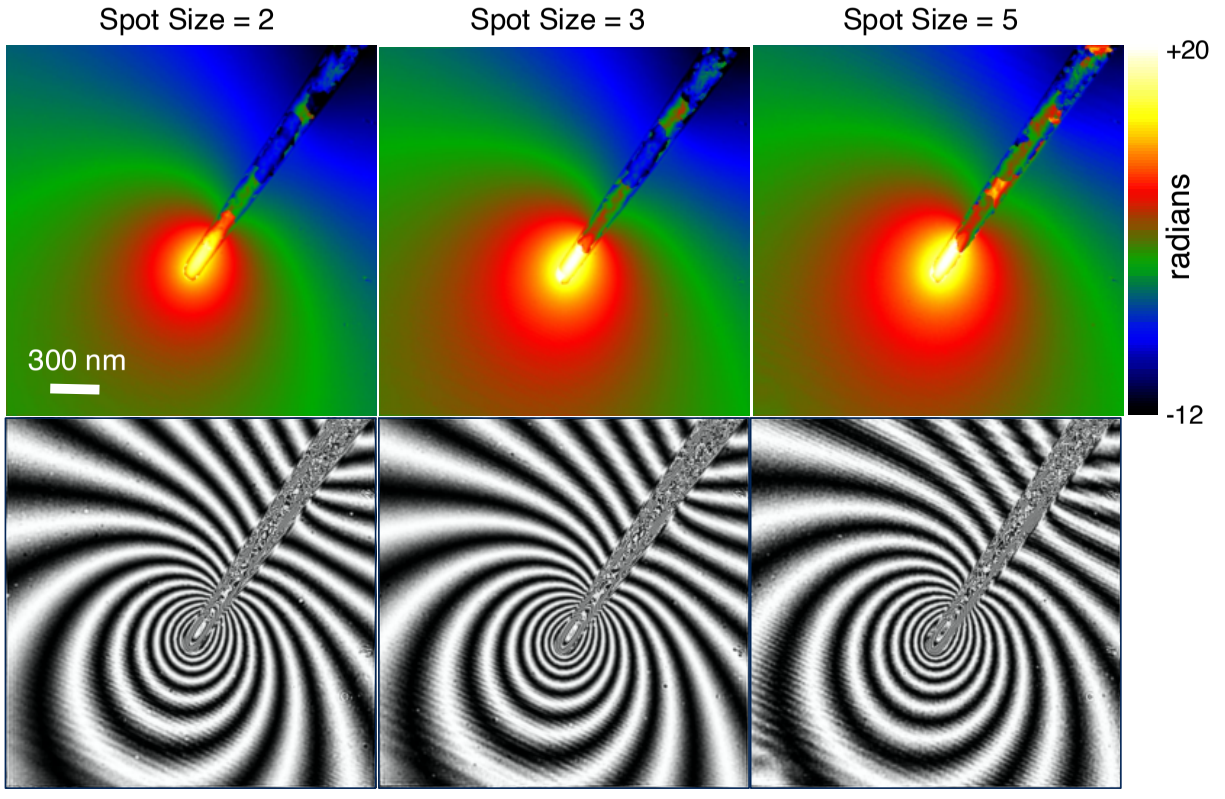

Fig. 8.16 Electron-beam-induced charging of the third needle measured at an accelerating voltage of 60 kV. Phase image (upper row) and corresponding phase contour maps (lower row) are shown for different dose rates. From left to right, the spot size is 2, 3 and 5. The phase contour spacing is $\frac{2\pi}{4}$ radians.

Fig. 8.17 Results of model-based iterative reconstruction of the projected charge density for three cases: (a) before plasma cleaning at 300 kV; (b) after plasma cleaning at 300 kV; (c) after plasma cleaning at 60 kV. The pixel sizes at 60 kV and 300 kV are 4.4 and 4.7 nm, respectively.

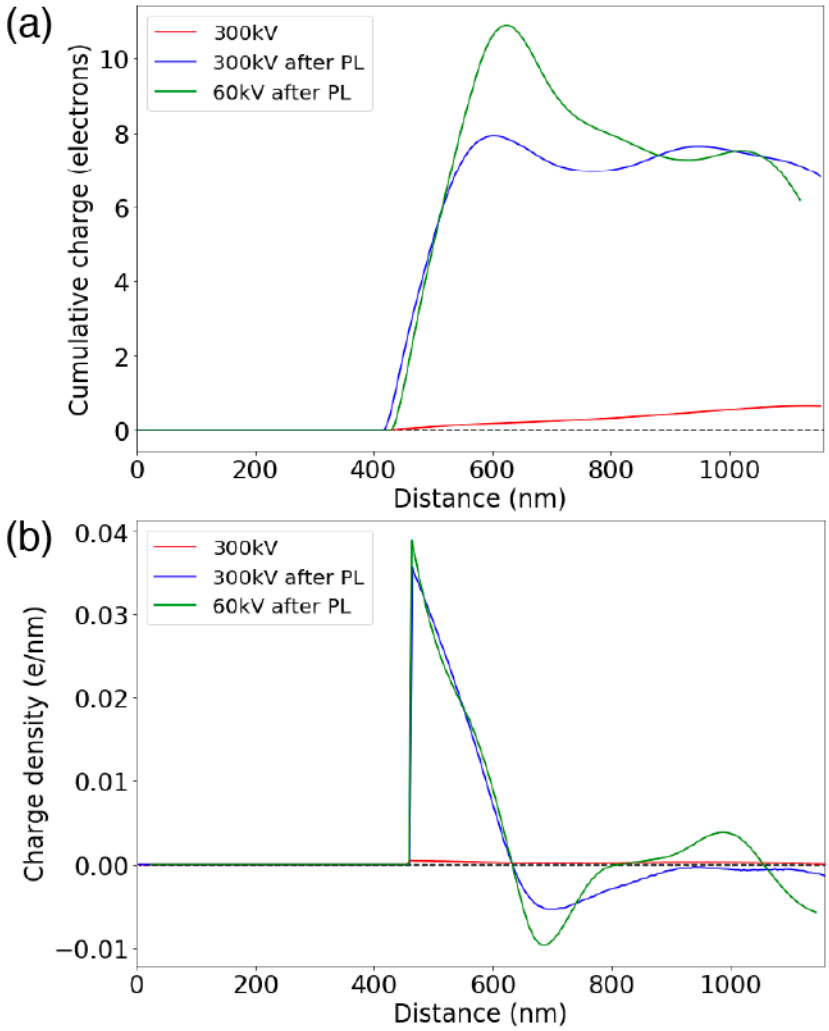

Fig. 8.18 (a) Cumulative charge profiles along the needle axis and (b) line profiles of the projected charge density along the needle axis (labelled by arrows in Figs. 8.17a-c) extracted from the reconstructed projected charge density distributions shown in Figs. 8.17a-c. The integration region in (a) starts from the top of the images shown in Figs. 8.17a-c.

8.7 Summary and conclusions

Electron-beam-induced charging in three similar needle-shaped specimens has been studied systematically using off-axis electron holography. The needles each comprise an insulating Al_2O_3 apex and a conductive Cr_2AlC base. The apex of each needle typically charges as a result of secondary electron emission during illumination with high-energy electrons in the TEM. The dependence of charging on parameters that include dose rate, total dose, primary electron energy, temperature and applied bias voltage have been studied systematically. The analytical model-dependent and model-independent approaches (Chapter 2), as well as the model-based iterative reconstruction approach (Chapter 5) have been used to quantitatively evaluate the projected charge density induced by electron beam illumination. The surface state of the specimen is found to play an important role in the charging process. Improved control or knowledge of the surface state may therefore be of great help in the future to understand and interpret charging behaviour resulting from high-energy electron illumination. Theoretical models that are able to include local variations in (surface) band structure, the presence of junctions (*e.g.*, metal/semiconductor/insulator or metal/insulator/semiconductor), secondary electron emission, defects and surface states, in comparison with further systematic experimental measurements performed on ultra-clean and damage-free specimens, are necessary to understand the underlying physics of electron-beam-induced charging fully.

Chapter 9

Discussion

In this thesis, three approaches based on off-axis electron holography for the measurement of charge, electric field and electrostatic potential with high spatial resolution, both in projection and in three dimensions, have been developed and applied to the characterisation of a variety of needle-shaped specimens.

9.1 Applicability of approaches

The three approaches that have been investigated are: i) an analytical model-dependent approach (Section 4.2.2), in which a mathematical model is used to describe the charge density and phase shift; ii) a model-independent approach (Section 4.2.1), which is based on the application of a Laplacian operator to a recorded phase image; iii) a numerical model-based iterative reconstruction approach (Chapter 5), in which the charge density is varied in a forward model that is used to simulate phase images until a best match to experimental measurements is obtained.

The analytical model-dependent approach (Section 4.2.2) relies on access to an analytical solution for the charge density and phase distribution for the experimental specimen geometry and requires the effect of the perturbed reference wave to be included in the model. The model-independent approach (Section 4.2.1) is the most direct and unbiased approach for retrieving the projected charge density from a holographic phase image and is insensitive to the presence of both a perturbed reference wave and charges outside the field of view. However, the measured charge density can be noisy (since the approach relies on the evaluation of second-order derivatives), complicating reconstruction of the three-dimensional charge density from a tomographic tilt series of two-dimensional projected charge density measurements. In the model-based iterative reconstruction approach (Chapter 5), a forward model approximates each charged voxel as a homogeneously charged sphere and its mirror charge. It can be used

to incorporate *a priori* knowledge about the specimen and the experimental setup through the use of masks (Section 5.4.1), regularisation parameters and other physical constraints, resulting in the reconstruction of images that have lower noise, but requiring care in the selection of input parameters to avoid the introduction of artefacts (Section 5.4.2). Boundary buffer pixel regions can be used to take into account the presence of charges outside the field of view and the effect of a perturbed reference wave (Section 5.4.4). Furthermore, a confidence mask can be used to specify regions of phase images that contain untrustworthy information (Section 5.4.3).

The three approaches have been used to study experimental phase images of electrically-biased needle-shaped specimens, such as a LaB_6 field emitter (Chapters 4 and 5). They have been shown to provide consistent results for charge density measurements. One or more line charges have been used as the basis for simple models for the charge density in these specimens in the analytical model-dependent approach (Chapters 4, 6 and 8). Projected charge density distributions retrieved using both from the model-independent approach (*e.g.*, Figs. 4.6a and 4.6b) and the model-based iterative reconstruction approach (*e.g.*, Figs. 5.14 and 6.15) show that most of the charge in a needle-shaped specimen is typically located close to its outer surface, with the greatest charge accumulation at its apex. The charge density obtained using the model-based iterative reconstruction approach has much less noise than that obtained using the model-independent approach. The three-dimensional charge density can in principle be reconstructed using each approach, either by applying a standard backprojection-based tomographic reconstruction algorithm to the projected charge density distributions measured as a function of specimen tilt angle or more directly by using the model-based iterative reconstruction approach. Both simulated phase images (Section 5.5) and experimental phase images (Chapter 7) were used to show the advantage of using the model-based iterative reconstruction approach, in which *a priori* information can be specified about the boundary of the object when reconstructing a three-dimensional charge density (Section 5.5, Figs. 5.15 and 5.16). In addition, boundary buffer pixel regions can be used to take into account the presence of charges outside the field of view and the effect of a perturbed reference wave (Sections 5.4.4 and 5.5.2, Fig. 5.18).

The uniqueness of the reconstructed charge density is guaranteed in a mathematical sense, but not in a physical sense (Chapter 5), as different charge density distributions inside an object can result in the same electrostatic potential and phase distribution outside it. Subtraction of the mean inner potential contribution to the phase makes the problem less under-determined and improves the uniqueness of the solution. In the future, such reconstructions may require the use of a more robust regularisator (instead of the simple Euclidean norm used in this thesis), which searches for a minimum in total electrostatic

potential energy or makes use of other physical constraints. Nevertheless, the uniqueness of the reconstructed phase (*i.e.*, the projected potential and the projected in-plane electric field) is guaranteed, even if the charge density in the specimen is not reconstructed accurately. (See examples in Chapters 5-8.)

9.2 Significance of experimental measurements

In this thesis, the significance of a correct choice of experimental parameters when applying the three approaches has been highlighted.

In the analytical model-dependent approach (Section 4.2.2), a careful choice of specimen geometry is required to allow the creation of a model that can be used to solve the Laplace equation. For a the hemi-ellipsoidal needle-shaped specimen (*i.e.*, the LaB_6 field emitter studied in Chapter 4), the shape of the needle is required to specify the major and minor semi-axis in the analytical model [93, 41]. For a needle-shaped specimen that has a sharply-terminated end (*e.g.*, the W_5O_{14} nanowire studied in Chapter 6), a knowledge of the length, width and local curvature at the very apex is crucial to assess how closely it can be approximated by a standard ellipsoidal geometry. (See Chapter 6 and Appendix C.) In addition, the orientation of the biprism and the interference distance have to be measured correctly to take the effect of the perturbed reference wave into account. When such parameters are measured independently, the fitting of an analytical solution to an experimental phase image can be reduced to finding a single parameter, such as the constant K in the expression for the line charge density. (See Chapter 4 and Appendix B.)

In the model-independent approach described in Section 4.2.1, access to the phase inside the specimen is required, resulting in the need to remove the mean inner potential contribution to the phase and to minimise the influence of dynamical diffraction and contamination on recorded phase images. In addition, the signal-to-noise ratio in the measured phase should be as high as possible. It should be noted that the mean inner potential contribution to the phase does not affect a measurement of the *total* cumulative charge, as its net contribution across an entire specimen is zero. Optimisation of the phase resolution is important for evaluation of the Laplacian operator using a second-order derivative and also for standard back-projection-based tomography of the three-dimensional charge density from a tilt series of projected charge density distributions.

In the model-based iterative reconstruction approach (Chapter 5), more experimental parameters need to be determined carefully. The shape of the specimen is used to create a mask to define where charges can be located and has to be measured correctly. For three-dimensional reconstruction, the shape of the specimen has to be reconstructed from a

standard tomographic tilt series of images, ideally without artefacts such as those from the missing wedge. The accuracy of the three-dimensional mask has a strong influence on the reconstructed charge density. (See Section 5.5.) A confidence mask can often be determined directly from the experimental phase images to mark pixels that are not fully trustworthy as a result of the presence of effects such as contamination, diffraction contrast and X-ray spikes. Issues related to the alignment of an entire tilt series and to the determination of the tilt axis and individual tilt angles are also important. Furthermore, the signal-to-noise ratio in experimental phase images should be optimised, as a result of the sensitivity of the approach to noise, as it involves searching for the least-squared norm minimum between calculated and experimental phase images.

9.3 Potential for use in a combined APT-TEM instrument

The possibility of reconstructing the three-dimensional electric field of an electrically-biased needle-shaped specimen (Chapter 7) offers the chance to improve the reconstruction of three-dimensional atomic positions in an APT experiment. A direct measurement of the three-dimensional electric field around an atom probe needle during field evaporation would provide a significant benefit for the reconstruction of atom positions. A knowledge of the electric field around an atom probe needle can then serve as the basis of aberration correction for reconstruction [140].

A correlative experiment could involve taking an atom probe needle out repeatedly to map its three-dimensional electric field at different stages of field evaporation, in order to obtain several snapshots of the evolution of the electric field during the evaporation process. In such an experiment, the atom probe needle must withstand repeated (cryo) transfer between the APT and the TEM. Specimen failure (rupture, fracture, oxidation and contamination) can happen. At the least, the three-dimensional electric field at the initial and final stages of an atom probe experiment can be measured.

A physically-integrated APT and TEM is proposed in the TOMO project within the framework of the BMBF Roadmap 2.0 in Forschungszentrum Jülich. It aims to combine the two techniques in a single instrument, so that APT and TEM (including the techniques of off-axis electron holography and/or DPC imaging) can be performed sequentially or simultaneously. It is then no longer necessary to transfer the needle between the APT and the TEM. On the assumption of rotational symmetry, in order to reduce the acquisition time and the complexity of the experiment, the three-dimensional electric field can in principle be retrieved from a single projection.

In addition, the influence of the electrical conductivity of the needle on field evaporation and projection to the detector can be assessed directly. Whether electron-beam-induced charging affects needles fabricated from particular materials remains to be answered by using such an instrument. Aberrations that affect current atom probe experiments could be compensated directly by using measurements of the three-dimensional electric field of the needle. Questions regarding the sequence of electric field mapping and field evaporation experiments, the influence of tilting during experiments, the influence of "switch-on" and "switch-off" bias voltage, as well as the influence of information inside the specimen, remain open. Comparisons between parallel-beam-based off-axis electron holography and scanning-beam-based DPC imaging for electric field mapping have to be evaluated further in terms of acquisition time, electric field sensitivity, signal-to-noise ratio and effectiveness of 3D reconstruction.

9.4 Conclusions in the context of the SIMDALEE2 project

It has been demonstrated in this thesis that charge density and electric field can be measured quantitatively both in projection and in three dimensions, especially for studies of needle-shaped specimens (Chapters 4-8, in particular Chapter 6 for the study of field emission from a W_5O_{14} nanowire). The techniques that have been developed and applied in this thesis may serve as the basis for the evaluation of the field emission performance of field emitters before and during field emission to provide insight into the factors that affect their properties, such as their spatial and temporal coherence and brightness, as well as to understand the fundamental mechanism of field emission. The relationship between the physical shape of a field emitter and its field emission performance can be correlated (see Chapter 6). Such an understanding can help in the search for nano-sized or even atomic-sized field emitters, which can be used in instruments such as the NFESEM [85].

Interactions between low energy electrons and specimens, including biological materials, insulators and dielectric materials, are crucial for understanding image contrast and spatial resolution in the NFESEM, as well as for many other practical applications [141, 142]. The systematic observation of electron-beam-induced charging (Chapter 8) may serve as a fundamental basis for understanding the behaviour of materials (*e.g.*, PMMA as a lithography resist and vitrified ice for biological specimens in cryo EM) that are illuminated by both low and high energy electrons. It can also provide a deep understanding of the fundamental basis of the generation and emission of secondary electrons during electron illumination.

Chapter 10

Conclusions and outlook

In this thesis, the measurement of charge, electric field and electrostatic potential with high spatial resolution has been investigated using off-axis electron holography, both in projection and in three dimensions. Three approaches have been used to retrieve charge density from holographic phase images, including two existing approaches (an analytical model-dependent approach and a model-independent approach; Chapter 2) and a newly-developed model-based iterative reconstruction approach (Chapter 5). The advantages and disadvantages of each approach have been reviewed and evaluated from both a theoretical perspective (Chapter 2) and a practical perspective (Chapter 4). They have also been illustrated through experimental studies of samples that include a LaB_6 field emitter (Chapter 4) and a W_5O_{14} nanowire (Chapter 6). The newly-developed model-based iterative reconstruction approach has the following advantages: i) it allows the incorporation of *a priori* knowledge through the use of masks (Section 5.4.1), regularisation parameters and other physical constraints, resulting in lower noise in reconstructions but requiring care in the selection of parameters to avoid the introduction of artefacts (Section 5.4.2); ii) it allows the use of boundary buffer pixel regions to take into account the presence of charges outside the field of view and the effect of a perturbed reference wave (Section 5.4.4); iii) it allows the use of a confidence mask that can avoid artefacts originating from regions of phase images that contain untrustworthy information (Section 5.4.3); iv) it allows the capability for the measurement of three-dimensional charge density from tomographic tilt series of phase images without problems associated with missing wedge artefacts (Chapter 7).

In Chapter 6, the charge density was measured in a W_5O_{14} nanowire, which had a sharply-terminated apex and a quasi-rectangular cross-section. An accumulation of charge was found to be present at the apex of the nanowire, both before and during field emission. The charge density in the shank of the nanowire could be described using a linear line charge density approximation.

In Chapter 7, the three-dimensional charge density, electric field and electrostatic potential of an electrically-biased carbon fibre needle were mapped using the developed model-based iterative reconstruction approach (Chapter 5). The reconstructed charge density was found to be located primarily at the apex and on the outer surface of the needle, as expected from classical electrostatics. The cumulative charge was observed to display a linear behaviour, indicating an approximately constant line charge density along the needle axis. The slight asymmetry in the measured charge density could be ascribed to local curvature of the needle or artefacts of the reconstruction. The algorithm was found to be robust to many of the artefacts that affect conventional backprojection-based tomographic reconstruction approaches and was able to retrieve details of the charge density regardless of the symmetry of the specimen. The inferred three-dimensional electric field and electrostatic potential were found to have almost rotational symmetry about the needle axis. The electric field was greatest close to the apex region (outside the needle), where it had a maximum value of 0.25 GV/m with a bias voltage of 40 V applied to the needle at a distance of 4.5 μm to the counter-electrode.

In Chapter 8, electron-beam-induced charging in three similar needle-shaped specimen has been investigated systematically using off-axis electron holography. The needles each comprised an insulating Al_2O_3 apex and a conductive Cr_2AlC base. The apex of each needle typically charged due to secondary electron emission upon electron beam illumination in the TEM. The dependence of charging on dose rate, total dose, primary electron energy, temperature and applied bias voltage were studied. The analytical model-dependent, model-independent approaches and the model-based iterative reconstruction approach were used to quantitatively evaluate charges induced by electron beam illumination. The state of the specimen surface was found to play a vital role in the charging process. In the future, improved control or knowledge of the surface state may therefore be of great help to understand charging of samples due to low and high energy electron illumination.

Future work can concentrate on areas that include: i) implementation of a physical regularisator into the model-based iterative reconstruction algorithm, such as minimisation of the total electrostatic potential energy in the regularisation term; ii) assessment of the uniqueness of the inverse problem (from the electron holographic phase to the charge, the electric field and the electrostatic potential); iii) comparison between the reconstructed three-dimensional measurements of charge, electric field and electrostatic potential with finite element simulations; iv) measurements of field enhancement factor and field emission current in nano-objects of arbitrary geometry before and during field emission; v) examinations of field emitters that have ultra-clean specimen surfaces, for example using a Ferrovac ultra-high-vacuum transfer system; vi) systematic electron-beam-induced charging experiments performed on

ultra-clean and damage-free specimens with electrical different conductivities (*e.g.*, MgO nanocubes) in an ultra-high-vacuum TEM column, as well as coincidence measurements including secondary electron imaging/spectroscopy and electron energy-loss spectroscopy, as a function of specimen tilt, specimen orientation and shape (facets), electron dose, dose rate, temperature, bias voltage and primary electron energy in both parallel and scanning beam settings, and further as a function of time; vii) the development of theoretical understanding of the generation and emission of secondary electrons, in particular in association with surface band bending and defects.

Bibliography

[1] L Solymar, D Walsh, and RRA Syms. *Electrical properties of materials*. Oxford University Press, 2014.

[2] V Ravikumar, RP Rodrigues, and VP Dravid. Direct imaging of spatially varying potential and charge across internal interfaces in solids. *Physical Review Letters*, 75(22):4063, 1995.

[3] EY Tsymbal and H Kohlstedt. Tunneling across a ferroelectric. *Science*, 313(5784):181–183, 2006.

[4] Z Gan, M Gu, J Tang, C Wang, Y He, KL Wang, C Wang, DJ Smith, and MR McCartney. pping of charge distribution during lithiation of Ge nanowires using off-axis electron holography. *Nano Letters*, 16(6):3748–3753, 2016.

[5] T Hirayama, Y Aizawa, K Yamamoto, T Sato, H Murata, R Yoshida, C AJ Fisher, T Kato, and Y Iriyama. Advanced electron holography techniques for in situ observation of solid-state lithium ion conductors. *Ultramicroscopy*, 173:64–70, 2017.

[6] S Yazdi, T Kasama, M Beleggia, MS Yekta, DW McComb, AC Twitchett-Harrison, and RE Dunin-Borkowski. Towards quantitative electrostatic potential mapping of working semiconductor devices using off-axis electron holography. *Ultramicroscopy*, 152:10–20, 2015.

[7] H Lee, N Campbell, J Lee, TJ Asel, TR Paudel, H Zhou, JW Lee, B Noesges, J Seo, B Park, LJ Brillson, SH Oh, EY Tsymbal, MS Rzchowski, and CB Eom. Direct observation of a two-dimensional hole gas at oxide interfaces. *Nature Materials*, 17(231-236), 2018.

[8] DJL Brett, A Atkinson, NP Brandon, and SJ Skinner. Intermediate temperature solid oxide fuel cells. *Chemical Society Reviews*, 37(8):1568–1578, 2008.

[9] DY Wang and AS Nowick. The "grain-boundary effect" in doped ceria solid electrolytes. *Journal of Solid State Chemistry*, 35(3):325–333, 1980.

[10] J Maier. Nanoionics: ionic charge carriers in small systems. *Physical Chemistry Chemical Physics*, 11(17):3011–3022, 2009.

[11] D Cooper, R Truche, AC Twitchett-Harrison, RE Dunin-Borkowski, and PA Midgley. Quantitative off-axis electron holography of GaAs *p-n* junctions prepared by focused ion beam milling. *Journal of Microscopy*, 233(1):102–113, 2009.

[12] D Cooper, C Ailliot, J Barnes, J Hartmann, P Salles, G Benassayag, and RE Dunin-Borkowski. Dopant profiling of focused ion beam milled semiconductors using off-axis electron holography; reducing artifacts, extending detection limits and reducing the effects of gallium implantation. *Ultramicroscopy*, 110(5):383–389, 2010.

[13] N Shibata, SD Findlay, H Sasaki, T Matsumoto, H Sawada, Y Kohno, S Otomo, R Minato, and Y Ikuhara. Imaging of built-in electric field at a *p-n* junction by scanning transmission electron microscopy. *Scientific Reports*, 5:10040, 2015.

[14] K Song, S Ryu, H Lee, TR Paudel, CT Koch, B Park, JK Lee, S Choi, Y Kim, JC Kim, Y Jeong, MS Rzchowski, EY Tsymbal, CB Eom, and SH Oh. Direct imaging of the electron liquid at oxide interfaces. *Nature Nanotechnology*, 13(3):198, 2018.

[15] V Ravikumar, RP Rodrigues, and VP Dravid. Space-charge distribution across internal interfaces in electroceramics using electron holography: I. pristine grain boundaries. *Journal of the American Ceramic Society*, 80(5):1117–1130, 1997.

[16] V Ravikumar, RP Rodrigues, and VP Dravid. Space-charge distribution across internal interfaces in electroceramics using electron holography: II. doped grain boundaries. *Journal of the American Ceramic Society*, 80(5):1131–1138, 1997.

[17] Z Mao, RE Dunin-Borkowski, C Boothroyd, and KM Knowles. Direct measurement and interpretation of electrostatic potentials at 24°[001] tilt boundaries in undoped and niobium-doped strontium titanate bicrystals. *Journal of the American Ceramic Society*, 81(11):2917–2926, 1998.

[18] X Xu, S Haile, and C Phatak. *In-situ* electron holography study of grain boundaries in cerium oxide. *Microscopy and Microanalysis*, 24(S1):1466–1467, 2018.

[19] MA Schofield, M Beleggia, Y Zhu, K Guth, and C Jooss. Direct evidence for negative grain boundary potential in Ca-doped and undoped $YBa_2Cu_3O_{7-x}$. *Physical Review Letters*, 92(19):195502, 2004.

[20] RE Dunin-Borkowski, WO Saxton, and WM Stobbs. The electrostatic contribution to the forward-scattering potential at a space charge layer in high-energy electron diffraction: I. theory neglecting the effects of fringing fields. *Acta Crystallographica Section A*, 52(5):705–711, 1996.

[21] RE Dunin-Borkowski and WO Saxton. The electrostatic contribution to the forward-scattering potential at a space charge layer in high-energy electron diffraction: II. fringing fields. *Acta Crystallographica Section A*, 53(2):242–250, 1997.

[22] DB Dove. Image contrasts in thin carbon films observed by shadow electron microscopy. *Journal of Applied Physics*, 35(5):1652–1653, 1964.

[23] GH Curtis and RP Ferrier. The electric charging of electron-microscope specimens. *Journal of Physics D: Applied Physics*, 2(7):1035, 1969.

[24] L Reimer. *Scanning electron microscopy: physics of image formation and microanalysis*. Springer, 2013.

[25] CJ Russo and R Henderson. Charge accumulation in electron cryomicroscopy. *Ultramicroscopy*, 187:43–49, 2018.

[26] CJ Russo and R Henderson. Microscopic charge fluctuations cause minimal contrast loss in cryoEM. *Ultramicroscopy*, 187:56–63, 2018.

[27] M Malac, M Beleggia, M Kawasaki, P Li, and RF Egerton. Convenient contrast enhancement by a hole-free phase plate. *Ultramicroscopy*, 118:77–89, 2012.

[28] J Berriman and KR Leonard. Methods for specimen thickness determination in electron microscopy: II. changes in thickness with dose. *Ultramicroscopy*, 19(4):349–366, 1986.

[29] J Brink, MB Sherman, J Berriman, and W Chiu. Evaluation of charging on macromolecules in electron cryomicroscopy. *Ultramicroscopy*, 72(1-2):41–52, 1998.

[30] KH Downing, MR McCartney, and RM Glaeser. Experimental characterization and mitigation of specimen charging on thin films with one conducting layer. *Microscopy and Microanalysis*, 10(6):783–789, 2004.

[31] J Cazaux. Some considerations on the electric field induced in insulators by electron bombardment. *Journal of Applied Physics*, 59(5):1418–1430, 1986.

[32] J Cazaux. Correlations between ionization radiation damage and charging effects in transmission electron microscopy. *Ultramicroscopy*, 60(3):411–425, 1995.

[33] J Cazaux. Some considerations on the secondary electron emission, δ, from e-irradiated insulators. *Journal of Applied Physics*, 85(2):1137–1147, 1999.

[34] J Cazaux. e-induced secondary electron emission yield of insulators and charging effects. *Nuclear Instruments and Methods in Physics Research Section B: Beam Interactions with Materials and Atoms*, 244(2):307–322, 2006.

[35] J Cazaux. Secondary electron emission and charging mechanisms in auger electron spectroscopy and related e-beam techniques. *Journal of Electron Spectroscopy and Related Phenomena*, 176(1-3):58–79, 2010.

[36] K Danov, R Danev, and K Nagayama. Electric charging of thin films measured using the contrast transfer function. *Ultramicroscopy*, 87:45–54, 2001.

[37] K Danov, R Danev, and K Nagayama. Reconstruction of the electric charge density in thin films from the contrast transfer function measurements. *Ultramicroscopy*, 90:85–95, 2002.

[38] BG Frost. An electron holographic study of electric charging and electric charge distributions. *Ultramicroscopy*, 75(2):105–113, 1998.

[39] BG Frost and E Völkl. On the reliability of quantitative phase measurements by low magnification off-axis image plane electron holography. *Ultramicroscopy*, 72(3-4):101–107, 1998.

[40] C Gatel, A Lubk, G Pozzi, E Snoeck, and MJ Hÿtch. Counting elementary charges on nanoparticles by electron holography. *Physical Review Letters*, 111(2):025501, 2013.

[41] M Beleggia, LC Gontard, and RE Dunin-Borkowski. Local charge measurement using off-axis electron holography. *Journal of Physics D: Applied Physics*, 49(29):294003, 2016.

[42] DB Williams and CB Carter. *Transmission electron microscopy: A textbook for material science*. Springer, 1998.

[43] RH Fowler and L Nordheim. Electron emission in intense electric fields. *Proceedings of the Royal Society of London. Series A*, 119(781):173–181, 1928.

[44] PG Collins and A Zettl. Unique characteristics of cold cathode carbon-nanotube-matrix field emitters. *Physical Review B*, 55:9391–9399, Apr 1997.

[45] RB Sharma, VN Tondare, DS Joag, A Govindaraj, and CNR Rao. Field emission from carbon nanotubes grown on a tungsten tip. *Chemical Physics Letters*, 344(3-4):283–286, 2001.

[46] J Cumings, A Zettl, MR McCartney, and JCH Spence. Electron holography of field-emitting carbon nanotubes. *Physical Review Letters*, 88(5):056804, 2002.

[47] F Houdellier, A Masseboeuf, M Monthioux, and MJ Hÿtch. New carbon cone nanotip for use in a highly coherent cold field emission electron microscope. *Carbon*, 50(5):2037–2044, 2012.

[48] L de Knoop, F Houdellier, C Gatel, A Masseboeuf, M Monthioux, and M Hÿtch. Determining the work function of a carbon-cone cold-field emitter by in situ electron holography. *Micron*, 63:2–8, 2014.

[49] F Houdellier, L de Knoop, C Gatel, A Masseboeuf, S Mamishin, Y Taniguchi, M Delmas, M Monthioux, MJ Hÿtch, and E Snoeck. Development of TEM and SEM high brightness electron guns using cold-field emission from a carbon nanotip. *Ultramicroscopy*, 151:107–115, 2015.

[50] JJ Kim, D Shindo, Y Murakami, L Xia, Wand Chou, and Y Chueh. Direct observation of field emission in a single $TaSi_2$ nanowire. *Nano Letters*, 7(8):2243–2247, 2007.

[51] T Oikawa, JJ Kim, T Tomita, H Soon Park, and D Shindo. Measurement of electric potential distributions around FEG-emitters by electron holography. *Journal of Electron Microscopy*, 56(5):171–175, 2007.

[52] EW Müller, JA Panitz, and SB McLane. The atom-probe field ion microscope. *Review of Scientific Instruments*, 39(1):83–86, 1968.

[53] TF Kelly and DJ Larson. Atom probe tomography 2012. *Annual Review of Materials Research*, 42:1–31, 2012.

[54] F Vurpillot, B Gault, BP Geiser, and DJ Larson. Reconstructing atom probe data: A review. *Ultramicroscopy*, 132:19–30, 2013.

[55] EA Marquis and F Vurpillot. Chromatic aberrations in the field evaporation behavior of small precipitates. *Microscopy and Microanalysis*, 14(6):561–570, 2008.

[56] MK Miller. The effects of local magnification and trajectory aberrations on atom probe analysis. *Le Journal de Physique Colloques*, 48(C6):C6–565, 1987.

[57] MK Miller and MG Hetherington. Local magnification effects in the atom probe. *Surface Science*, 246(1-3):442–449, 1991.

[58] B Gault, ST Loi, VJ Araullo-Peters, LT Stephenson, MP Moody, SL Shrestha, Ross KW Marceau, L Yao, JM Cairney, and SP Ringer. Dynamic reconstruction for atom probe tomography. *Ultramicroscopy*, 111(11):1619–1624, 2011.

[59] F Vurpillot and C Oberdorfer. Modeling atom probe tomography: A review. *Ultramicroscopy*, 159:202–216, 2015.

[60] M Herbig, D Raabe, YJ Li, P Choi, and S Zaefferer, Sand Goto. Atomic-scale quantification of grain boundary segregation in nanocrystalline material. *Physical Review Letters*, 112(12):126103, 2014.

[61] M Herbig, P Choi, and D Raabe. Combining structural and chemical information at the nanometer scale by correlative transmission electron microscopy and atom probe tomography. *Ultramicroscopy*, 153:32–39, 2015.

[62] G Matteucci, GF Missiroli, and G Pozzi. Electron holography of long-range electrostatic fields. In Peter W. Hawkes, editor, *Advances in Imaging and Electron Physics*, volume 122, pages 173–249. Elsevier, 2002.

[63] G Pozzi. Electron holography of long-range electromagnetic fields: A tutorial. In *Advances in Imaging and Electron Physics*, volume 123, pages 207–223. Elsevier, 2002.

[64] H Lichte, F Börrnert, A Lenk, A Lubk, F Röder, J Sickmann, S Sturm, K Vogel, and D Wolf. Electron holography for fields in solids: Problems and progress. *Ultramicroscopy*, 134:126–134, 2013.

[65] G Pozzi, M Beleggia, T Kasama, and RE Dunin-Borkowski. Interferometric methods for mapping static electric and magnetic fields. *Comptes Rendus Physique*, 15(2-3):126–139, 2014.

[66] H Okada, D Shindo, JJ Kim, Y Murakami, and H Kawase. Triboelectricity evaluation of single toner particle by electron holography. *Journal of Applied Physics*, 102(5):054908, 2007.

[67] Y Yao, C Li, ZL Huo, M Liu, CX Zhu, CZ Gu, XF Duan, YG Wang, L Gu, and RC Yu. In situ electron holography study of charge distribution in high-κ charge-trapping memory. *Nature Communications*, 4:2764, 2013.

[68] D Cherns and CG Jiao. Electron holography studies of the charge on dislocations in GaN. *Physical Review Letters*, 87(20):205504, 2001.

[69] S Suzuki, Z Akase, D Shindo, and H Kondo. Suppression of charging effect on collagen fibrils utilizing a conductive probe in TEM. *Microscopy*, 62(4):451–455, 2013.

[70] AC Twitchett, RE Dunin-Borkowski, and PA Midgley. Quantitative electron holography of biased semiconductor devices. *Physical Review Letters*, 88(23):238302, 2002.

[71] G Matteucci, GF Missiroli, M Muccini, and G Pozzi. Electron holography in the study of the electrostatic fields: the case of charged microtips. *Ultramicroscopy*, 45(1):77–83, 1992.

[72] M Beleggia, T Kasama, DJ Larson, TF Kelly, RE Dunin-Borkowski, and G Pozzi. Towards quantitative off-axis electron holographic mapping of the electric field around the tip of a sharp biased metallic needle. *Journal of Applied Physics*, 116(2):024305, 2014.

[73] V Migunov, A London, M Farle, and RE Dunin-Borkowski. Model-independent measurement of the charge density distribution along an Fe atom probe needle using off-axis electron holography without mean inner potential effects. *Journal of Applied Physics*, 117(13):134301, 2015.

[74] M Beleggia, T Kasama, RE Dunin-Borkowski, S Hofmann, and G Pozzi. Direct measurement of the charge distribution along a biased carbon nanotube bundle using electron holography. *Applied Physics Letters*, 98(24):243101, 2011.

[75] CT Koch. A flux-preserving non-linear inline holography reconstruction algorithm for partially coherent electrons. *Ultramicroscopy*, 108(2):141–150, 2008.

[76] M Beleggia, MA Schofield, VV Volkov, and Y Zhu. On the transport of intensity technique for phase retrieval. *Ultramicroscopy*, 102(1):37–49, 2004.

[77] CT Koch and A Lubk. Off-axis and in-line electron holography: A quantitative comparison. *Ultramicroscopy*, 110(5):460–471, 2010.

[78] N Shibata, SD Findlay, Y Kohno, H Sawada, Y Kondo, and Y Ikuhara. Differential phase-contrast microscopy at atomic resolution. *Nature Physics*, 8(8):611, 2012.

[79] A Hangleiter, F Hitzel, S Lahmann, and U Rossow. Composition dependence of polarization fields in GaInN/GaN quantum wells. *Applied Physics Letters*, 83(6):1169–1171, 2003.

[80] K Müller-Caspary, T Grieb, J Müßener, N Gauquelin, P Hille, J Schörmann, J Verbeeck, S Van Aert, M Eickhoff, and A Rosenauer. Electrical polarization in AlN/GaN nanodisks measured by momentum-resolved 4D scanning transmission electron microscopy. *Physical Review Letters*, 122(10):106102, 2019.

[81] M Lohr, R Schregle, M Jetter, C Wächter, T Wunderer, F Scholz, and J Zweck. Differential phase contrast 2.0—opening new "fields" for an established technique. *Ultramicroscopy*, 117:7–14, 2012.

[82] K Müller, FF Krause, A Béché, M Schowalter, V Galioit, S Löffler, J Verbeeck, J Zweck, P Schattschneider, and A Rosenauer. Atomic electric fields revealed by a quantum mechanical approach to electron picodiffraction. *Nature Communications*, 5:5653, 2014.

[83] N Shibata, SD Findlay, T Matsumoto, Y Kohno, T Seki, G Sänchez-Santolino, and Y Ikuhara. Direct visualization of local electromagnetic field structures by scanning transmission electron microscopy. *Accounts of Chemical Research*, 50(7):1502–1512, 2017.

[84] K Müller-Caspary, FF Krause, T Grieb, S Löffler, M Schowalter, V Béché, Aand Galioit, D Marquardt, J Zweck, P Schattschneider, J Verbeeck, and A Rosenauer. Measurement of atomic electric fields and charge densities from average momentum transfers using scanning transmission electron microscopy. *Ultramicroscopy*, 178:62–80, 2017.

[85] TL Kirk. A review of scanning electron microscopy in near field emission mode. In *Advances in Imaging and Electron Physics*, volume 204, pages 39–109. Elsevier, 2017.

[86] A Kyritsakis, JP Xanthakis, TL Kirk, and D Pescia. Lateral reution of the NFESEM microscopy and the existence of self focusing of electrons. In *Vacuum Nanoelectronics Conference (IVNC), 2011 24th International*, pages 21–22. IEEE, 2011.

[87] E Mikmeková, H Bouyanfif, M Lejeune, I Müllerová, M Hovorka, M Unčovskỳ, and L Frank. Very low energy electron microscopy of graphene flakes. *Journal of Microscopy*, 251(2):123–127, 2013.

[88] D Gabor. A new microscopic principle. *Nature*, 161:777–778, 1948.

[89] H Lichte and M Lehmann. Electron holography—basics and applications. *Reports on Progress in Physics*, 71(1):016102, 2007.

[90] E Völkl, LF Allard, and DC Joy, editors. *Introduction to Electron Holography*. Springer Science & Business Media, 1999.

[91] GF Missiroli, G Pozzi, and U Valdre. Electron interferometry and interference electron microscopy. *Journal of Physics E: Scientific Instruments*, 14(6):649–671, 1981.

[92] M Beleggia and G Pozzi. Phase shift of charged metallic nanoparticles. *Ultramicroscopy*, 110(5):418–424, 2010.

[93] EG Pogorelov, AI Zhbanov, and Y Chang. Field enhancement factor and field emission from a hemi-ellipsoidal metallic needle. *Ultramicroscopy*, 109(4):373–378, 2009.

[94] K Svensson, Y Jompol, H Olin, and E Olsson. Compact design of a transmission electron microscope-scanning tunneling microscope holder with three-dimensional coarse motion. *Review of Scientific Instruments*, 74(11):4945–4947, 2003.

[95] G Singh, R Bücker, G Kassier, M Barthelmess, F Zheng, V Migunov, M Kruth, RE Dunin-Borkowski, ST Purcell, and RJ D Miller. Fabrication and characterization of a focused ion beam milled lanthanum hexaboride based cold field electron emitter source. *Applied Physics Letters*, 113(9):093101, 2018.

[96] M Remškar, J Kovac, M Viršek, M Mrak, A Jesih, and A Seabaugh. W_5O_{14} nanowires. *Advanced Functional Materials*, 17(12):1974–1978, 2007.

[97] R Liu, Z-A Li, C Zhang, X Wang, MA Kamran, M Farle, and B Zou. Single-step synthesis of monolithic comb-like CdS nanostructures with tunable waveguide properties. *Nano Letters*, 13(6):2997–3001, 2013.

[98] P Morgan. *Carbon fibers and their composites*. CRC press, 2005.

[99] P Eklund, M Beckers, U Jansson, H Högberg, and L Hultman. The $M_{n+1}AX_n$ phases: Materials science and thin-film processing. *Thin Solid Films*, 518(8):1851–1878, 2010.

[100] W Tian, P Wang, G Zhang, Y Kan, Y Li, and D Yan. Synthesis and thermal and electrical properties of bulk Cr_2AlC. *Scripta Materialia*, 54(5):841–846, 2006.

[101] KG Pradeep, K Chang, A Kovács, S Sen, A Marshal, R de Kloe, RE Dunin-Borkowski, and JM Schneider. Nano-scale Si segregation and precipitation in $Cr_2Al(Si)C$ MAX phase coatings impeding grain growth during oxidation. *Materials Research Letters*, 7(5):180–187, 2019.

[102] F Zheng, J Caron, V Migunov, M Beleggia, G Pozzi, and RE Dunin-Borkowski. Measurement of charge density in nanoscale materials using off-axis electron holography. *Journal of Electron Spectroscopy and Related Phenomena*, 2020, in press.

[103] M O'Keeffe and JCH Spence. On the average Coulomb potential (Φ_0) and constraints on the electron density in crystals. *Acta Crystallographica Section A: Foundations of Crystallography*, 50(1):33–45, 1994.

[104] J Zweck. Imaging of magnetic and electric fields by electron microscopy. *Journal of Physics: Condensed Matter*, 28(40):403001, 2016.

[105] E Völkl and D Tang. Approaching routine $2\pi/1000$ phase resolution for off-axis type holography. *Ultramicroscopy*, 110(5):447–459, 2010.

[106] J Caron. *Model-based reconstruction of magnetisation distributions in nanostructures from electron optical phase images*. PhD thesis, Jülich: Forschungszentrum Jülich, Zentralbibliothek, 2017.

[107] A Tarantola. *Inverse problem theory and methods for model parameter estimation*. Society for Industrial and Applied Mathamatics, 2005.

[108] AN Tikhonov and VIA Arsenin. *Solutions of ill-posed problems, ser. Scripta series in mathematics.* Washington and New York: Winston and Distributed solely by Halsted Press, 1977.

[109] DW Kammler. *A first course in Fourier analysis*. Cambridge University Press, 2007.

[110] JD Jackson. *Classical Electrodynamics*. Wiley, 2012.

[111] PC Hansen. Analysis of discrete ill-posed problems by means of the L-curve. *SIAM Review*, 34(4):561–580, 1992.

[112] F Zheng, G Pozzi, V Migunov, L Pirker, M Remškar, M Beleggia, and RE Dunin-Borkowski. Quantitative measurement of charge accumulation along a quasi-one-dimensional W_5O_{14} nanowire during electron field emission. *Nanoscale*, 12:10559–10564, 2020.

[113] WA de Heer, A Châtelain, and D Ugarte. A carbon nanotube field-emission electron source. *Science*, 270(5239):1179–1180, 1995.

[114] N de Jonge, Y Lamy, K Schoots, and TH Oosterkamp. High brightness electron beam from a multi-walled carbon nanotube. *Nature*, 420(6914):393, 2002.

[115] M Žumer, V Nemanič, B Zajec, M Wang, J Wang, Y Liu, and L-M Peng. The field-emission and current-voltage characteristics of individual W_5O_{14} nanowires. *The Journal of Physical Chemistry C*, 112(14):5250–5253, 2008.

[116] G Ulisse, C Ciceroni, AD Carlo, F Brunetti, J Jelenc, M Saqib, A Varlec, and M Remskar. Synthesis and field emission characteristics of W_5O_{14} nanowires film. *Microelectronic Engineering*, 170:44–48, 2017.

[117] M Saqib, J Jelenc, L Pirker, SD Škapin, L de Pietro, U Ramsperger, A Knápek, I Müllerová, and M Remškar. Field emission properties of single crystalline W_5O_{14} and $W_{18}O_{49}$ nanowires. *Journal of Electron Spectroscopy and Related Phenomena*, 2020, in press.

[118] Y Li, Y Bando, and D Golberg. Quasi-aligned single-crystalline $W_{18}O_{49}$ nanotubes and nanowires. *Advanced Materials*, 15(15):1294–1296, 2003.

[119] N de Jonge. Carbon nanotube electron sources for electron microscopes. In *Advances in imaging and electron physics*, volume 156, pages 203–233. Elsevier, 2009.

[120] G Matteucci, GF Missiroli, JW Chen, and G Pozzi. Mapping of microelectric and magnetic fields with double-exposure electron holography. *Applied Physics Letters*, 52(3):176–178, 1988.

[121] V Migunov, C Dwyer, CB Boothroyd, G Pozzi, and RE Dunin-Borkowski. Prospects for quantitative and time-resolved double and continuous exposure off-axis electron holography. *Ultramicroscopy*, 178:48–61, 2017.

[122] CA Spindt, I Brodie, L Humphrey, and ER Westerberg. Physical properties of thin-film field emission cathodes with molybdenum cones. *Journal of Applied Physics*, 47(12):5248–5263, 1976.

[123] J Bonard, M Croci, I Arfaoui, O Noury, D Sarangi, and A Châtelain. Can we reliably estimate the emission field and field enhancement factor of carbon nanotube film field emitters? *Diamond and Related Materials*, 11(3-6):763–768, 2002.

[124] AH Tavabi, V Migunov, C Dwyer, RE Dunin-Borkowski, and G Pozzi. Tunable caustic phenomena in electron wavefields. *Ultramicroscopy*, 157:57–64, 10 2015.

[125] DJ Griffiths and Y Li. Charge density on a conducting needle. *American Journal of Physics*, 64(6):706–714, 1996.

[126] M Andrews. Equilibrium charge density on a conducting needle. *American Journal of Physics*, 65(9):846–850, 1997.

[127] JD Jackson. Charge density on thin straight wire, revisited. *American Journal of Physics*, 68(9):789–799, 2000.

[128] JB Ross. Plotting the charge distribution of a closed-loop conducting wire using a microcomputer. *American Journal of Physics*, 55(10):948–950, 1987.

[129] WR Smythe. Charged right circular cylinder. *Journal of Applied Physics*, 27(8):917–920, 1956.

[130] Emile Durand. *Électrostatique*, volume 2. Masson: Paris, 1964.

[131] Debabrata Biswas. A universal formula for the field enhancement factor. *Physics of Plasmas*, 25(4):043113, 2018.

[132] C Phatak, L de Knoop, F Houdellier, C Gatel, MJ Hÿtch, and A Masseboeuf. Quantitative 3D electromagnetic field determination of 1D nanostructures from single projection. *Ultramicroscopy*, 164:24–30, 2016.

[133] M Wu, A Tafel, P Hommelhoff, and E Spiecker. Determination of 3D electrostatic field at an electron nano-emitter. *Applied Physics Letters*, 114(1):013101, 2019.

[134] W van Aarle, WJ Palenstijn, J de Beenhouwer, T Altantzis, S Bals, KJ Batenburg, and J Sijbers. The ASTRA toolbox: A platform for advanced algorithm development in electron tomography. *Ultramicroscopy*, 157:35–47, 2015.

[135] Z Saghi, G Divitini, B Winter, R Leary, E Spiecker, C Ducati, and PA Midgley. Compressed sensing electron tomography of needle-shaped biological specimens–potential for improved reconstruction fidelity with reduced dose. *Ultramicroscopy*, 160:230–238, 2016.

[136] T Sakurai and EW Müller. Field calibration using the energy distribution of field ionization. *Physical Review Letters*, 30(12):532, 1973.

[137] T Sakurai and EW Müller. Field calibration using the energy distribution of a free-space field ionization. *Journal of Applied Physics*, 48(6):2618–2625, 1977.

[138] KK Singh, KK Senapati, C Borgohain, and KC Sarma. Newly developed Fe_3O_4–Cr_2O_3 magnetic nanocomposite for photocatalytic decomposition of 4-chlorophenol in water. *Journal of Environmental Sciences*, 52:333–340, 2017.

[139] MS Chung and TE Everhart. Simple calculation of energy distribution of low-energy secondary electrons emitted from metals under electron bombardment. *Journal of Applied Physics*, 45(2):707–709, 1974.

[140] TF Kelly. Atomic-scale analytical tomography. *Microscopy and Microanalysis*, 23(1):34–45, 2017.

[141] V Astašauskas, A Bellissimo, P Kuksa, C Tomastik, H Kalbe, and WSM Werner. Optical and electronic properties of amorphous silicon dioxide by single and double electron spectroscopy. *Journal of Electron Spectroscopy and Related Phenomena*, 2020, in press.

[142] A Bellissimo, GM Pierantozzi, A Ruocco, G Stefani, OY Ridzel, V Astašauskas, WSM Werner, and M Taborelli. Secondary electron generation mechanisms in carbon allotropes at low impact electron energies. *Journal of Electron Spectroscopy and Related Phenomena*, 2020, in press.

[143] Stephen Wolfram. *The mathematica book*. Wolfram Media, Champaign, IL, 4th edition, 1999.

Appendix A

Elementary expressions for phase and electric field

A.1 Preliminary knowledge

A Potential of a point charge $q(x_0,\ y_0,\ z_0)$:

$$V_P = \frac{q}{4\pi\varepsilon_0}\frac{1}{\sqrt{(x-x_0)^2+(y-y_0)^2+(z-z_0)^2}}, \tag{A.1}$$

where $(x,\ y,\ z)$ is an arbitrary point P in space except $(x_0,\ y_0,\ z_0)$, $\varepsilon_0 = 8.85\times10^{-12}$ F/m is the vacuum permittivity.

B Indefinite Integral:

$$\int \frac{1}{\sqrt{a^2+x^2}}\,dx = \ln\left(x+\sqrt{a^2+x^2}\right)+C. \tag{A.2}$$

C Image charge:

Assume that a point charge is located at $(x_0,\ y_0)$ and the normal vector of a planar counter-electrode is $(a,\ b)$. The position of the image charge $(x_0',\ y_0')$ is then:

$$x_0' = \frac{b^2-a^2}{a^2+b^2}x_0 - \frac{2ab}{a^2+b^2}y_0 + 2a \tag{A.3}$$

$$y_0' = \frac{a^2-b^2}{a^2+b^2}y_0 - \frac{2ab}{a^2+b^2}x_0 + 2b \tag{A.4}$$

A.2 Phase of a point charge

The electrostatic potential of a point charge $q(x_0,\, y_0,\, 0)$ and its image charge $-q(x_0',\, y_0',\, 0)$, *i.e.*, a dipole, can be written as follows:

$$V_P = \frac{q}{4\pi\varepsilon_0}\frac{1}{\sqrt{(x-x_0)^2+(y-y_0)^2+z^2}} - \frac{q}{4\pi\varepsilon_0}\frac{1}{\sqrt{(x-x_0')^2+(y-y_0')^2+z^2}}. \tag{A.5}$$

The total phase can be calculated by integrating the electrostatic potential in the electron beam direction z, from $-\infty$ to $+\infty$, in the form

$$\varphi(x,y) = C_E \int_{-\infty}^{+\infty} V_P\, dz = C_E \frac{q}{4\pi\varepsilon_0} \ln \frac{(x-x_0')^2+(y-y_0')^2}{(x-x_0)^2+(y-y_0)^2}, \tag{A.6}$$

where C_E is an interaction parameter and takes a value of 6.53×10^6 rad/(V·m) at 300 kV.

One should be aware that two singularities at the dipole positions are present in the above expressions. Accordingly, here a uniformly-charged sphere model is used to avoid such singularities, *i.e.*, each singularity (single voxel) is treated as a uniformly-charged sphere.

A.3 Uniformly-charged sphere

In this model, a total charge q in a sphere is assumed to be uniformly distributed.

The volumetric charge density ρ is

$$\rho = \frac{3q}{4\pi R^3}, \tag{A.7}$$

where R is the radius of the sphere.

Electric field

According to Gauss's Law, the electric flux leaving a volume is proportional to the charge inside it, according to the expression

$$\oint_C \vec{E}\cdot d\vec{S} = \frac{Q}{\varepsilon_0}, \tag{A.8}$$

where $\vec{E}$ is the electric field, C is the surface to the volume, $\vec{S}$ is the normal of the surface and Q is the charge enclosed by S.

As a result of spherical symmetry, the electric field can be obtained within and outside the sphere as follows:

- $r < R$, inside the sphere

$$E(r) \cdot 4\pi r^2 = \frac{\rho \cdot \frac{4}{3}\pi r^3}{\varepsilon_0}$$

$$E(r) = \frac{\rho r}{3\varepsilon_0} = \frac{qr}{4\pi\varepsilon_0 R^3} \tag{A.9}$$

- $r \geq R$, outside the sphere

$$E(r) \cdot 4\pi r^2 = \frac{q}{\varepsilon_0}$$

$$E(r) = \frac{q}{4\pi\varepsilon_0 r^2} \tag{A.10}$$

The electric field takes the graphical form shown in Fig. A.1.

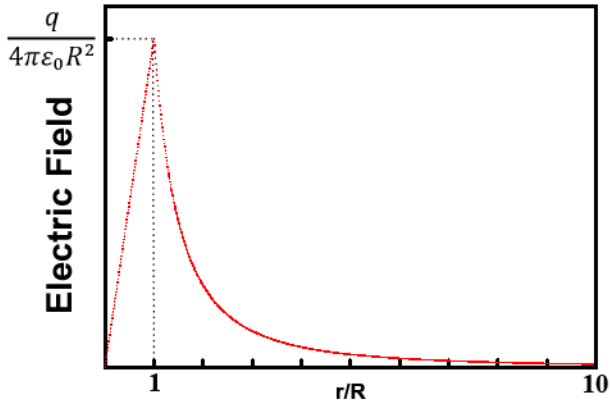

Fig. A.1 Electric field within and outside a uniformly charged sphere. See text for details.

Electrostatic potential

The electrostatic potential outside a uniformly charged sphere can be determined from Eq. A.5. If the potential at infinity is defined to be zero, then

$$V(r) = \frac{q}{4\pi\varepsilon_0 r}. \tag{A.11}$$

The potential at the surface of the sphere is $V|_{r=R} = \frac{q}{4\pi\varepsilon_0 R}$.

The potential difference between any point inside the sphere ($r < R$) and the potential at its surface V_{rR} can be retrieved as follows:

$$V_{rR} = V_r - V_R = \int_r^R \vec{E}\cdot d\vec{l} = \int_r^R E)(r)dr = \frac{q}{8\pi\varepsilon_0 R^3} r^2|_r^R = \frac{q}{8\pi\varepsilon_0 R^3}(R^2 - r^2)$$

$$V_r = V_R + V_{rR} = \frac{q}{8\pi\varepsilon_0 R^3}(3R^2 - r^2). \tag{A.12}$$

The potential takes the graphical form shown in Fig. A.2.

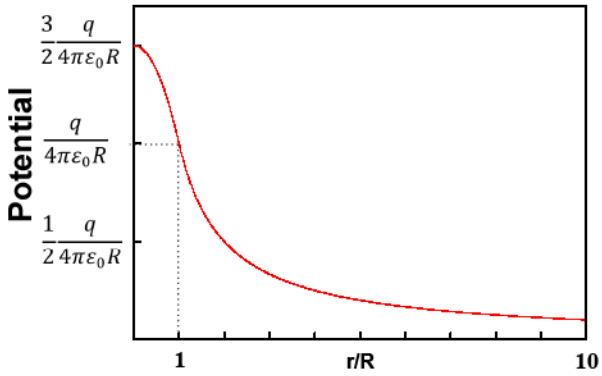

Fig. A.2 Electrostatic potential within and outside a uniformly charged charged sphere. See text for details.

Phase

Just as for a point charge, the phase outside a uniformly charge sphere is given by Eq. A.6. When the electron beam travels through the sphere, the phase has to be calculated carefully to avoid singularities.

The projected distance is defined as the distance between the centre of the sphere and an arbitrary point in the $z = 0$ plane, $(x, y, 0)$. Then, the projected distances of the centres of the sphere and its images, d_1 and d_2, can be given as follows:

$$d_1 = \sqrt{(x-x_0)^2 + (y-y_0)^2},$$
$$d_2 = \sqrt{(x-x_0')^2 + (y-y_0')^2}.$$

If the projected distance d_1 or d_2 is smaller than the radius of the sphere R, *i.e.*, inside the spheres of the charge and its image charge, then the projection has to involve the potential both within and outside the sphere. Due to symmetry, only $d_1 \leq R$ is considered here.

The heights that an electron enters the sphere are listed below:

$$z_1 = \sqrt{R^2 - d_1^2},$$
$$z_2 = \sqrt{R^2 - d_2^2}.$$

The phase shift can then be integrated in two separate regions, *i.e.*, outside and within the sphere, as follows:

$$\begin{aligned}
&\varphi(x,y) \\
&= C_E[\int_{z_1}^{+\infty} V(r>R)\,dz + \int_{-z_1}^{z_1} V(r<R)\,dz + \int_{-\infty}^{-z_1} V(r>R)\,dz + \int_{-\infty}^{+\infty} V^{'}(r>R)\,dz] \\
&= C_E[2\int_{z_1}^{+\infty} V(r>R)\,dz + 2\int_{0}^{+\infty} V^{'}(r>R)\,dz + 2\int_{0}^{z_1} V(r<R)\,dz] \\
&= 2C_E\frac{q}{4\pi\varepsilon_0}(\int_{z_1}^{+\infty} \frac{dz}{\sqrt{(x-x_0)^2+(y-y_0)^2+z^2}} - \int_{0}^{+\infty} \frac{dz}{\sqrt{(x-x_0')^2+(y-y_0')^2+z^2}}) \\
&+ 2C_E\frac{q}{8\pi\varepsilon_0 R^3}\int_0^{z_1} 3R^2 - (d_1^2+z^2)\,dz \\
&= 2C_E\frac{q}{4\pi\varepsilon_0}(\ln(z+\sqrt{z^2+d_1^2})|_{z_1}^{+\infty} - \ln(z+\sqrt{z^2+d_2^2})|_0^{+\infty}) + 2C_E\frac{q}{8\pi\varepsilon_0 R^3}(3R^2-d_1^2)z_1 + \frac{z_1^3}{3}) \\
&= 2C_E\frac{q}{4\pi\varepsilon_0}\ln\frac{d_2}{z_1+\sqrt{z_1^2+d_1^2}} + 2C_E\frac{q}{8\pi\varepsilon_0 R^3}(2R^2 z_1 + \frac{2}{3}z_1^3) \\
&= 2C_E\frac{q}{4\pi\varepsilon_0}(\ln\frac{d_2}{z_1+R} + \frac{z_1}{R} + \frac{z_1^3}{3R^3}).
\end{aligned} \tag{A.13}$$

Similarly, the phase shift inside the image charge sphere is given by the expression:

$$\varphi(x,y) = 2C_E\frac{q}{4\pi\varepsilon_0}(\ln\frac{z_2+R}{d_1} - \frac{z_2}{R} - \frac{z_2^3}{3R^3}). \tag{A.14}$$

In summary, the phase can be expressed as follows:

$$\varphi(x,y) = 2C_E \frac{q}{4\pi\varepsilon_0} \begin{cases} \ln \frac{d_2}{d_1} & \text{if } d_1, d_2 \geq R \\ \ln \frac{d_2}{z_1+R} + \frac{z_1}{R} + \frac{z_1^3}{3R^3} & \text{if } d_1 < R \\ \ln \frac{z_2+R}{d_1} - \frac{z_2}{R} - \frac{z_2^3}{3R^3} & \text{if } d_2 < R \end{cases} . \tag{A.15}$$

Appendix B

Analytical line charge models for a needle-shaped geometry

B.1 Constant line charge model

The electrostatic field outside a charged tip can be obtained using expressions for two constant line charges, whose lengths are $2c$ and whose centres are $2h$ apart, with the lines situated along the y axis in a symmetric position with respect to the xz plane of the xyz coordinate system [71]. The electrostatic potential and phase can then be written as follows:

$$V(x,y,z) = \frac{\lambda}{4\pi\varepsilon_0}\Big[\sinh^{-1}\frac{c-(y-h)}{\sqrt{x^2+z^2}} - \sinh^{-1}\frac{-c-(y-h)}{\sqrt{x^2+z^2}} + \sinh^{-1}\frac{-c-(y+h)}{\sqrt{x^2+z^2}} - \sinh^{-1}\frac{c-(y+h)}{\sqrt{x^2+z^2}}\Big], \tag{B.1}$$

$$\varphi(x,y) = 2C_E \frac{\lambda}{4\pi\varepsilon_0}\Big[\\ (-c+(y-h))\ln\sqrt{x^2+(c-(y-h))^2} + |x|\arcsin\frac{-c+(y-h)}{\sqrt{x^2+(c-(y-h))^2}} \\ +(-c-(y-h))\ln\sqrt{x^2+(c+(y-h))^2} - |x|\arcsin\frac{c+(y-h)}{\sqrt{x^2+(c+(y-h))^2}} \\ +(c+(y+h))\ln\sqrt{x^2+(c+(y+h))^2} + |x|\arcsin\frac{c+(y+h)}{\sqrt{x^2+(c+(y+h))^2}} \\ +(c-(y+h))\ln\sqrt{x^2+(c-(y+h))^2} - |x|\arcsin\frac{-c+(y+h)}{\sqrt{x^2+(c-(y+h))^2}}\Big], \tag{B.2}$$

where λ is the line charge density.

B.2 Linear line charge model

In the presence of an external electric field, an expression for the charge density that increases linearly along the length of a line charge can be used [93, 72]. The electrostatic potential and phase can then be formulated as follows:

$$V(r,y) = \frac{Ky}{4\pi\varepsilon_0}\Big[\frac{4L}{\sqrt{r^2+(y-L)^2}+\sqrt{r^2+(y+L)^2}} + \ln\frac{\sqrt{r^2+(y-L)^2}+(y-L)}{\sqrt{r^2+(y+L)^2}+(y+L)}\Big], \tag{B.3}$$

where K is a constant with units of surface charge density and $r = \sqrt{x^2+z^2}$.

$$\varphi(x,y) = \frac{KC_E}{4\pi\varepsilon_0}\Big[\\ 4Ly + 4xy\arctan\frac{y-L}{x} - 4xy\arctan\frac{y+L}{x} \\ -(L^2+x^2-y^2)\ln\frac{x^2+(y-L)^2}{x^2+(y+L)^2}\Big], \tag{B.4}$$

where L is the length of the line charge, *i.e.*, half of the distance between the foci of the ellipsoid (assuming an ellipsoid-like geometry for the needle), and x and y are Cartesian coordinates. The electric field strength E induced by the counter-electrode and the base on

which the field emitter is located can be calculated using the expression

$$E = \frac{K}{4\pi\varepsilon_0}(\ln\frac{1+e}{1-e} - 2e), \tag{B.5}$$

where e is the eccentricity of the needle, $e = \frac{L}{a}$ and a is the major semi-axis.

Appendix C

Analytical model-dependent approach for the W_5O_{14} nanowire

This appendix contains further details about the numerical and analytical modelling and simulations for the experimental setup presented in Chapter 6.

C.1 Analytical and numerical modelling

As explained in Chapter 6, we attempt to adapt our setup to the considerations developed in a series of didactic papers written with the purpose of answering the question of the equilibrium charge distribution on a conducting needle [125–127]. These works have also highlighted the influence of the shape of the conductor on the charge distribution and confirmed the accumulation of charge at the tips of cylindrical metallic needles.

Analytical solutions are known for the electrostatic potentials and electron optical phase shifts of line charges that have constant [124] and linear [74] charge density distributions. In the present case, our starting point is the expression for the electrostatic potential of a line charge that extends along the y axis from $-a$ to 0, which takes the form [124]

$$V(x,y,z) = \frac{K}{4\pi\varepsilon_0}\left[\log\left(\frac{\sqrt{(a+y)^2+x^2}+a+y}{\sqrt{x^2+y^2}+y}\right) - \frac{a}{\sqrt{(x+x_D)^2+(y+y_D)^2}}\right], \tag{C.1}$$

where K is the charge density and $(x_D, y_D, 0)$ are the coordinates of a neutralising charge.

Table C.1 Lengths and line charge densities of the support, the nanowire and the counter-electrode based on the analytical model.

Electrode	Length (a, μm)	Charge density(λ, e/nm)
Support	50	8.1
Nanowire	9.4	11.5
Counter-electrode	80	-8.14

In order to model the experimental setup, which consists of the fixed side of the specimen holder (the support), the attached nanowire and the counter-electrode, we first consider three aligned line charges and choose their lengths and charge densities so that the shapes of the resulting equipotentials approximately fit the shapes of the real electrodes (*i.e.*, the support, the nanowire and the counter-electrode). In order to remove the need for neutralising charges, we chose the charge density of the counter-electrode to obtain overall neutrality of the setup, while ensuring that the charge on the nanowire was in agreement with the experimentally measured value. By adjusting these parameters, we obtained values for the experimental setup that are given in Table C.1.

In this model, the shape of the nanowire and support is defined by the equipotential surface at $V_s = V_n$ = 130 V, while the shape of the counter-electrode is defined by the equipotential surface at V_c = -20 V.

It should be noted that the nanowire is attached to the support and its distance from the counter-electrode is 1.6 μm. Fig. C.1a shows a schematic diagram of the setup of the analytical model. Fig. C.1b-d show equipotential plots corresponding to this preliminary step on three different scales. The equipotential surface corresponding to V_n = 130 V (*i.e.*, the shape of the nanowire) is extremely sharp (approximately 40 nm in diameter at a distance of 1.2 μm from the apex), as shown in Fig. C.1d.

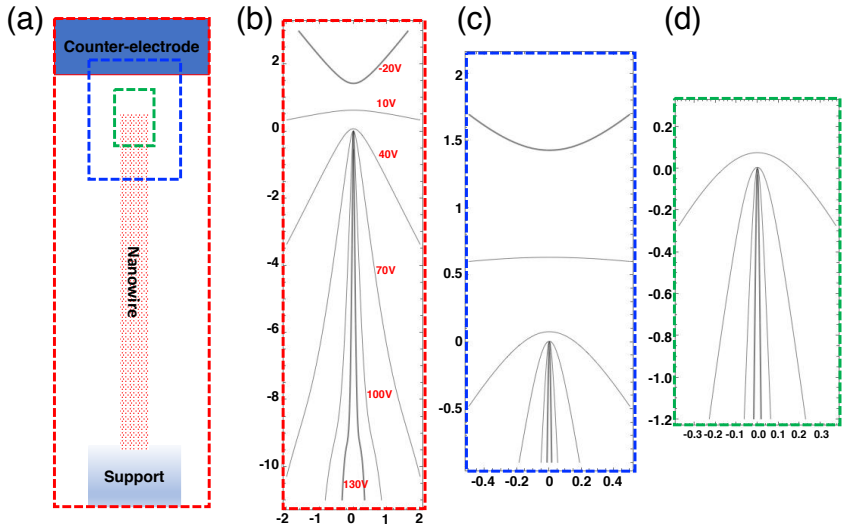

Fig. C.1 (a) Schematic illustration of the analytical model; (b-d) Equipotential plots in the $z = 0$ plane resulting from the presence of the three line charges, shown on different length scales with distances given in μm. (b) The entire setup, including the support, the nanowire and the counter-electrode, are marked in red in (a). (c) The nanowire and counter-electrode, marked in blue in (a). (d) The nanowire, marked in green in (a). The equipotential lines are at -20 V (counter-electrode), 10 V, 40 V, 70 V, 100 V and 130 V (nanowire and support), labelled in (b).

In order to better approximate the cylindrical shape of the nanowire, its continuous charge distribution was modelled using $N = 601$ equally-spaced charges along its length. In order to include the effects of the support and the counter-electrode, their potentials were added to those of the discrete charges, making use of the requirement that the potential mid-way between the discrete charges and the support should be a constant. This constant was determined by imposing the additional constraint that the total charge must be equal to that of the previous continuous line charge. The result of these calculations is shown in Fig. C.2 in the form of equipotentials plotted in the $z = 0$ plane. The lateral dimension (*i.e.*, diameter) of the discrete charge of the nanowire at a distance of 1.2 μm from the apex) is similar to the experimental value (100 nm) and is larger than that of the continuous one (40 nm). Moreover, the shape of the resulting equipotential surface that describes the nanowire is now nearly cylindrical with a round apex.

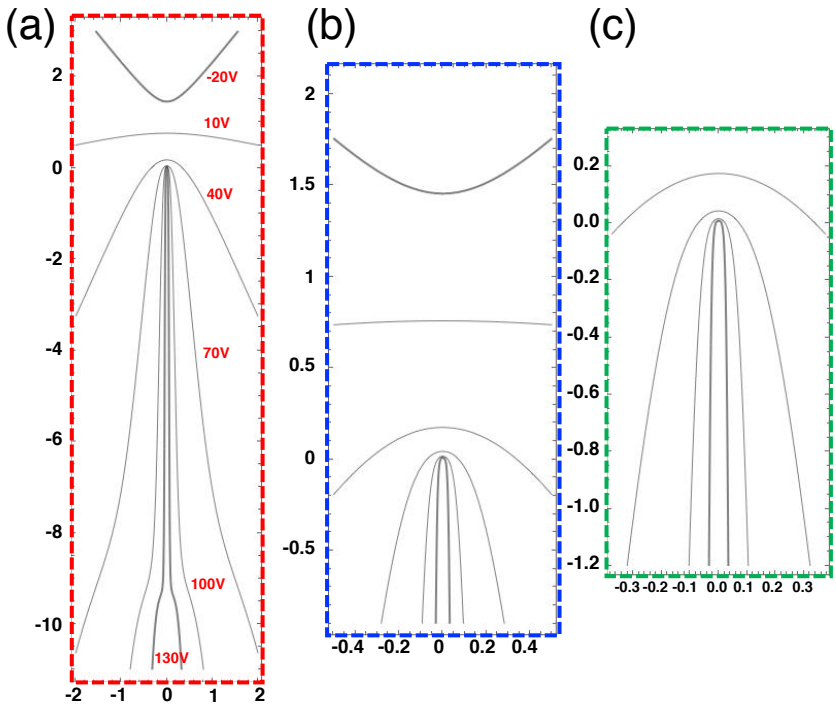

Fig. C.2 Equipotential plots in the $z = 0$ plane for the above two line charges (*i.e.*, representing the counter-electrode and support) and a discrete distribution of $N = 601$ equidistant charges in place of the nanowire, shown on different length scales, as in Fig. C.1.

Interestingly, the resulting discrete charge density in the nanowire oscillates strongly, as shown in Fig. C.3a. This effect is probably due to the choice of the potential mid-way between the discrete charges. If it is averaged over each pair of neighbouring points, then it resembles the expected behaviour, as shown in Fig. C.3b. The cumulative charge integrated along the nanowire is shown in Fig. C.3c and its difference from a 2^{nd} order polynomial fit (with all of the data points used for fitting) is shown in Fig. C.3d.

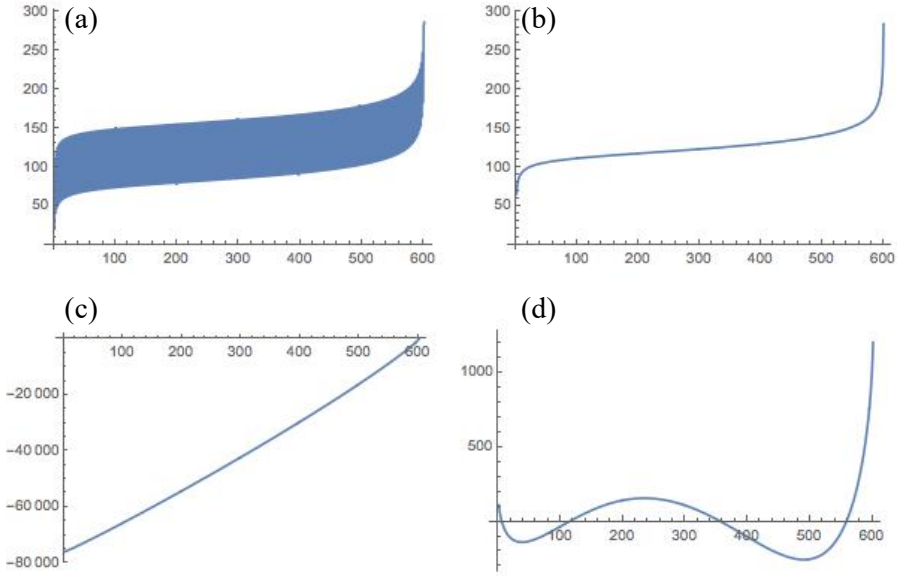

Fig. C.3 Calculated charge density from the analytical model shown in Fig. C.2. (a) Oscillating charge density in the nanowire. (b) Charge density after averaging neighbouring points. (c) Cumulative charge integrated along the nanowire. (d) Difference between the cumulative charge in (c) and a 2^{nd} order polynomial fit. The horizontal axis contains $N = 601$ discrete charges. The vertical axis in (a) and (b) is the charge density (e/nm), while that in (c) and (d) is the cumulative charge (electrons). The horizontal axis shows the number of discrete charges (in total $N = 601$).

A simulation was also performed with the equipotential surface of the nanowire at 150 V. The resulting theoretical cumulative charge profile, together with a 2^{nd} order polynomial fit (with the data points close to the apex not used for fitting) are shown in Fig. C.4 for the last 700 nm. These can be compared with the experimental results shown in Fig. 6.9, demonstrating that the charge accumulated at the apex still differs by a factor of approximately 2 from the experimental value. Although it may be possible to reduce this discrepancy by making use of a three-dimensional discrete model, the use of such an approach is not addressed in this thesis.

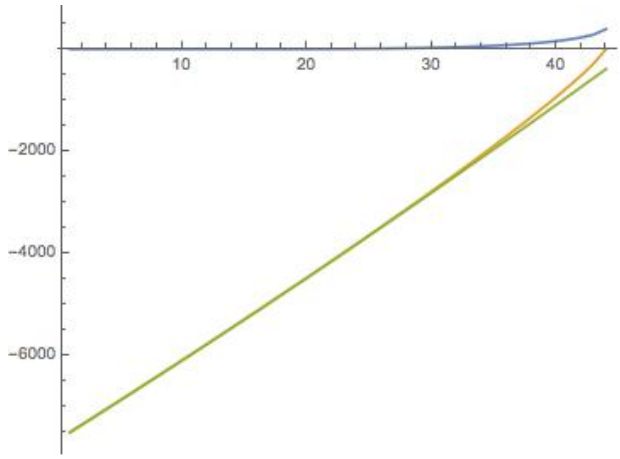

Fig. C.4 Theoretical cumulative charge profile (yellow) when the equipotential surface of the nanowire is at 150 V, its corresponding 2^{nd} order polynomial fit (green) and their difference (blue) for the last 700 nm of the nanowire. The vertical axis shows the cumulative charge (electrons), while the horizontal axis shows the number of discrete charges.

C.2 Fitting of charge density and cumulative charge

A more complete understanding of the function that is fitted to the experimental data can be obtained from the paper by Griffiths and Li [125], who were in turn inspired by the treatment by Smythe [129] of a finite cylinder. They considered the so-called "fundamental term" in Smythe's series expansion of the charge density along a cylinder of length $2A_0$, oriented with its axis parallel to the y axis, which takes the form

$$\lambda(y) = C_0 + \frac{B_0}{(A_0^2 - y^2)^{1/3}}. \tag{C.2}$$

In this way, they obtained an excellent agreement with their discrete charge distribution.

In the present study, it is of interest to determine what happens at the apex of the nanowire, say for $y \leq A_0$. By assuming that A_0 is large, we obtain the following model for the charge distribution

$$\lambda(y) = C_0 + \frac{B}{(A_0 - y)^{1/3}}, \tag{C.3}$$

where $B = \frac{B_0}{(2A_0)^{1/3}}$.

In order to reproduce our data, we also introduce a linear term. Renaming the parameters, we obtain the expression

$$\lambda(y) = C_0 + \frac{B}{(A_0 - y)^{1/3}} + Dy. \tag{C.4}$$

In our experiments, the field of view is limited and only a finite length of the nanowire can be seen. If the length inside the field of view is A, then y in this coordinate system varies from $(A_0 - A)$ to A_0. As the origin of the above coordinate system cannot be determined in the experimental data, we allow y to start from 0 at the left edge of the image and to end at the right edge of the image. In this coordinate system, Eq. C.4 can be reduced to the form

$$\lambda(y) = C + \frac{B}{(A - y)^{1/3}} + Dy, \tag{C.5}$$

where $C = C_0 + D(A_0 - A)$.

By integrating the above expression to find the cumulative charge and imposing the restriction that the cumulative charge must be zero at the tip and beyond, we finally obtain the expression for the cumulative charge

$$-\frac{1}{2}A(2C + AD) + Cy + \frac{1}{2}Dy^2 - \frac{3}{2}B(A - y)^{2/3}. \tag{C.6}$$

This function provides excellent fits to experimental data, as shown in Fig. C.5 and Table C.2.

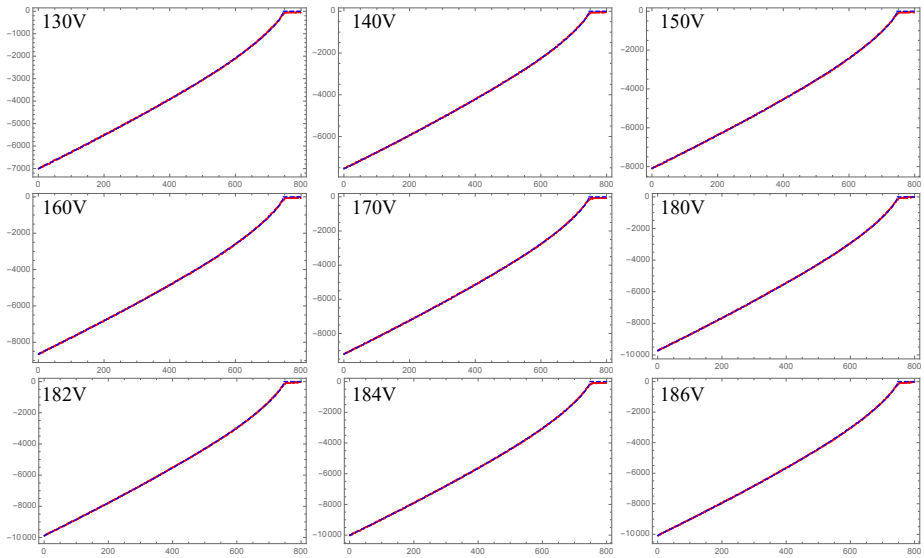

Fig. C.5 Fitting of experimental cumulative charge profiles at different bias voltages based on Eq. C.6. The number in the upper left of each image denotes the applied bias voltage. The experimental data are shown in dashed black lines and the fits are shown in red. The horizontal axis in each image is distance (nm), while the vertical axis in each image is cumulative charge (electrons).

Table C.2 Fitted parameters to experimental cumulative charge profiles for different applied bias voltages based on Eq. C.6.

Voltage(V)	A	B	C	D
130	746.22	42.11	2.60	-4.83×10^{-4}
140	746.76	45.21	2.85	-5.72×10^{-4}
150	746.27	49.02	2.91	-4.75×10^{-4}
160	746.24	53.24	3.04	-6.77×10^{-4}
170	746.12	56.94	3.133	-1.10×10^{-3}
180	746.33	60.51	3.40	-9.95×10^{-4}
182	746.95	60.62	3.58	-1.00×10^{-3}
184	748.24	62.68	3.78	-9.46×10^{-4}
186	747.53	61.26	3.58	-6.29×10^{-4}

Although the goodness of fit provides strong evidence that the accumulation of charge at the apex of the nanowire can be described successfully using Eq. C.6, the parameters

cannot be determined for the whole nanowire, but only for its apex. In order to obtain this information in a more general way and to assess the relative weights of the linear and additional "accumulation" contributions to the field enhancement factor, we now consider the more idealised geometry of a line charge distribution in the presence of a flat anode.

C.3 Rounded cylindrical needle on a conducting plane

As shown by Durand [130] (see also the work of Pogorelov and co-workers [93]), we consider the case of a line charge of length A_0, protruding perpendicularly from a conducting plane along the y direction in the presence of an applied constant field E_0 (*i.e.*, a linear electrostatic potential $-yE_0$) and having a linear charge density distribution vanishing on the plane. If we add the image charges with respect to the plane, at $V = 0$, it turns out that the equipotential surface at $V = 0$ outside the plane corresponds to the shape of a hemi-ellipsoid and is able to represent a metallic hemi-ellipsoidal emitter on a plate in a constant field. Points $(0,\ -A_0)$ and $(0,\ A_0)$ are the foci of the ellipse. At a fixed field, if we take it to be unity for convenience, with fixed length A_0, then the coefficient of the linear density of charge is in one to one relationship with the shape of the ellipse. So, if we choose the radius R at the base of the hemi-ellipsoid at $y = 0$, the charge density is fixed as well as the potential and field in the whole space.

Here, we apply the same procedure to investigate the addition to a linear charge distribution of Smythe's fundamental term (Eq. C.5), noting that this extra parameter introduces a new degree of freedom, which is able to affect the shape of the emitter. With the condition that $\lambda(0) = 0$, the line charge distribution for $y \geq 0$ becomes

$$\lambda(y) = -B + \frac{B}{(1-y)^{1/3}} + Dy. \tag{C.7}$$

A more intuitive physical meaning can be ascribed to the parameters by expressing them as a function of the total charge in the linear term q_{lin} and the total charge in the nonlinear term q_{tip}, resulting in the expression

$$\lambda(y) = -2\frac{q_{tip}}{A} + 2\frac{q_{tip}}{A^{2/3}(A-y)^{1/3}} + 2q_{lin}\frac{y}{A^2}. \tag{C.8}$$

For $y \leq 0$, an image charge distribution should be added to keep the plane $y = 0$ at zero potential. The potential in the entire space then takes the form

$$V(r,y) = \int_0^1 \frac{1}{4\pi\varepsilon_0}\left(\frac{1}{\sqrt{(t-y)^2+r^2}} - \frac{1}{\sqrt{(t+y)^2+r^2}}\right)\lambda(t)dt - y, \tag{C.9}$$

where $r = \sqrt{x^2 + z^2}$ is the radial coordinate, the second term in the brackets corresponds to the image charge and the linear term y corresponds to an added electric field of unit intensity. Software such as Mathematica [143] can be used to provide an analytical solution to this integral equation in terms of hypergeometric confluent functions. However, it is more convenient to evaluate it numerically. By defining $k = \frac{q_{lin}}{q_{tip}}$ and setting the radius at the base (in practice at a small distance from the equipotential plane) to be equal to the aspect ratio of the needle, the last free parameter is used to define the zero equipotential and hence the shape of the emitter. The electric field E can be obtained by taking the gradient of Eq. C.9.

Fig. C.6 shows the ratio-dependence of the shape of the tip of the nanowire for $A_0 = 9.4\ \mu$m and $R = 40$ nm, which are close to the experimental values of our nanowire. Fig. C.6a represents the case for $q_{lin} = 1$ and $q_{tip} = 1$, Fig. C.6b for $q_{lin} = 5$ and $q_{tip} = 1$ and Fig. C.6c for $q_{lin} = 10$ and $q_{tip} = 1$. Owing to the very large aspect ratio we have shown only the region over 1 μm around the tip (distances are in μm). We can see that in the first case (a), with the relatively predominant Smythe's term, the shape of the wire is larger at the tip than at the base. In the second case (b), the shape become more cylindrical, whereas in the case (c), with a predominant linear term, the shape turns into that of an elongated ellipsoid.

Luckily, we do not need more terms in Smythe's expansion [129] for describing our rounded cylindrical nanowire. Having fixed the shape, we can proceed and numerically calculate the electric field in the space around the tip and at the tip itself, where is needed to calculate current density according to the Fowler-Nordheim expression [43].

$$j = \frac{C_1 E^2}{\phi} \exp\left(-\frac{C_2 \phi^{3/2}}{E}\right), \tag{C.10}$$

where ϕ = 4.3 eV [116] is the work function of W_5O_{14} and the first and second Fowler-Nordheim constants are $C_1 = 1.56 \times 10^{-6}$ A eV V^{-2} and $C_2 = 6.83 \times 10^9$ eV$^{-3/2}$ V m^{-1}, respectively. Note that if the work function were to be significantly affected by the surface contamination layer, then a space charge region could form at the wire/contamination layer interface. While we cannot rule out such effects, they are below the sensitivity of the present measurements and require a separate higher spatial resolution study.

By numerically integrating this expression over the surface of the apex, it is possible to calculate the emission current. Fig. 6.14 (see Chapter 6) shows results of calculations for the electric field around the tip, on the axis from the tip and of the emission current for values of k = 4, 5 and 6. It is reassuring that a satisfying agreement with the experimental data is obtained for k = 5.

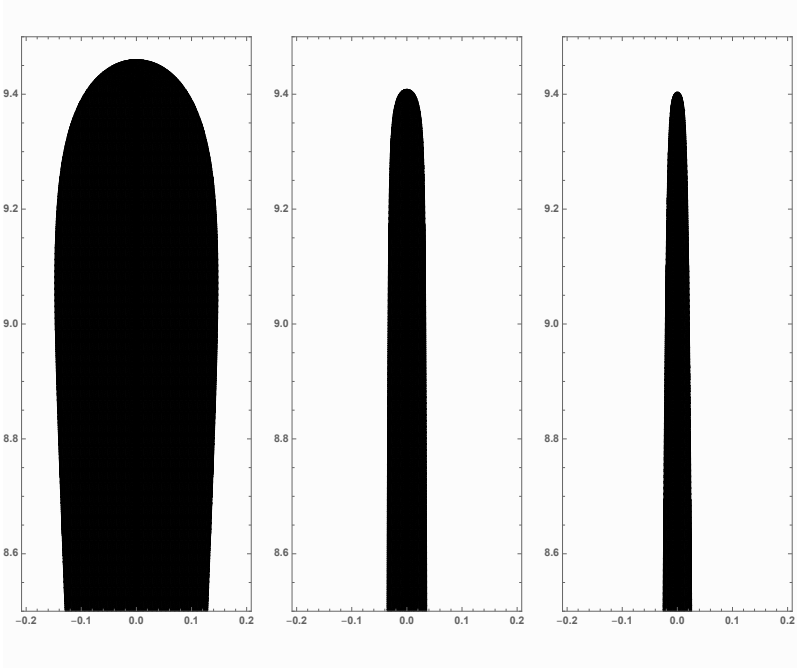

Fig. C.6 Shape of the nanowire near the tip for (a) $q_{lin} = 1$ and $q_{tip} = 1$, (b) $q_{lin} = 5$ and $q_{tip} = 1$ and (c) $q_{lin} = 10$ and $q_{tip} = 1$ in a region over 1 μm around the tip. Distances are shown in units of μm.

Acknowledgements

I would like to take this opportunity to express my sincere gratitude to all of the people who have offered assistance during my Ph. D., both in study and in daily life. In particular, I would like to thank:

- Prof. Dr. Rafal E. Dunin-Borkowski for offering me this chance for a doctoral degree, as well as his valuable suggestions and support.
- Prof. Dr. Joachim Mayer for kindly accepting me for enrolment in Faculty V.
- Dr. Vadim Migunov for his patient and thoughtful supervision on experimental techniques, data analysis, scientific writing and lectures.
- Dr. Jan Caron for his advice and help on Python coding and his Pyramid software framework.
- Prof. Dr. Giulio Pozzi and Dr. Marco Beleggia for their time and effort on theoretical interpretations of experimental data.
- Dr. Hongchu Du and Mr. Patrick Diehle for discussions about tomographic data acquisition and processing.
- Ms. Doris Meertens, Mr. Maximilian Kruth and Ms. Lidia Kibkalo for their assistance with specimen preparation.
- Mr. Rolf Speen, Mr. Werner Pieper and Prof. Michael Farle and AG Farle for technical assistance.
- Ms. Marie Göcking, Ms. Gabriele Mertzbach, Ms. Ingrid Rische-Radloff and Dr. Karsten Tillmann for administrative help.
- Dr. Knut Müller-Caspary, Dr. Florian Winkler, Dr. Helmut Soltner and Dr. Vadim Migunov for their proof-reading and comments on this thesis.
- My wife and son for their encouragement and support throughout my Ph. D. study.

List of Publications

1. Refereed journal publications

   (a) **F Zheng**, G Pozzi, V Migunov, L Pirker, M Remskar, M Beleggia, and RE Dunin-Borkowski. Quantitative measurement of charge accumulation along a quasi-one-dimnesional W_5O_{14} nanowire during electron field emission, *Nanoscale*, 12: 10559–10564, 2020.

   (b) **F Zheng**, V Migunov, J Caron, M Beleggia, G Pozzi, and RE Dunin-Borkowski. Measurement of charge density in nanoscale materials using off-axis electron holography, *Journal of Electron Spectroscopy and Related Phenomena*, 2020, in press.

2. Conferences

   (a) **F Zheng**, V Migunov, J Caron, H Du, G Pozzi, and RE Dunin-Borkowski. Three-dimensional electric field mapping of an electrically biased atom probe needle using off-axis electron holography, *Microscopy and Microanalysis*, 25(S2):326-327, 2019 (Poster).

   (b) **F Zheng**, V Migunov, J Caron, G Pozzi, and RE Dunin-Borkowski, Model-based iterative reconstruction of charge density in nanoscale materials using off-axis electron holography. *Microscopy and Microanalysis*, 25(S2):48-49, 2019.

   (c) E Völkl, **F Zheng**, V Migunov, M Beleggia, and RE Dunin-Brokowski. Live measurement of electrical charge density in materials using off-axis electron holography, *Microscopy and Microanalysis*, 25(S2):44-45, 2019.

   (d) **F Zheng**, V Migunov, J Caron, M Beleggia, G Pozzi, and RE Dunin-Borkowski. Quantitative charge measurement in nanoscale materials using off-axis electron holography, PICO 2019, Vaalsbroek, The Nehterlands, May 6^{th}, 2019 (Poster).

   (e) **F Zheng**, V Migunov, J Caron, G Pozzi, and RE Dunin-Borkowski. Electric field mapping of needle-shaped specimens using off-axis electron holography, Materials Science and Engineering Congress 2018, Darmstadt, Germany, Sept. 26^{th}, 2018 (Oral talk).

   (f) **F Zheng**, V Migunov, U Ramsperger, D Pescia, and RE Dunin-Borkowski. Quantitative measurement of the charge distribution along a tungsten nanotip using transmission electron holography, in: *European Microscopy Congress 2016: Proceedings*, Wiley-VCH Verlag GmbH & Co. KGaA, 2016 (Poster).

Band / Volume 207
NADPH-related studies performed with a SoxR-based biosensor in *Escherichia coli*
A. Spielmann (2019), IV, 73 pp
ISBN: 978-3-95806-438-6

Band / Volume 208
Chemisorption aromatischer Moleküle auf Übergangsmetalloberflächen: Bildung molekularer Hybridmagnete
S. Schleicher (2019), 109 pp
ISBN: 978-3-95806-442-3

Band / Volume 209
Regulatory interactions between *Corynebacterium glutamicum* and its prophages
M. Hünnefeld (2019), IV, 209 pp
ISBN: 978-3-95806-445-4

Band / Volume 210
Quantum Technology
Lecture Notes of the 51st IFF Spring School 2020
23 March – 03 April 2020, Jülich, Germany
ed. by H. Bluhm, T. Calarco, D. DiVincenzo (2020), ca. 700 pp
ISBN: 978-3-95806-449-2

Band / Volume 211
Interaction of physical fields with nanostructured materials
(2020), 255 pp
ISBN: 978-3-95806-450-8

Band / Volume 212
First-principles study of collective spin excitations in noncollinear magnets
F.J. dos Santos (2020), 270 pp
ISBN: 978-3-95806-459-1

Band / Volume 213
Direct measurement of anisotropic resistivity in thin films using a 4-probe STM
T. Flatten (2020), viii, 129 pp
ISBN: 978-3-95806-460-7

Band / Volume 214
The guided self-assembly of magnetic nanoparticles into two- and three-dimensional nanostructures using patterned substrates
W. Ji (2020), VI, 140 pp
ISBN: 978-3-95806-462-1

Band / Volume 215
Molecular layer deposition and protein interface patterning for guided cell growth
M. Glass (2020), iv, 81 pp
ISBN: 978-3-95806-463-8

Band / Volume 216
Development of a surface acoustic wave sensor for in situ detection of molecules
D. Finck (2020), 63 pp
ISBN: 978-3-95806-464-5

Band / Volume 217
Detection and Statistical Evaluation of Spike Patterns in Parallel Electrophysiological Recordings
P. Quaglio (2020), 128 pp
ISBN: 978-3-95806-468-3

Band / Volume 218
Automatic Analysis of Cortical Areas in Whole Brain Histological Sections using Convolutional Neural Networks
H. Spitzer (2020), xii, 162 pp
ISBN: 978-3-95806-469-0

Band / Volume 219
Postnatale Ontogenesestudie (Altersstudie) hinsichtlich der Zyto- und Rezeptorarchitektonik im visuellen Kortex bei der grünen Meerkatze
D. Stibane (2020), 135 pp
ISBN: 978-3-95806-473-7

Band / Volume 220
Inspection Games over Time: Fundamental Models and Approaches
R. Avenhaus und T. Krieger (2020), VIII, 455 pp
ISBN: 978-3-95806-475-1

Band / Volume 221
High spatial resolution and three-dimensional measurement of charge density and electric field in nanoscale materials using off-axis electron holography
F. Zheng (2020), xix, 182 pp
ISBN: 978-3-95806-476-8

Weitere ***Schriften des Verlags im Forschungszentrum Jülich*** unter
http://wwwzb1.fz-juelich.de/verlagextern1/index.asp

Schlüsseltechnologien / Key Technologies
Band / Volume 221
ISBN 978-3-95806-476-8

Mitglied der Helmholtz-Gemeinschaft